sustainability

Article

Design and Innovative Integrated Engineering Approaches Based Investigation of Hybrid Renewable Energized Drone for Long Endurance Applications

Yinyin Wang [1,2], Lokeshkumar Kumar [3], Vijayanandh Raja [3,*], Hussein A. Z. AL-bonsrulah [4,5,*], Naveen Kumar Kulandaiyappan [3], Ashok Amirtharaj Tharmendra [3], Nagaraj Marimuthu [3] and Mohammed Al-Bahrani [6,7]

1 Economics and Management School, Nantong University, Nantong 226019, China
2 Jiangsu Yangtze River Economic Belt Research Institute, Nantong University, Nantong 226002, China
3 Department of Aeronautical Engineering, Kumaraguru College of Technology, Coimbatore 641049, Tamil Nadu, India
4 Al-Amarah University College, Amarah 62001, Iraq
5 Iraqi Ministry of Oil, Midland Refineries Company, Najaf Refinery, Najaf 54001, Iraq
6 School of Engineering, University of Plymouth, Plymouth PL4 8AA, UK
7 Chemical Engineering and Petroleum Industries Department, Al-Mustaqbal University College, Babylon 51001, Iraq
* Correspondence: vijayanandh.raja@gmail.com (V.R.); huseenabd541@gmail.com (H.A.Z.A.-b.)

Citation: Wang, Y.; Kumar, L.; Raja, V.; AL-bonsrulah, H.A.Z.; Kulandaiyappan, N.K.; Amirtharaj Tharmendra, A.; Marimuthu, N.; Al-Bahrani, M. Design and Innovative Integrated Engineering Approaches Based Investigation of Hybrid Renewable Energized Drone for Long Endurance Applications. *Sustainability* **2022**, *14*, 16173. https://doi.org/10.3390/su142316173

Academic Editor: Pablo Rodríguez-Gonzálvez

Received: 22 September 2022
Accepted: 7 November 2022
Published: 3 December 2022

Abstract: At present, surveillance is attracting attention in the field of UAV development. In particular, border surveillance plays a vital role in obtaining the required data around the border and for assisting in military operations. The primary function of this Hybrid UAV (VTOL and Fixed Wing) is to provide prerequisite data, captured during day/night surveillance, to the respective database. One of the primary problems that arise in border patrolling is the use of the UAV under different environmental conditions, thereby reducing its endurance firmly. In addition to the surveillance equipment, energy harvesting techniques are involved in solving the problem of endurance. The piezoelectric energy harvester and solar panels are added to harvest electrical energy in the UAV. Based on this application, the conceptual design of the Hybrid UAV, based on nature, was designed and investigated theoretically, as well as computationally. A series of analysis, which includes Computational Fluid Dynamics, Finite Element Analysis and Analytical approach, was used to determine the energy harvested from the energy harvester. This work confirms the proposed integrated engineering approach for the estimation of renewable energy, via PVEH patches, and the same approach is thus offered to researchers for subsequent applications. Additionally, a hybrid energy idea for newly developed drones was proposed in this work. This concept will be extensively used in the unmanned aircraft system sectors.

Keywords: energy drone; hybrid energy; hybrid UAV; long endurance; solar energy; piezo-vibrational energy

1. Introduction

The use of unmanned aerial vehicles (UAVs), in both civilian and military settings, has been extensively researched and documented. UAVs are used by modern militaries for patrolling, reconnaissance, and other types of surveillance operations, for the purpose of saving lives and reducing the risk to humans. UAVs can have either fixed wings or rotary wings, and they can have one rotor or multirotors. This classification includes both aircrafts with fixed wings and those with multirotors, due to the fact that both types are utilized often and offer an adequate performance for their purpose. The design of the fixed-wing aircraft is superior, from an aerodynamics standpoint, and can remain airborne for extended periods of time. It was important to maximize the amount of payload storage space in the fuselage and, as a result, the body of an insect, known as a Murder Hornet, served as a source of inspiration for its design. A multirotor UAV is capable of accomplishing the goal for which it was designed, which is to finish a steady mission, somewhere other than on a launch pad or runway, and it can keep its agility for an infinite amount of time; however, it cannot fly for extended periods of time.

An essential aspect of border patrol is watching for any indications that hostile behavior may be taking place along the border. The use of scientific technology in border monitoring produced trustworthy data that could be to the advantage of humanity. Whilst the UAV will enhance the performance and efficiency in ground-based National Border Patrolling, its endurance will decrease, as the cost of power is rapidly increasing. A high endurance level is required for the ground-based border patrol of the United States border. A harvester that runs on non-conventional forms of energy is currently being designed as part of an effort to make the project more long-lasting. This particular UAV is able to provide nighttime photographs, as well as thermal imaging of the target. In the event of an unexpected catastrophe, it may also transport necessities, such as food and medicine.

In particular, the military surveillance of borders presents a number of potential dangers. The military is able to prepare for the future by taking control of a territory and monitoring important fields, in order to obtain the information that they require. This allows them to plan ahead. It is difficult to successfully complete both the encounter and the nightly surveillance at the same time. The UAV is fueled by a renewable energy harvester, which improves its function and enables it to complete numerous jobs simultaneously. The eight propellers that power the MH (Murder Hornet) hybrid UAV give it the power to conquer any obstacle. Utilizing piezoelectric patches, which produce energy through vibration, in conjunction with power harvesting solar cells, results in an increase in both the efficiency of the surveillance and the rate at which it is carried out. As a result, this hybrid UAV offers a potential solution to the issues outlined above.

1.1. Literature Review

The main focus of this literature review is to collect the necessary data for the enhancement of the UAV's endurance. In this regard, we studied the relevant literature in order to gain insight into the optimum energy extractor for UAVs, with respect to their working nature. In total, five stages are involved in this literature section: (1) studies about various energy extractors; (2) studies about suitable energy extractors for UAVs; (3) studies about imposed energy extractors in UAVs; (4) studies about the execution of energies through engineering approaches in UAVs; (5) studies about hybrid energy schemes for energized drone: Initially, Solar, thermal, mechanical, acoustic, wave, and other energy harvesters were summarized in this research [1]. In comparison to other solar cells, multi-junction solar cells were efficient but expensive to maintain. Polymer-based plastic photovoltaic (PV) cells functioned similarly, but at a lower cost. Solar thermoelectric generators can replace solar photovoltaics in home and commercial applications. Synthesized piezoelectric material (PZT) and zinc oxide nano-wire were transformed nanoscale mechanical energy/movements, such as those found in blood vessels, auditory or ultrasonic waves, into electrical energy. Finally, the PV cells and PVEH-based energy extractors were highlighted [1].

The key features, major problems, and projected advances of energy harvesting systems are summarized in this paper. The Pb (Zr, Ti) O_3 (PZT) and other perovskite-type composite oxides were widely used in piezoelectric applications to efficiently convert vibrational energy to electrical energy. Rectennas are antennas with rectifier circuits that convert radio waves into DC electricity for radio wave-generating devices. Carbon nanotube thin films, p-type silicon germanium, cobalt oxide, and others are employed in thermoelectric harvesting [2]. In the lab, researchers altered these "smart materials" using stress, temperature, and magnetic or electric fields. Due to their ability to sense and react, transducers use piezoelectric materials. Piezoelectric materials' distinctive electromechanical properties have made them popular during the past 30 years. Piezoelectric materials were used in many engineering fields, but piezoelectric-based structural health monitoring has changed the market for numerous technological parts [3]. Piezoelectric transducers in small electrical gadgets captured energy. Cantilever beam transducers with multiple design possibilities were used in many applications. Unimorph and bimorph types, diaphragm types, Gimbal types, and stack types were primarily imposed. The PZT 5H was found to be more effective than PZT 4 and PZT 8H [4]. This research examined how to use piezoelectric material to harvest energy from human and mechanical movements. Footfalls can generate 5 watts of electricity by using a Polyvinylidene fluoride device. This was conducted with a full-wave bridge rectifier, wherein it used a lead acid battery [5].

This study examined the construction and performance of a solar-powered UAV with a 4-m wingspan. The SD5060 airfoil was chosen for solar panel installation due to its flat top surface. The system was powered by a Sun Power C60 solar array. The investigations found that the average power consumption during takeoff was 127.32 watts, then 43.26 watts for the rest of the flight. The array's maximum output was 180 watts; however, the average power was 146.69 watts. The results showed that solar electricity can provide more than enough power for level flying [6]. This study showed that a tactical solar power UAV that can fly longer without recharging was needed. As a result of its greater lift coefficient range, the SG6043 airfoil was chosen over the S1223 and SD7032. The designers have considered T-tails and straight wing planform to lessen pressure drop from the leading edge to the trailing edge. The authors were encoded all design parameters in MATLAB and Scilab. Wing properties and aerodynamic performance were analyzed in XFLR5 [7]. This study proposed calculation parameters, development of an e-aircraft, and renewable energy sources-based research. This e-UAV was powered purely by sunlight, it can fly. Border police processes have made mistakes because humans were flawed. Human monitoring was limited, hence this work focused on military surveillance. A fixed-wing UAV was used for espionage in this work. UAVs for border surveillance required extensive flight times. Thus, the power loss was caused by the built-in solar panel power harvesting equipment. The complete UAV design was created in CATIA. The solar panels on the building's exterior faced the wind. The central power management unit delivered electricity to various subsystems from the onboard solar panel array. After rigorous testing, the solar-powered fixed-wing UAV for surveillance was implemented [8]. Experimental investigation showed that the UAV has 22 PV cells, 11 on each wing. The Sun Power C60 monocrystalline silicon PV cells have a theoretical efficiency of 29%. When exposed to 300–1000 W/m^2, a Sun Power C60 solar cell generated 0.5 V. The energy storage system was run on the 3S Li-Po battery. The solar power system barely extended the UAV's flight time at 300 W/m^2, but it worked well above 500 W/m^2. Under the magnitude of 800 W/m^2 sun illuminations, final tests averaged 6.27 W [9].

This article described UAVs' reverse-frequency (RF) energy transmission method. Reusing energy from RF power harvesting was deemed possible; and the RF output released electromagnetic radiation into space. The proper software depended on the mission because electromagnetic wave intensity fluctuates with operational range. The UAV receiver's antenna sent signals to a rectifier. In this case, a radio frequency signal was amplified and the DC was converted. Energy was stored centrally and released as needed. Inaccessible areas, such as woodlands and military, adversary monitoring can use RF energy transfer. The RF based energy approach allowed the UAV to fly longer without draining the battery [10].This multi-rotor UAV was being numerically studied. This collection employed a quadcopter harvester. The model weighs 1 kg, according to numerical calculations. With a 10-inch propeller and 250-watt motor, the computed thrust was 9.57 N. A Blue Zirconate Titanate crystal released electric energy as it grows or shrinks by less than 0.1%. This investigation used the Quadcopter's frame, which was 450 mm long and 540 mm wide [11]. The 3D antenna radiation patterns were used to capture energy for networking UAVs in this article. In order to increase efficiency, stationary energy transmitters, such as ground-based base stations (BSs), have been discussed for replacement with mobile energy transmitters. UAV-assisted energy harvesting has become popular due to the flexibility and ease of setting up UAV base stations. A specified analytical framework was analyzed UAV energy harvesting networks with collocated user equipment (UEs). The UAVs were assumed to be at a constant height above the user cluster centers, and the UE placements were modeled as a Poisson Cluster Process. The authors' UAV setup discussion focused on the end-user. The network performance was examined using two LOS probability function models. Doughnut-shaped radiation antennas were used on UAVs and UEs to investigate how realistic 3D antenna radiation patterns affected network performance. Energy coverage varied numerically with cluster size and UAV height. Energy coverage probability can vary greatly based on antenna angle and UAV density [12]. The solar and RF energy harvesting in UAVs was investigated in this work. The power base battery was a 7660 mAh with 6S-Li-Po. The planets and sun created 18.04 V on average. After 25 s, the 5.02 V RF power output was stable. A 6S Li-Po battery rated at 22.8 V could be topped off with the hybrid solar RF harvesting energy's 23.2 V output and 30-s settling time. Battery charging time depended on charging current. The hybrid approach delivered 6.62A, compared to 1.05A for the other methods. Thus, a hybrid's 1.16-h charging time was more convenient than other ways (7.06 h). Charge time and output powers were better with this hybrid solar-RF energy harvesting system [13].

This study investigated piezoelectric vibration energy harvester (PVEH)-equipped propellers' power-generating potential. The authors solved the UAV endurance problem, which was especially challenging to address for UAVs carrying heavy payload, using the electrified propeller-based technology. There were10 composite blade configurations used; the propellers were CATIA-designed. ANSYS's finite element method and finite volume approach were employed for vibrational and CFD analysis, respectively. The authors were discussed regarding propeller materials and data. The blades' power was determined analytically [14]. A two-bladed propeller powered by a PVEH was studied using MRF-CFD. This article tested and assessed propellers made of GFRP, aluminium alloy, and CFRP. They used CATIA to draw UAV propeller designs that met all design criteria. The calculations determined each material's inherent frequency and aerodynamic stresses. Each material's vibrational characteristics were estimated as a precaution. UAV propellers loaded with PVEH generated significant force in this investigation [15]. A composite fixed-pitch propeller with a 24-inch diameter and a 12-degree pitch angle made from PZT-5A-type macro fiber composites was computationally and empirically analyzed for turboprop engine vibration. Hammer and shaker testing were employed in the trial. Frequency response function (FRF) analysis was utilized during two-mode testing to assess the relationship between input excitation and output response. For computer simulation, a CMM model scaled the propeller. The propeller's resting frequency and mode shape were determined through FEA. Piezoelectric transducers were set at the first mode's highest modal strain. The ANSYS workbench-15.0 and Piezo-extension R 15.0 were used for FEA on the PZT propeller. FRFs were calculated withANSYS-15 Workbench. These results showed that piezoelectric transducers at the propeller blades' first mode maximum modal strain sites effectively dampen blade vibrations [16]. Multifunctional energy harvesting integrated with thin film batteries was examined in this work. This device's frequency response was determined using the Rayleigh-Ritz model for resistive electrical loads. According to the data, the battery normally draws 80 A of current and consumes 0.29 mW of power. QP16N piezoelectric devices and 3.13 mm carbon fiber composite substrate powered this self-charging wing spar. During the four-hour test, the battery was charged at 80 A at 0.27 mW and 0.281 mAh. At moderate stimulation amplitudes, each device's piezoelectric layers can charge the thin-film battery to 40% capacity in 4 h [17].

An RC glider UAV's piezoelectric and solar energy harvesters were tested in this investigation. This UAV was powered by an 11.1 V, 2100 mAh, Li-Po battery and an electric motor. It had a wingspan of 1.8 m, a length of 1.1 m, and a takeoff weight of 0.9 kg. It employed a cantilever PFC harvester with Powerflim RC7.2-75 PSA panels. For a 13-min flying test with a 170 mAh battery, the solar panel can charge it to 14% capacity, while the cantilever PFC harvester can charge the EH300's 4.6 mJ internal capacitor to 70% capacity [18]. The power extraction techniques of solar panels plus PVEH patches and their consumptions based internal architectures were investigated. In particular, the role of charge collectors for solar panels and PVEH patches were explained in the detailed manners. Apart from the charge collectors, the other important electronic components, which are linked in unmanned aircraft system, were provided [19–21]. The design procedures involved in the development of UAVs, such as estimation of payload weight, estimation of overall takeoff weight of UAV, design of propulsive system, design of UAV frame dimensions, design of landing gear, and design of other associates were discussed. The analytical procedures of said UAV design parameters were also provided [22–25]. Additional energy gainers for UAVs and their estimations on the development of voltages were studied. In particular, analytical and computational procedures for energy extractions through UAV propellers attached with PVEH patches were investigated. In addition, solar energy induction with respect to the flight conditions of UAV and its calculations stages were mentioned. Finally, wind rotors suitable for additional energy development in UAVs were also studied, in which both energy and exergy studies were focused predominantly. For electrical power development through PVEH patches, aerodynamic pressures impacted on the surfaces of the UAV and free vibrational frequencies, and their corresponding displacements of UAV parts, were played major contributor roles. For CFD, the types of initial and boundary conditions were given to the solver, the type of solver suitable for UAVs' working conditions, type of pressure and velocity coupler for solver, the type of initialization for the attainment of convergence in computational study, and the type of solver controls were obtained. For vibrational analysis, the type of input conditions needed, the type of supports applicable for UAVs, the type of remote displacements suitable for rotating components of UAV, and the selection of natural frequencies of UAV parts applicable for voltage calculations were demonstrated. Finally, the variations of composite materials suitable for hybrid UAVs and their different parts were studied. In addition to the primary composites, the relevant alloys were incorporated and obtained their properties. The important input properties such as dielectric constant rate, Young's modulus, Poisson ratio, and densities were noted for the determination of electrical voltages [26–45].

1.2. Summary, Observations and Contributions

The integration of energy sources for the enhancement of UAV endurance is possible; therefore, this work was finalized to impose hybrid energy mechanism in the outer surfaces of the hybrid UAV. From the comprehensive survey, it is understood that piezoelectric energy extraction through vibration of UAV parts and solar energy through solar panels imposed on outer surfaces of UAV are reliable. Thus, this work was shortlisted to impose piezoelectric patches and solar panels on the control surfaces of this UAV, wherein the occupation of both attachments is planned to share in an equal manner. Instead of experimental studies, this work was planned to impose integrated approach with an incorporation of advanced computational simulations and standard analytical calculations. In this regard, the detailed variables and their explanations, and also summaries, are collected and listed in Tables 1–4.

Table 1. The variable sand their descriptions imposed in this work.

Variables	Descriptions
$P^{General}_{Intermediate}$	Generalized power at intermediate level
d_{lwm}	Material constant for patches made-up of piezoelectric materials
w	Applicable natural frequency of the system
f	Aerodynamic force acting on the base structure
T_{PL}	Thickness of the piezoelectric patches
ρ_{lwm}	Density of the lightweight material
W_P	Width of the base structure

Table 1. *Cont.*

Variables	Descriptions
L_{PL}	Length of the piezoelectric patches
t_P	Thickness of the base structure
T	Temperature of the working environment
L	Length of the base structure
$P^{General}_{Final}$	Generalized power at final level
$F(t)_{aerodynamic}$	Various aerodynamic forces involved in the force balance equation
m_{UAV}	Total mass of the UAV
C_{UAV}	Damping coefficient of the material
K_{UAV}	Stiffness of the material
u	Vibrational displacement
u^a_l	Aerodynamic velocity in "x" direction
v^a_m	Aerodynamic velocity in "y" direction
w^a_n	Aerodynamic velocity in "z" direction
P_a	Pressure of the air fluid
μ	Bulk viscosity of the aerodynamic fluid
ρ_a	Density of the air fluid
ε	Dielectric constant of the patch material

Table 2. Comparative information about UAV's Design.

Reference	Configuration	Weight Ratios	Dimensions			Aerofoil Used
			Length	Breadth	Thickness	
[42]	Box wing	1.2 to 1.5	-	-	-	-
[43]	Fixed wing	1.175	-	-	-	NACA 63-512
[44]	Fixed wing	Overall weight of the UAV was 3.5 kg.	0.96 m	1.8 m	-	NACA 3414(w) & NACA 0012(ht)
[37]	Fixed wing	The thrust to gravity ratio was assumed as 1.3 and maximum weight to payload weight was assumed as 1.4.	-	-	-	-
[14]	Fixed wing and Multirotor	For CW-10 version, the takeoff weight was 12 kg and the payload weight was 2 kg; For CW-30 version, the takeoff weight was 34.5 kg and the payload weight was 6 kg; For DELTAQUAD version, the takeoff weight was 6.2 kg and the payload weight was 1.2 kg; For ZHIHANGV-330 version, the takeoff weight was 18 kg and the payload weight was 3 kg;	1.8 m 2.4 m	4.6 m 2.74 m	- 0.6 m	- -

Table 2. *Cont.*

Reference	Configuration	Weight Ratios	Dimensions			Aerofoil Used
			Length	Breadth	Thickness	
[7]	Fixed wing	The thrust to weight ratio was 2.17 and the power to weight ratio was 610 W/kg.	-	1.6 m	-	NACA 23012
[38]	Fixed wing	-	1.6 m	2.52 m	-	-
[9]	Fixed wing	total weight was 3.155 kg	1.4 m	4 m	-	SD5060
[6]	Fixed wing (BWB)	Overall weight of the UAV was 47 kg	1.8 m	5.2 m	1.25 m (h)	MH922 MH78 NACA 04012
[39]	Prop for Hexacopter	The thrust to weight ratio was 2 (individual prop 5 kg).	-	-	-	-
[15]	Fixed wing (Tilt wing)	total wt. = 1 kg	-	-	-	NACA 0012
[13]	Fixed wing	Overall weight of the UAV was 2.3 kg	1 m	1 m	-	NACA 2412 NACA 0012(ht)
[40]	Fixed wing (BWB)	For first case, the overall weight of the UAV was 3.3 kg and the power to weight ratio was 0.826 hp/kg. For second case, the overall weight of the UAV was 3.5 kg and the power to weight ratio was 0.24 hp/kg.	-	2 m 1.8 m	-	EPPLER637 MH 81
[18]	Box wing	Max thrust was 3.35 kgf	1 m	-	-	NACA 0012
[45]	Blended wing	The thrust to weight ratio was 1.3. Overall weight of the UAV was 46 kg. The nominal payload was 8 kg. The endurance (with 10 kg) was 95 min and endurance (with 5 kg) 135 min.	1.82 m	-	-	-
[20]	Delta wing Canard wing	Overall weight of the UAV was 30 kg.	-	-	-	NACA 6214
[22]	Fixed wing	-	-	-	-	E186, HS 522, MH60, MH78, MH82, MH92, S 5020
[1]	multirotor	Total weight was 1 kg	0.45 m	0.5 m	-	-
[17]	fixed wing		-	4 m	-	-
[13]	fixed wing	flying weight was 0.9 kg	1.1 m	1.8 m	-	-
[5]	fixed wing(rectangular)	Overall weight of the UAV was 5 kg	1.852 m	4 m	0.53 m	SG6043

Table 3. Comparative information about parameters of CFD and FEA analysis on UAVs.

Reference	Types of Mesh Used	Type of Turbulence Model	Boundary Conditions	Extracted OUTCOMES	Reference	Types of Mesh Used	Type of Supports Given and Loads Applied	Type of Conditions Imposed [Steady/Transient]	Materials Imposed	Extracted Outcomes
[37]	Fine Unstructured	k-epsilon	Velocity, 5 m/s	pressure, velocity	[37]	fine unstructured	fixed support and aerodynamic pressure	transient	CFRP-UD-Wet based 10 × 10 inch CFRP-Woven-Prepreg based 20 × 22.5 inch	modal analysis-total deformation
[38]	Unstructured tetra	Transitional SST	Velocity inlet and pressure outlet	C_L, C_D, velocity, iso-surface of vorticity	[39]	fine unstructured	aerodynamic pressure	transient	GFRP, Aluminum alloy and CFRP materials	Modal analysis-total deformation
[6]	-	k-epsilon Enhanced Wall Treatment turbulence model	-	C_L, C_D, Velocity contours of the coaxial fan	[41]	-	Fixed support and Bending Torsional	-	Aluminum alloy 6061-T6	Max deformation observed 4.33 mm
[39]	Fine Unstructured	-	velocity, 5 m/s	velocity, pressure	[2]	Smooth, fine structured	-	transient	PZT-5A type Macro Fiber Composites	elastic strain
[40]	Unstructured Tetra	RANS coupled Spalart-Allmaras	-	C_L, C_D						

Table 4. Comparative information about components involved in UAVs.

Reference	Battery Rate	KV Rate of Motor and ESC Rate	Dimensions of Propeller	Other Component Details
[43]	48 A,22.2 V, 20,000 mAh	-	-	Propeller's pitch to diameter ratio was 0.8.
[44]	600 mAh, 3 s	-	-	Pixhawk FCU, Transmitter and receiver 2.5 GHz
[37]	-	MR-960 FW-880	MR-9 × 4.5 FW-10 × 4.7	Pixhawk FCU, automatic antenna tracker, Telemetry-915 MHz, 32 kms
[7]	6S-2P, 10,000 mAh	970 min^{-1}; max power-740 W	APC TE 9 × 5	Pixhawk
[9]	-	0.3 Nm, 2000 RPM	-	Pixhawk
[39]	4S Li Po	280 KV and 30 A	20 × 4.5	-
[15]	-	-	10 × 4.5	-
[15]	12.6 V–5000 mAh	1500 KV and 40A	10 × 4.5-inch m^2 and 10 × 4.5-inch	Transmitter and receiver 2.5 GHz—6 channel
[17]	-	-	-	Multispectral cameras 4200 pixels by 2800 pixels
[18]	Li-Po battery 6S with 10,000 mAh and 15C	-	13 × 6	-
[23]	-	-	25.40 diameter and speed of propeller is 34.3 m/s	GT2213-09KV1180—used motor
[8]	Cell 4.2 V 4 mAh	-	-	self-charging structure is 1100-O aluminum alloy with dimensions of 63.5 mm × 25.4 mm × 0.127 mm and a mass of 0.555 g; active piezoelectric element of 45.97 mm × 20.57 mm × 0.254 mm, and a mass of 2.267 g
[1]	-	850 KV	10-inch dia	L3GD20- angular rate sensor with 3 axes of low power
[11]	thin Li film 0.7 mAh	-	-	-
[17]	3S, Li-Po, 11.1 V	-	-	GVP8 Li, 14.2 Boost MPPT, solar power c60 PV cells
[9]	6S, Li-Po, 7660 mAh	-	-	-
[13]	Li-Po, 170 mAh	-	-	EH300 energy harvesting chip.

2. Proposed Methodologies—Energy Drone

This study made an original contribution by proposing the idea of an energy drone, in which the majority of an energy drone's power requirements can be met by drawing electricity from renewable sources, such as solar panels and piezoelectric energy harvesters. Traditional propellant engines will be used for the takeoff and landing phases of the energy drone's operation, while hybrid renewable energy extractors will be used for all other phases of the drone's operation. This proposed energy drone will have a propulsion system that is comprised of two components. As a result of the requirement for additional base parts of UAVs in order to harvest a greater quantity of energy, the double-winged, tandem-configured hybrid UAV has been shortlisted for the development of the energy drone. The primary and secondary design parameters of a hybrid UAV have been derived with the assistance of standard calculations and design techniques, and those values have been enforced during the modeling phases. Figure 1 provides a methodical breakdown of the infrastructure that underpins the hybrid energy system that is imposed on the hybrid drone's power supply [20,21]. The authors intend to employ the cumulative voltages (PVEH patches plus Solar panels) for real-time applications that are based on UAVs through the implementation of this planned architecture. The hybrid system that is being considered can potentially generate electrical power, which it is intended to store in a variety of different batteries in the future. In addition to this, it is intended to install independent charge controllers between the panels (both solar and PVEH) and the batteries. Consequently, the DC current is very amenable to storage in batteries. Following the batteries, the supplementary energies that have been extracted can finally be settled in the power distribution board, which is where the necessary communication voltages have been framed. The framed voltages of either 5 V or 3.3 V are going to be used in a variety of avionics systems, including the flight control system, the navigation system, the air data system, and the communication system. The schematic representations of this proposed energy drone are shown in Figures 2 and 3.

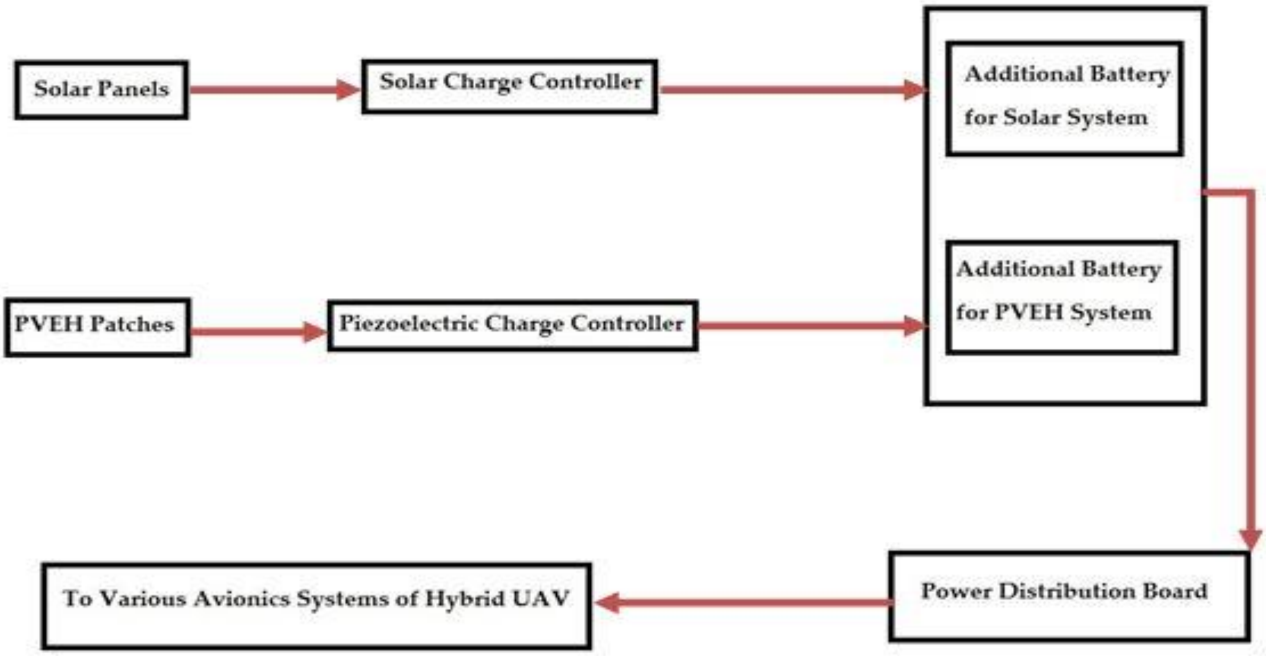

Figure 1. A systematic view of the proposed architecture of Hybrid Energy for Hybrid Energized Drone.

2.1. Proposed System—Renewable Energized Drone

In order to attain and enhance the energy harvesting technique, the PVEH patches are imposed on the half of the tandem wing and further imposed on the vertical tail from the tip, in which the PVEH patch occupies half of the span of the vertical tail. The typical proposed concepts of the imposition of PVEH patches on wing and vertical stabilizer of hybrid UAV are pictorially revealed in Figures 4 and 5.

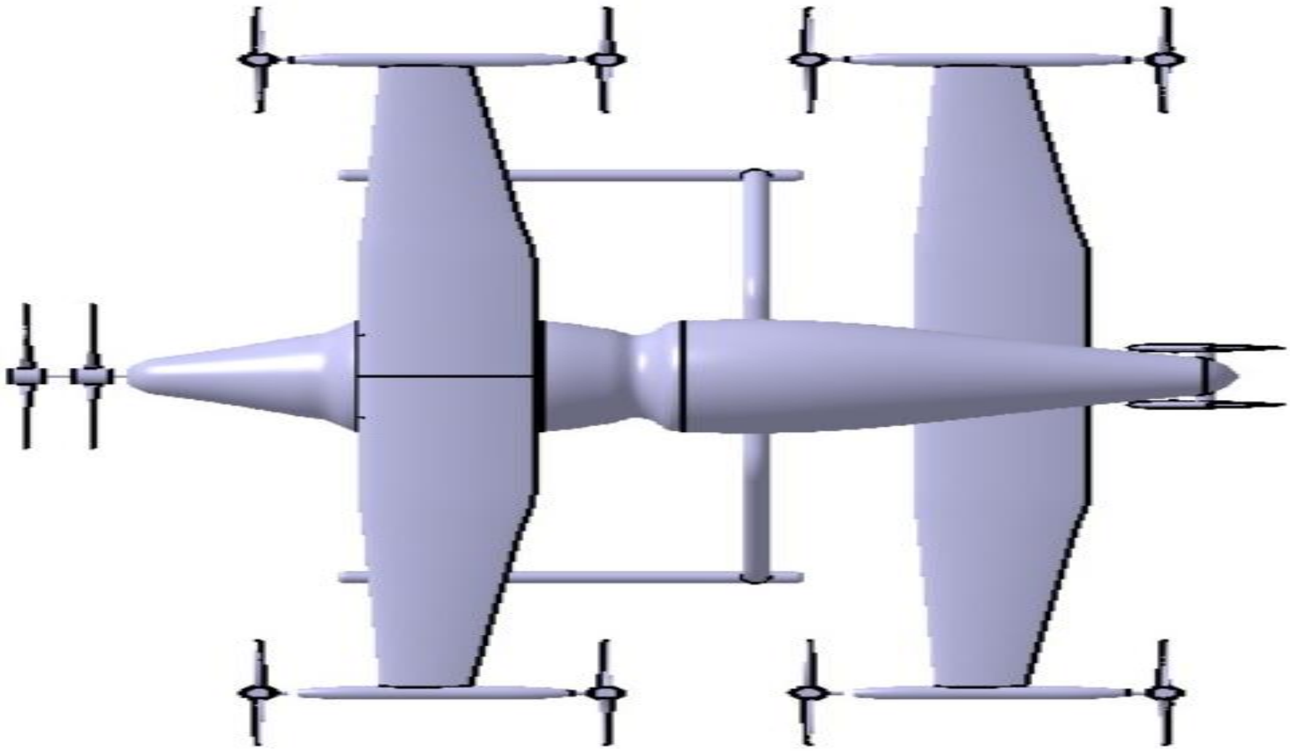

Figure 2. Top view of VTOL and normal cruise.

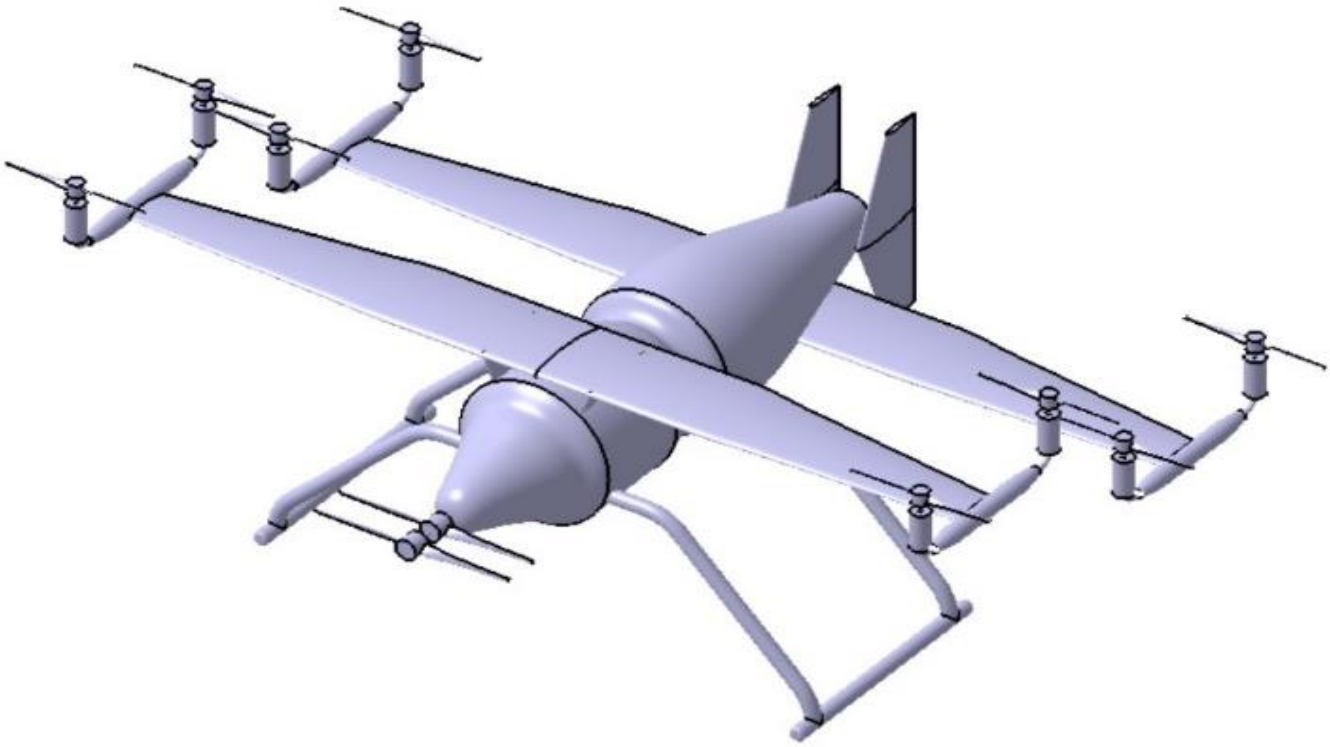

Figure 3. Isometric view of VTOL and normal cruise.

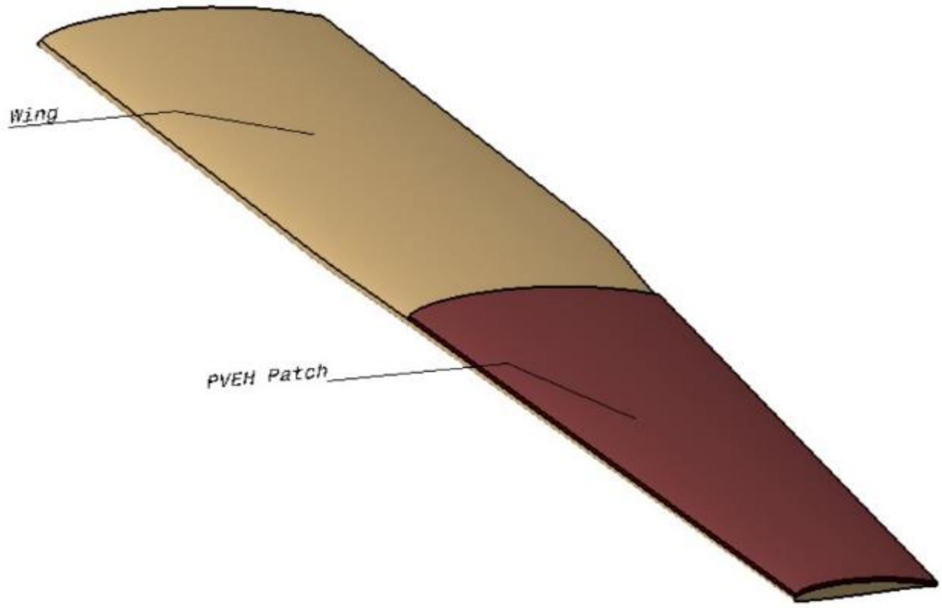

Figure 4. Graphical representation of the placement of PVEH patch on the top of the wing.

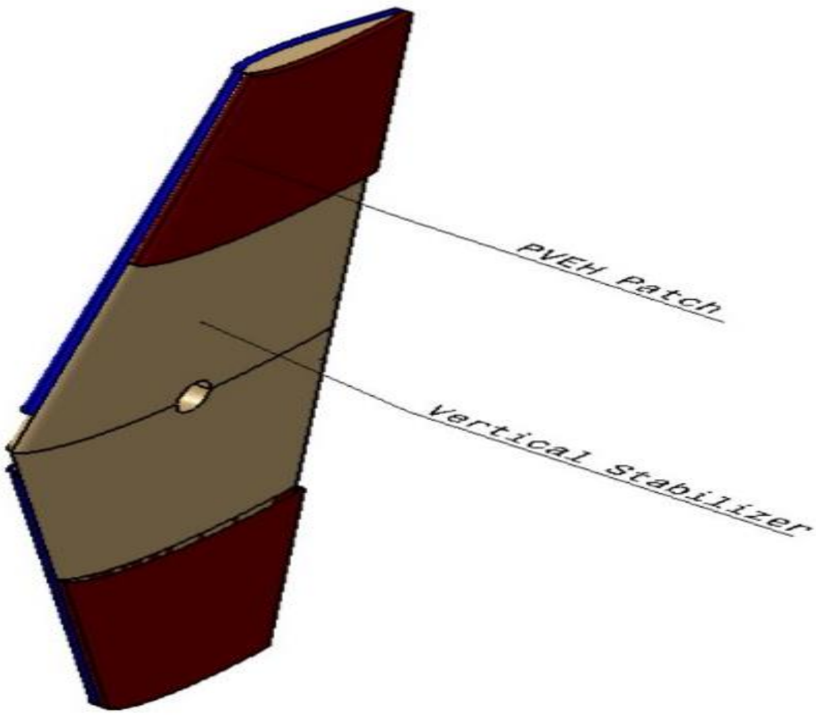

Figure 5. Graphical representation of the placement of PVEH patch on the side of the VS.

Aside from the PVEH patches, solar panels are also planned to impose on the same wings and vertical stabilizers so the proposed hybrid energy systems are pictorially revealed in Figures 6 and 7.

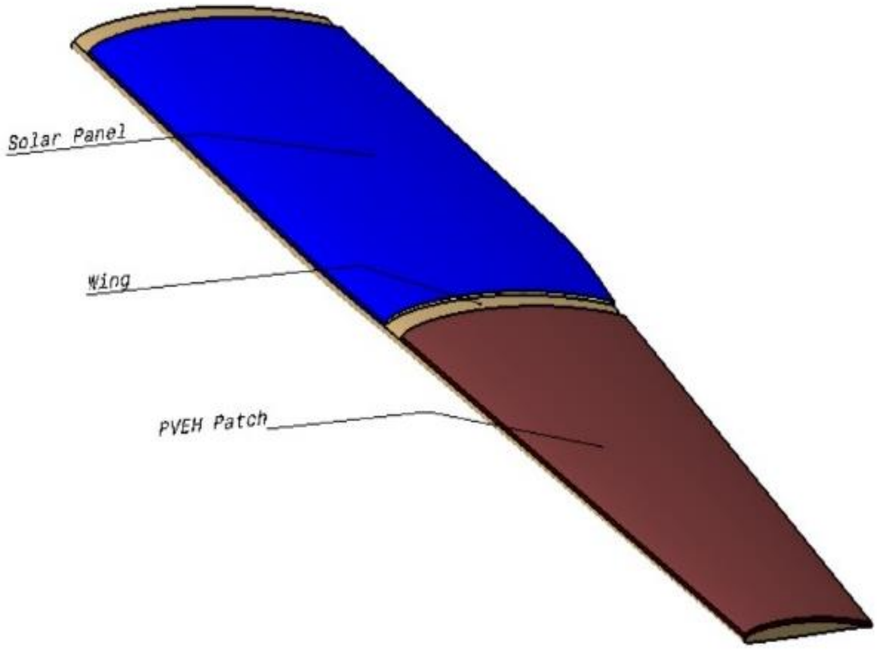

Figure 6. Graphical representation of the placement of a solar cell on the top of the wing.

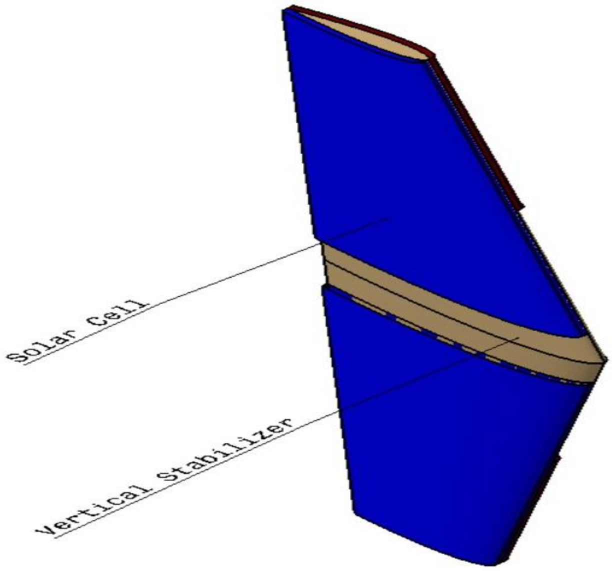

Figure 7. Graphical representation of the placement of a solar cell on the side of the VS.

2.2. Proposed Scheme—Integrated Energy Approach

A uniquely integrated energy approach is proposed in this work, wherein the computational and analytical methods are integrated in order to extract and estimate the energy level through PVEH patches. Equations (1) and (2) include the essential analytical elements of the PVEH patch's contribution to the generation of electricity. These elements were developed and described in the literature study [15,16,25]. The fluid dynamic pressure-based evenly distributed loads, natural frequencies, and dielectric constants are the three important inputs. The pressure and free vibration frequency are computed through CFD and CVA, respectively, while the dielectric constants are obtained from a survey of the relevant literature [15,16,25]. The calculations for the generation of power have been updated. At this time, the maximum amount of electrical power that can be extracted is 196 W. The writers had faith that this novel method of electricity extraction was trustworthy. This effort involves two significant components, the first of which is an increase in the level of power extraction, which is more than in other instances. The first factor to consider is the design specifications of the base object, specifically the wingspan of the hybrid UAV, and the second factor is the strong hydrodynamic pressures that are impacting on the skin of the UAV. As a result of the fact that Equations (1) and (2) have previously been validated [15,16,25], only the validated connections are used in this work.

$$P^{\mathrm{General}}_{\mathrm{Intermediate}} = d^2_{\mathrm{lwm}} w^2 f^2 \times \frac{18 \times T_{\mathrm{PL}}}{[(W_{\mathrm{P}}) \times (L_{\mathrm{PL}})^2 \times ([t_{\mathrm{P}}] + [T_{\mathrm{PL}}])^4]} \times \frac{\rho_{\mathrm{lwm}}}{[1 + f \times \varepsilon \times (\rho_{\mathrm{lwm}})]} \quad (1)$$

$$P^{\mathrm{General}}_{\mathrm{Final}} = \left(P^{\mathrm{General}}_{\mathrm{Intermediate}}\right) \times \left(\frac{(0.44L)^5}{36} - \frac{L(0.44L)^4}{6} + \frac{5L^2(0.44L)^3}{12} - \frac{L^3(0.44L)^2}{2} + \frac{L^4(0.44L)}{4}\right) \quad (2)$$

The reference model of the Murder Hornet hybrid UAV was forced upon the CFD investigation. ANSYS was used to do the CFD analysis. Unstructured tetrahedral particles are utilized for the meshing process. Several computational factors are examined and analyzed. In the first step of the process, a steady-state flow study is performed on the MH Hybrid UAV. To ensure that this UAV has an adequate amount of thrust, a transient flow study, in particular for the propeller, is being performed.

2.2.1. Computational Fluid Dynamics

The CFD work is carried out in ANSYS. Initially, the computational model of hybrid UAV is imported. The upstream and downstream dimensions of the control volume are given as 2.5 D and 5 D, respectively. Figure 8 reveals the typical view of the imposed boundaries of control volume, wherein the dimensions of control volumes are framed with respect to the primary design parameter of the computational model (hybrid UAV).

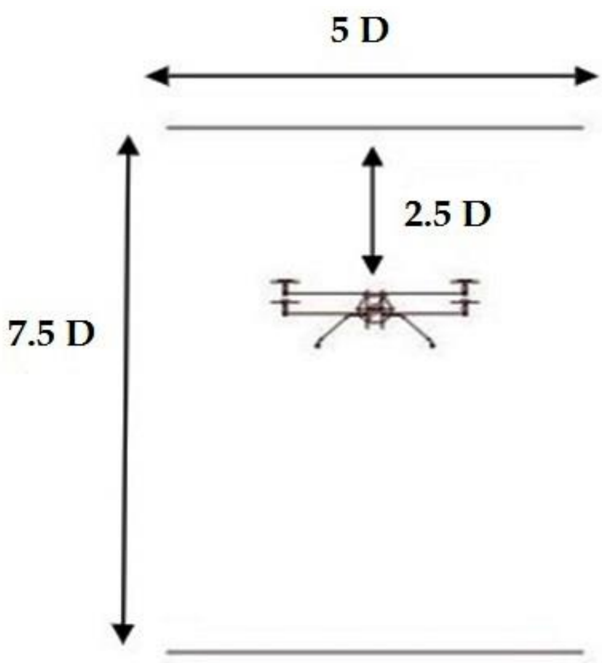

Figure 8. Dimensions of the imposed control volume.

Unstructured Tetrahedral mesh is used for its complex design, as shown in Figure 9, in which the fine meshes are developed at nearby the regions of UAV. Since this UAV has the effect of fluid structure interaction, an additional concern has been given at discretization phase.

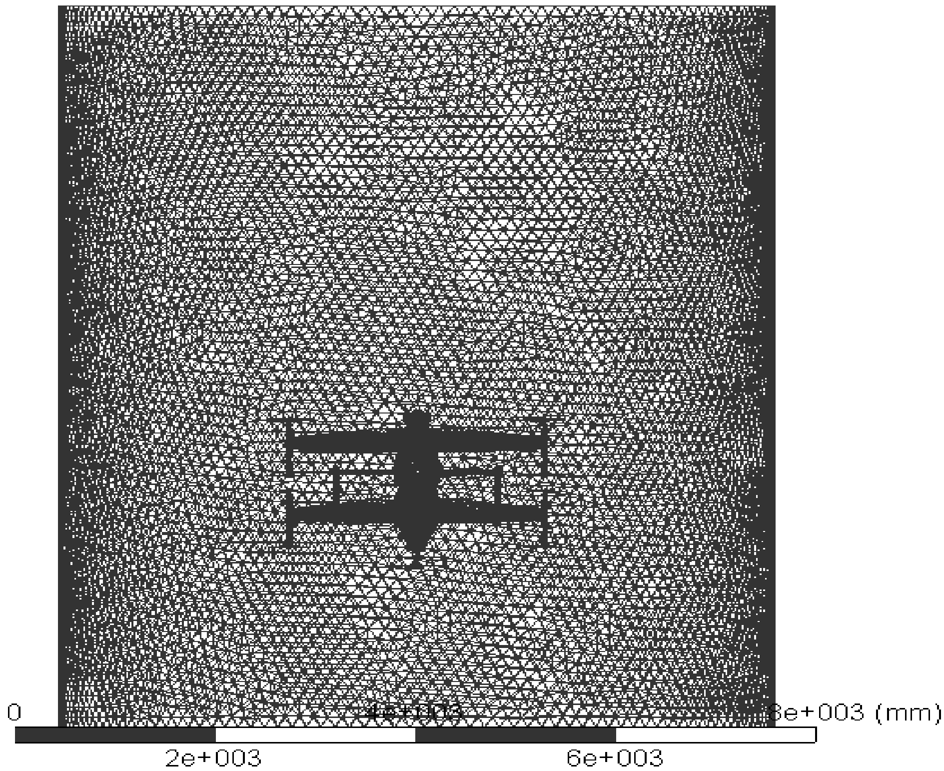

Figure 9. Discretization of the model.

The authors proposed five different maneuvering cases, under these 5 cases two inlet velocities are taken into consideration. The detailed inlet velocities-based boundary conditions are listed in Table 5. The k-epsilon turbulence model is imposed for the computational fluid dynamics analysis. The pressure outlet is assumed with zero pressure and operating pressure is given as regular pressure data.

Table 5. Boundary conditions for MH hybrid UAV.

Cases	Boundary Condition (Inlet Velocity)	
	Min (m/s)	**Max (m/s)**
Vertical take-off and landing without payload	15	27.78
Normal cruise without payload	15	27.78
Super cruise without payload	33.33	41.67
Normal cruise with payload	15	27.78
Super cruise with payload	33.33	41.67

In order to estimate the desired thrust of the UAV, the authors proposed moving reference frame (MRF) analysis for the propeller. Four different operating conditions are chosen. Unstructured tetrahedral mesh is used, and control volumes are generated near the tip of the propeller and whole domain, respectively. The CFD analyses have been conducted using the ANSYS Fluent tool. The authors have applied pressure-based incompressible flow solver. For acquiring accurate results, second order upwind spatial discretization has been used. The governing equations is the mathematical formula which helps to perform the computational simulations. For modeling, they manage the expected behavior of fluids in the surface provided by the code. Governing equations are the theoretical approximations for describing the fluid flow and their components. The simplified term of continuity and momentum equations are presented in Equations (3) and (5). The complete

Reynolds-averaged-Navier-stokes (RANS) relationships are shown in Equations (11)–(14) and Equation (15) implies the finite volume approach-based relationship.

$$\nabla\cdot\vec{V}_a = 0 \tag{3}$$

$$\frac{\partial(u_l^a)}{\partial x} + \frac{\partial(v_m^a)}{\partial y} + \frac{\partial(w_n^a)}{\partial z} = 0 \tag{4}$$

$$-\nabla P_a + \mu\nabla^2\vec{V}_a + F = \rho_a\left(\vec{V}_a\cdot\nabla\right)\vec{V}_a \tag{5}$$

$$\rho_a\left(\vec{V}_a\cdot\nabla\right)(C_V T) = k\nabla^2 T + \mu\varphi \tag{6}$$

$$\nabla\cdot\left(\rho_a\vec{V}_a\right) = 0 \tag{7}$$

$$-\nabla P_a + \mu\nabla\left(\nabla\vec{V} + \nabla\vec{V}^T\right) - \frac{2}{3}\mu\nabla\left(\nabla\cdot\vec{V}_a\right) = \rho_a\left(\vec{V}_a\cdot\nabla\right)\vec{V}_a \tag{8}$$

$$\rho_a\left(\vec{V}_a\cdot\nabla\right)(C_V T) = k\nabla^2 T - P_a\left(\nabla\cdot\vec{V}_a\right) + \mu\varphi \tag{9}$$

$$\rho_a = \frac{P_a}{RT} \tag{10}$$

RANS Equations for incompressible flow,

$$\nabla\cdot\overline{u} = 0 \tag{11}$$

$$\rho_a\,\overline{u}\cdot\nabla(\overline{u}) = -\nabla\,\overline{p} + \nabla\cdot\left(\mu\left(\nabla\overline{u} + \nabla\overline{u}^T\right) - \rho_a\overline{u'\,u'}\right) + \overline{F} \tag{12}$$

RANS Equations compressible flow,

$$\frac{\partial\rho_a}{\partial t} + \frac{\partial}{\partial x_l}\left(\overline{\rho_a}\widetilde{u_i}\right) = 0 \tag{13}$$

$$\frac{\partial}{\partial t}\left(\overline{\rho_a}\widetilde{u_i}\right) + \frac{\partial}{\partial x_j}\left(\rho_a\widetilde{u_j}\widetilde{u_i}\right) = -\frac{\partial\overline{\rho_a}}{\partial x_l} + \frac{\partial}{\partial x_m}\left(\widetilde{\sigma}_{lm} - \overline{\rho_a u_j'' u_i''}\right) \tag{14}$$

Numerical integration,

$$\frac{\partial}{\partial t}\iiint U\,dV = -\oiint \vec{F}\cdot\vec{dS} + \iiint Q\,dV \tag{15}$$

2.2.2. Computational Free Vibrational Analyses

The full model is analyzed with various materials. Firstly, fixed supports are given to the model. Later, it is subjected to free vibration. With the help of modal analysis, the frequency of the respective material is determined which is used to estimate the power of PVEH material.

A typical top view based computational model of the vibrational analysis is revealed in Figure 10. The unstructured based discretized structure of the hybrid UAV is shown in Figure 11 also the imposed boundary condition is listed in Figure 12.

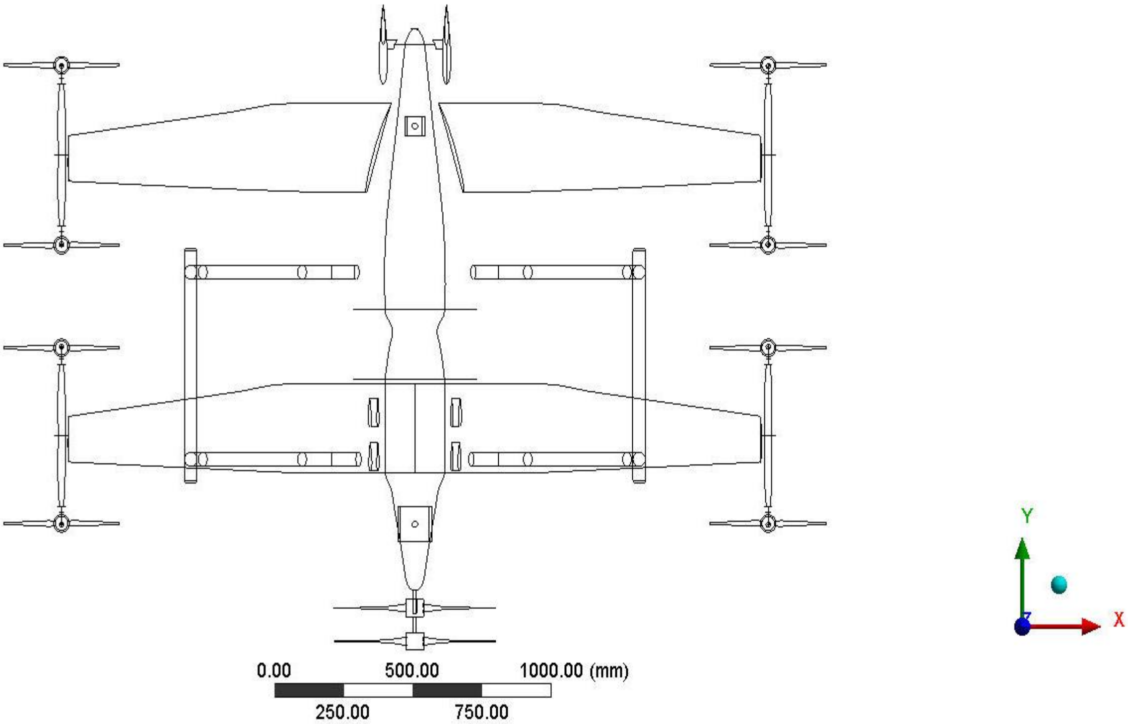

Figure 10. A typical top view of the computational model focused for vibrational analyses.

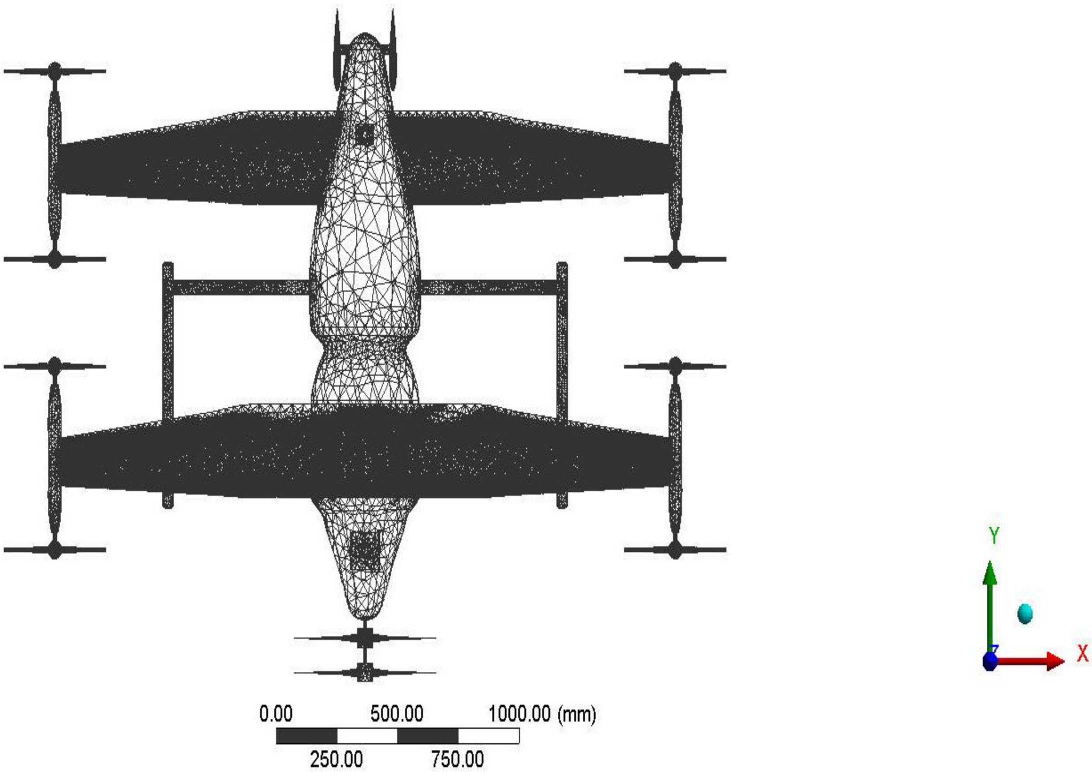

Figure 11. A typical top view of discretized hybrid UAV for vibrational analysis.

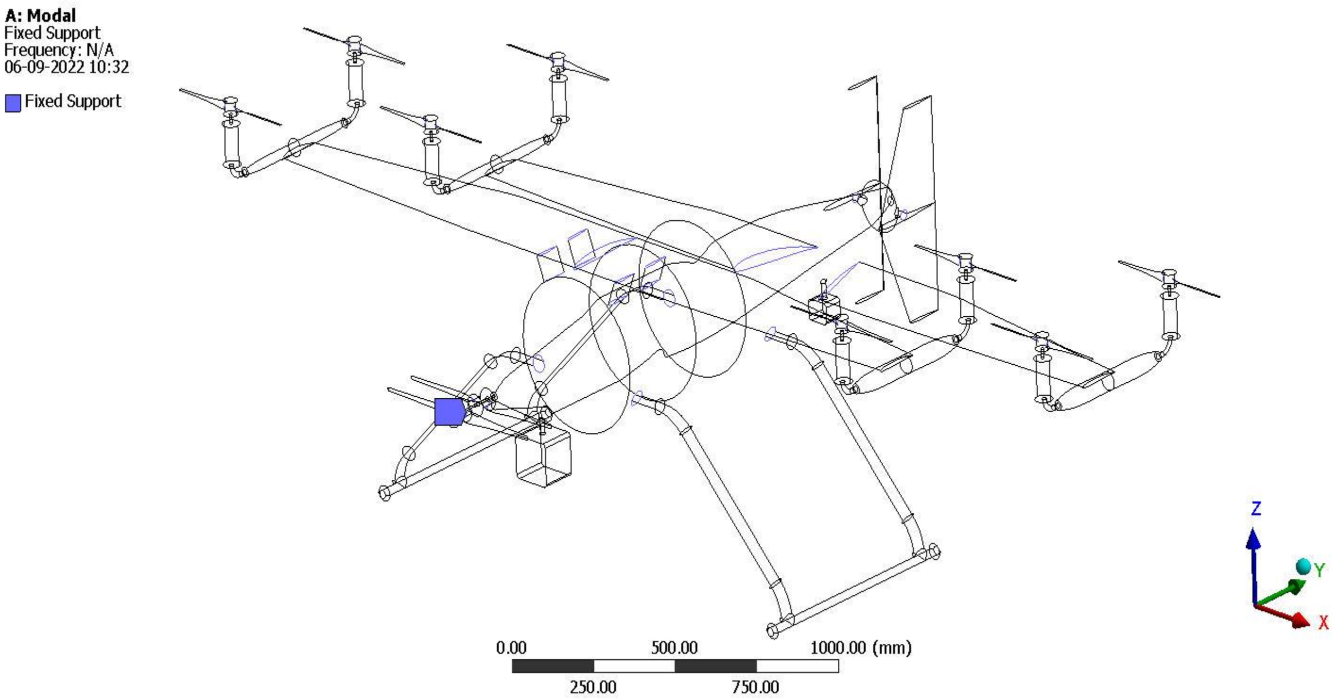

Figure 12. A typical isometric view-based representation of imposed boundary conditions on the UAV.

Learning how to identify a structure's inherent resonance frequencies and mode shapes is important. The study of modes is known as a linear dynamical analysis. The fundamental equation of motion is always used as a starting point when calculating the dynamic reaction of a structure, where the unknowns are the structure's overall acceleration, velocity, and position at each location. The major governing equation is given in Equation (16).

$$[m_{\mathrm{UAV}}]\left\{\frac{d^2u}{dx^2}\right\} + [C_{\mathrm{UAV}}]\left\{\frac{du}{dx}\right\} + [K_{UAV}]\{u\} = \left\{F(t)_{aerodynamic}\right\} \quad (16)$$

Modal analysis requires that the resonance frequency and mode forms do not depend on the external load, and thus set it to zero. Since complex numbers are required to represent the morphologies of natural frequencies and modes when damping is present, its effects are being disregarded for the time being. The first optimized governing equation of modal simulation is given in Equation (17).

$$[m_{\mathrm{UAV}}]\left\{\frac{d^2u}{dx^2}\right\} + [K_{\mathrm{UAV}}]\{u\} = 0 \quad (17)$$

From the perspective of time domain dynamics, this problem describes either a body at rest or a body moving at a constant speed. If you solve it, you would not learn anything useful about velocity change or acceleration. Thus, $\left\{\frac{d^2u}{dx^2}\right\}(t) = 0$; the simplified governing equation (Equation (18)) involved in the modal computation is,

$$[K_{\mathrm{UAV}}]\{u\} = 0 \quad (18)$$

2.2.3. Experimental Validation

To determine the effectiveness of computational work, a comprehensive study of experimental analysis is carried out. The authors proposed an experimental setup, where the MIDE quick pack qp10w are used. The power extracted in this research is 2.5 mW. Thus, to compare the experimental setup to validate the computational work, a 3-D model of this experimental setup is designed with the help of CATIA and analyzed in ANSYS

17.2, respectively. The boundary conditions and material properties are proposed by the authors, followed by the CFD simulation modal analysis is carried out to determine the frequency of the respective material. The established studies of aerodynamic analysis and modal analysis are given and clearly depicted in Figures 13–16 [26].

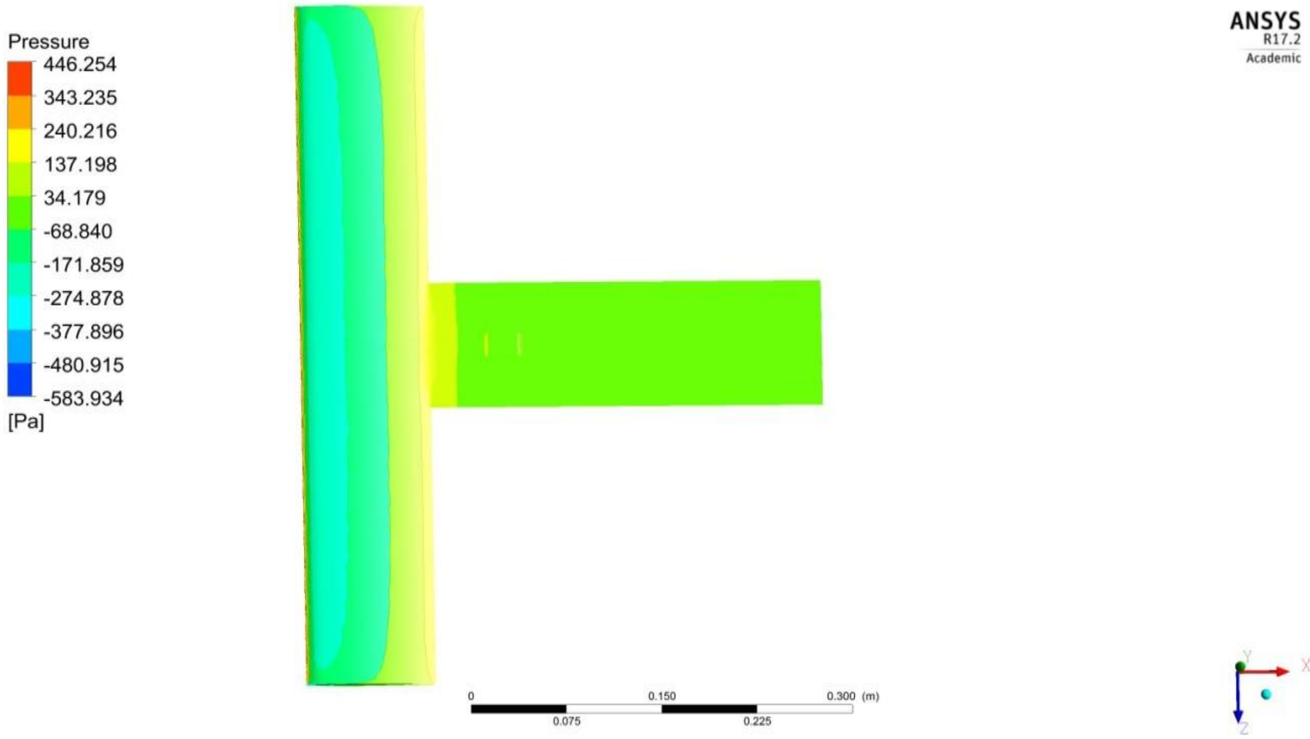

Figure 13. Pressure distribution on the proposed experimental setup.

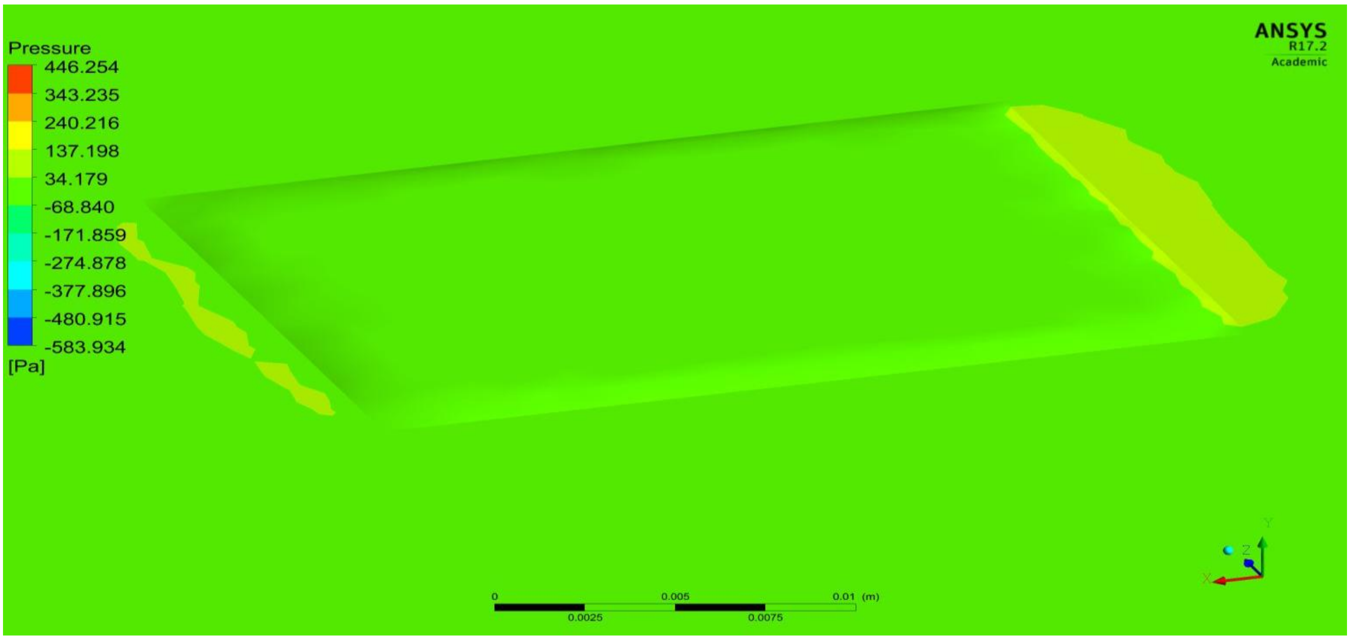

Figure 14. Pressure distribution on the quick pack PVEH patch.

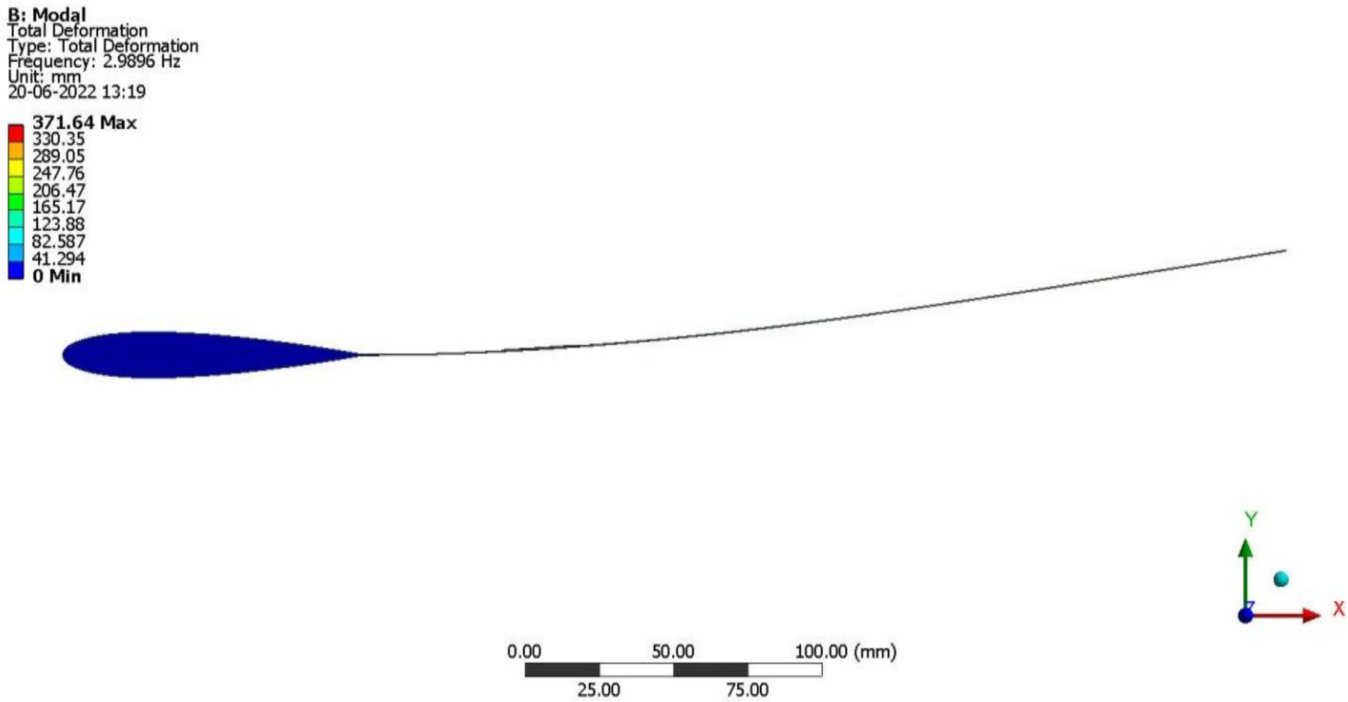

Figure 15. Total deformation of the proposed experimental setup under free vibration.

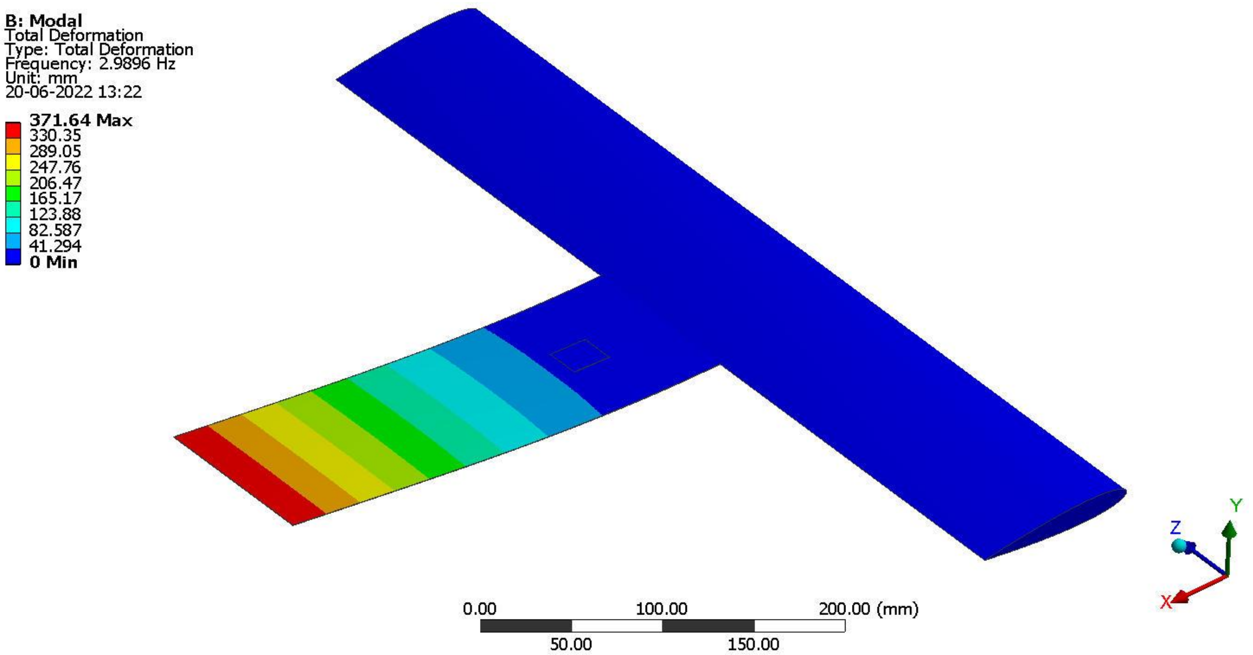

Figure 16. Total deformation of the proposed experimental setup under free vibration.

With the help of the computational simulation, necessary values for the calculation are derived. The sample calculation material is taken as Quick pack QP 10W. The predicted computational outcome-based data are substituted in Equations (19) and (20).

$$P^{\text{Validation}}_{\text{Intermediate}} = d^2_{pmc} w^2 f^2 \times \frac{18 \times T_{PL}}{\left[(W_P) \times (L_{PL})^2 \times ([t_P] + [T_{PL}])^4\right]} \times \frac{\rho_{lwm}}{[1 + f \times \varepsilon \times (\rho_{lwm})]} \quad (19)$$

where, Piezoelectric material constant (d_{pmc}) = 120 for PZT; the pressure on the piezoelectric patch is determined as 34.179 N/m^2, respectively. Therefore, Force (f) = Pressure

$\times$ Surface area = (34.179 $\times$ 0.031) + (34.179 $\times$ 0.031) + (34.179 $\times$ 0.0001023) + (34.179 $\times$ 0.0001023) + (34.179 $\times$ 0.0000333) + (34.179 $\times$ 0.0000333) = 1.07903103 N; natural frequency (w) = 2.9896 Hz; width of the cantilever beam (W_P) = 0.101 m; length of the piezoelectric layer (L) = 0.0254 m; thickness of the cantilever beam (t_P)=0.00039 m; thickness of the piezoelectric (T_{PL}) = 0.00025 m; density of the material (ρ_{lwm}) = 7500 kg/m^3; thereby,

$$P^{Validation}_{Final} = \left(P^{Validation}_{Intermediate}\right) \times \left(\frac{(0.44 \times L)^5}{36} - \frac{L(0.44 \times L)^4}{6} + \frac{5L^2(0.44 \times L)^3}{12} - \frac{L^3(0.44 \times L)^2}{2} + \frac{L^4(0.44 \times L)}{4}\right) \quad (20)$$

On substituting the necessary values in the equation, the estimated power is 2.3 mW, respectively; therefore, 8% of error occurred in computational analysis compared to experimental work. The comprehensive outcome of experimental data and our own proposed data are listed in Table 6. From Table 6, it is clearly understood that the error percentage is within the acceptable limit, so this work proposed approach (mathematical cum analytical) is capable to extract electrical energy with the help of PVEH patches.

Table 6. The validation of electrical power extractions through experimental and computational outcomes [15,16,25,26].

Experimental Results of Developed Electrical Power (mW)	Results of Developed Electrical Power through this Proposed Approach (mW)	Error Percentage
2.5	2.3	8

After the successful validation of this imposed integrated approach, the authors are finalized to extend this validated integrated approach to various real time applications. Firstly, the same approach is implemented in the nature-inspired hybrid UAV.

3. Results and Discussions

3.1. Computational Fluid Dynamics Results

Based on the CFD analysis, the aerodynamic characteristics of the MH hybrid UAV were studied for discussed four cases. The maximum and minimum velocity for the VTOL case is 27.78 m/s and 15 m/s, respectively. The same condition relies on the forward-normal cruise condition. For the super cruise case, the UAV has the minimum velocity of 33.33 m/s and maximum velocity of 41.67 m/s, respectively. The aforesaid all the cases are solved in ANSYS Fluent, and thereby the needful aerodynamic pressures on the various parts of the UAV are computed. The aerodynamic results of various maneuvering cases are revealed in Figures 17–22. Generally, aerodynamic pressures are considered as external loads under uniformly distributed loads (UDLs), wherein these UDLs need to be considered as concentrated loads with the inclusion of this impacted area on UAV parts.

3.2. Modal Analysis Results

The modal analysis is the fundamental dynamic analysis type, providing the natural frequencies at which a structure will resonate. These natural frequencies are of paramount importance in various engineering fields. In the modal analysis Al alloy, GFRP-fabric, CFRP-UD-Wet, CFRP-UD-Pre, CFRP-Wn-Pre, KFRP-UD-49, CFRP-Wn-Wet, GFRP-E-UD, GFRP-E-Wet, and GFRP-S-UD, FR 4 are used. The typical vibrational results of PVEH patched parts such as front wing, rear wing, and vertical stabilizer of UAV for various lightweight materials are revealed in Figures 23–55. In addition, the comprehensive outcome of natural frequencies and their corresponding vibrational displacements are listed in Tables 7 and 8, respectively.

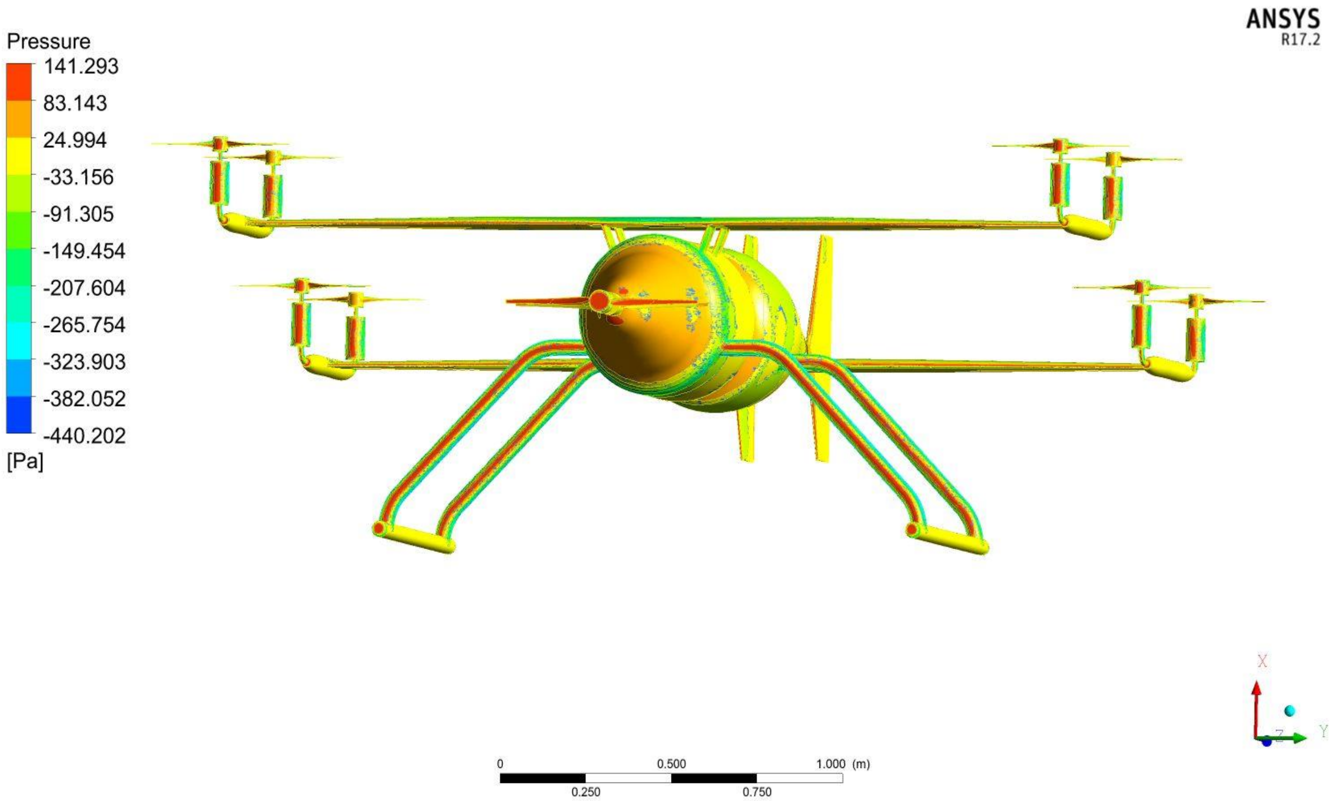

Figure 17. Pressure variation on the UAV at steady state- Normal cruise 15 m/s.

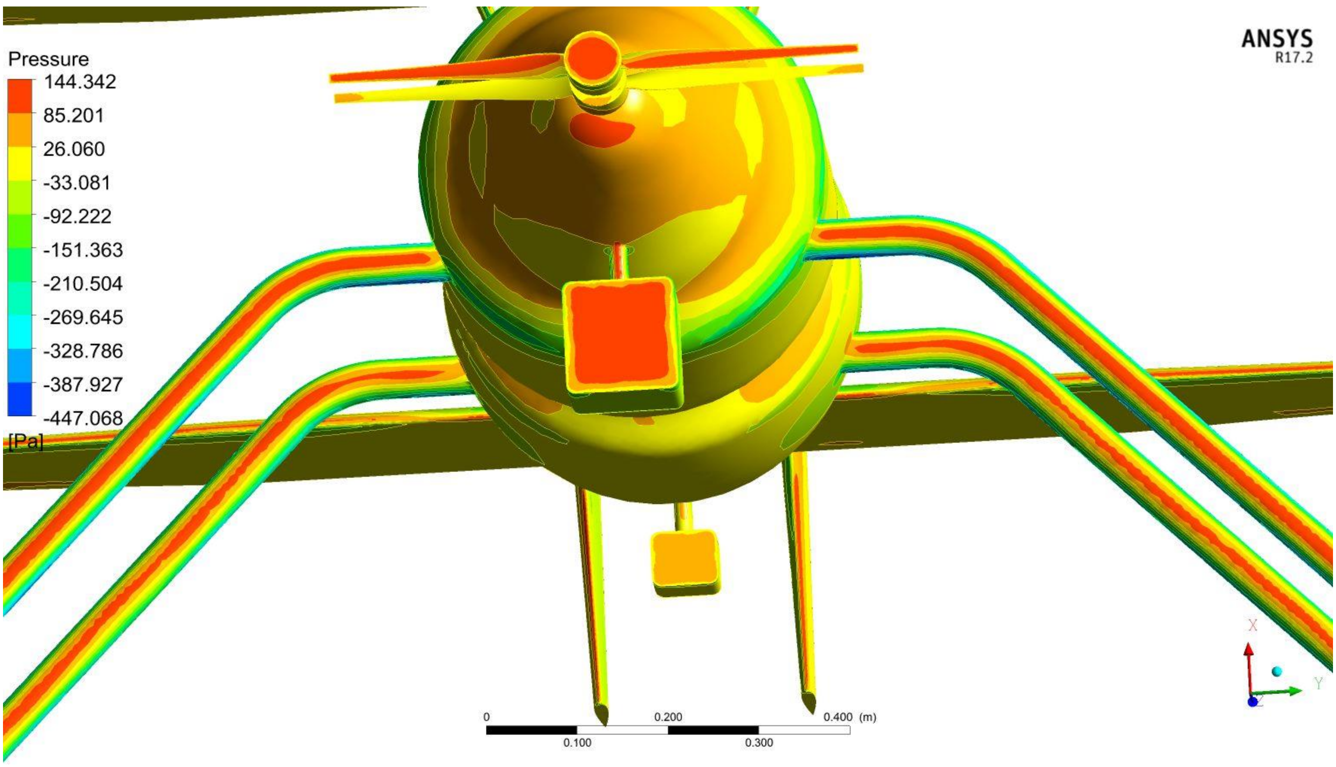

Figure 18. Pressure variation on UAV at steady state- Normal cruise with payload 15 m/s.

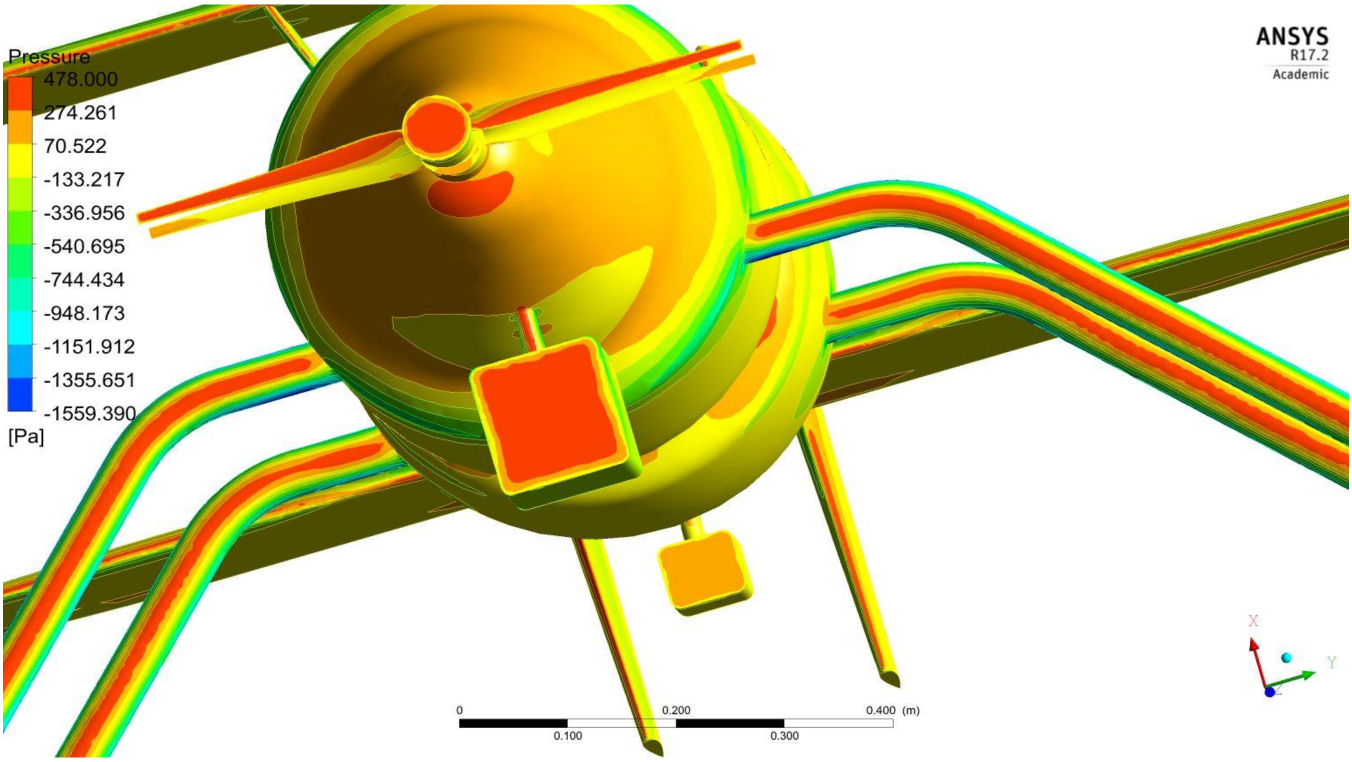

Figure 19. Pressure variation on UAV at steady state- Normal cruise with payload 27.78 m/s.

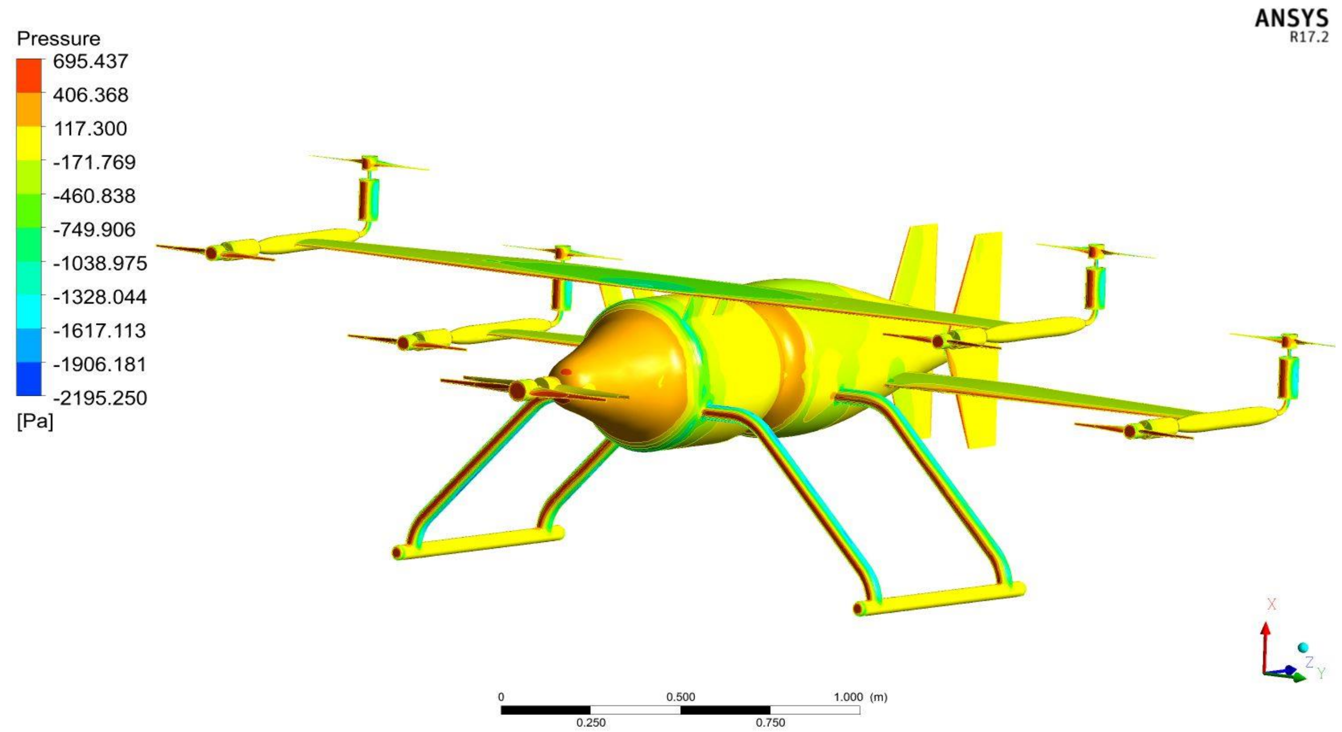

Figure 20. Pressure variation on the UAV at steady state- Super cruise 33.33 m/s.

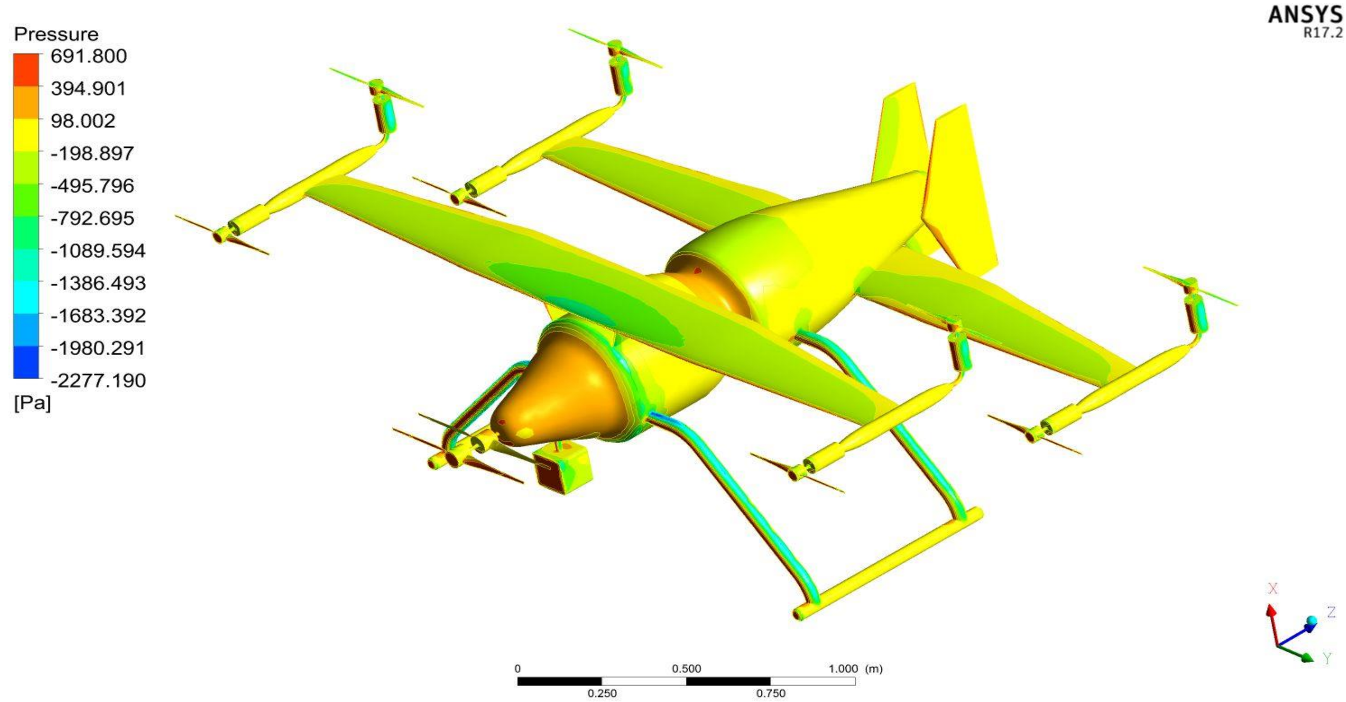

Figure 21. Pressure variation on the UAV at steady state- Super cruise with payload 33.33 m/s.

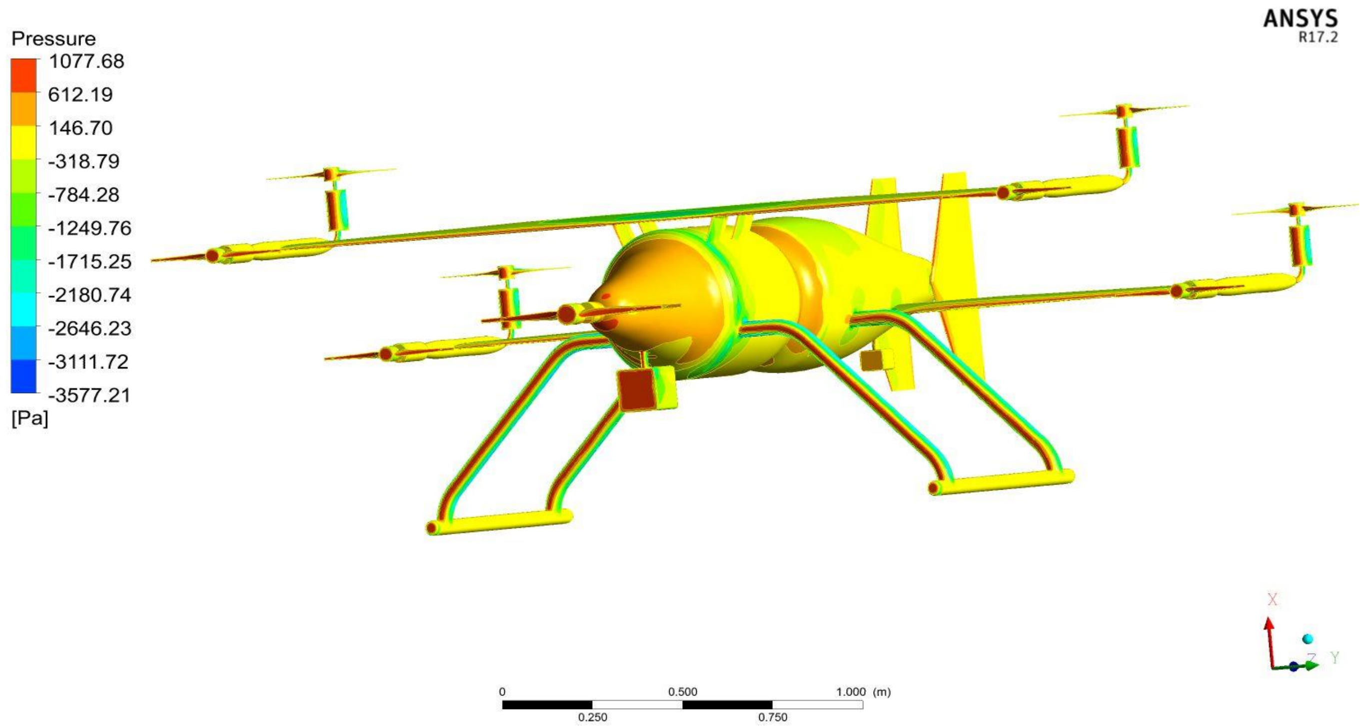

Figure 22. Pressure variation on the UAV at steady state- Super cruise with payload 41.67 m/s.

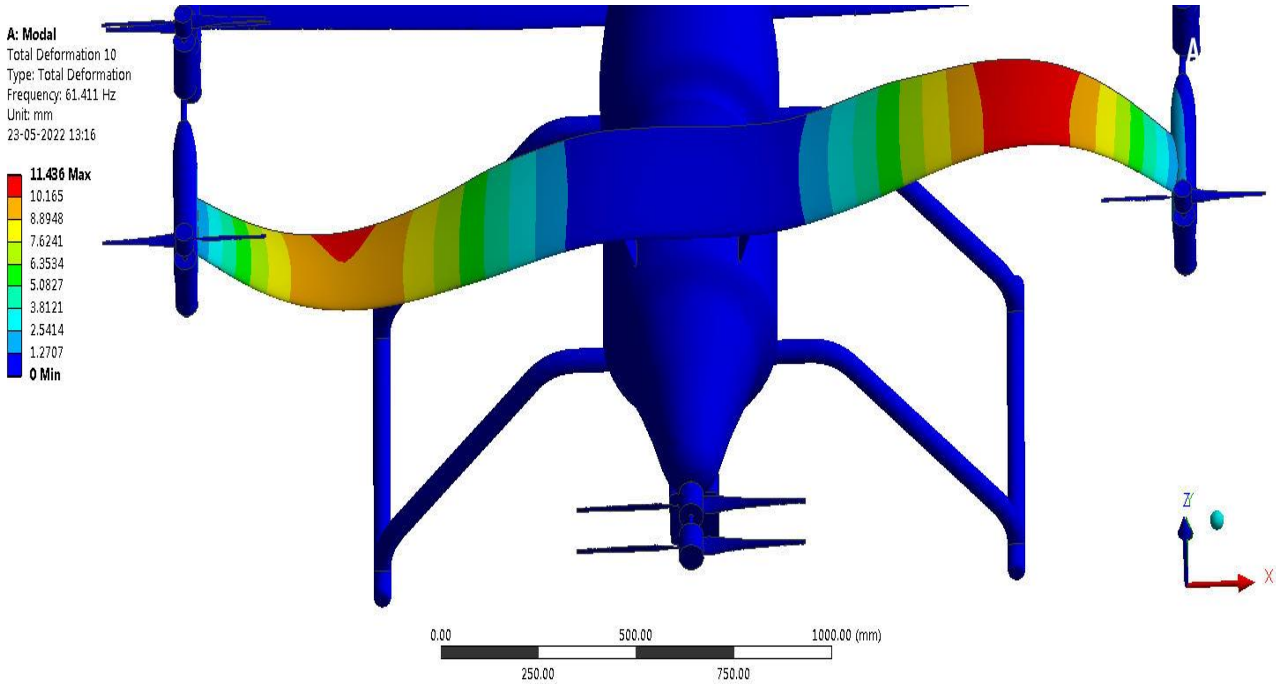

Figure 23. Vibrated structure of front wing—Aluminum alloy.

Figure 24. Vibrated structure of rear wing—Aluminum alloy.

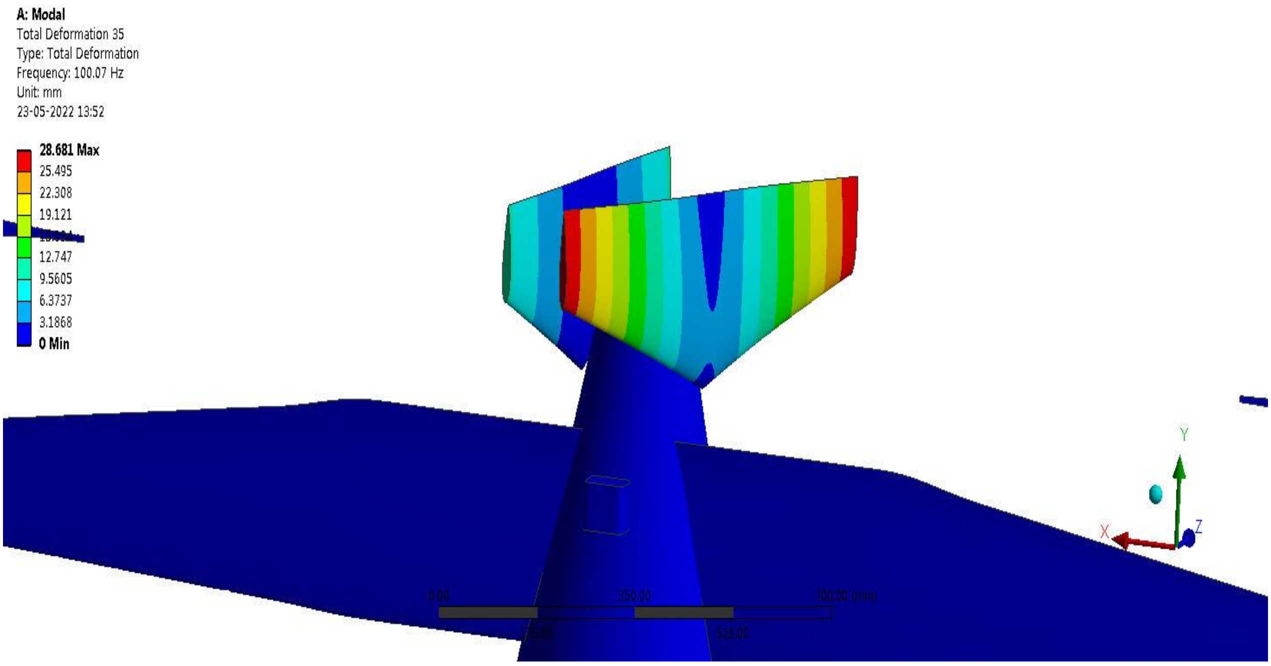

Figure 25. Vibrated structure of vertical stabilizer—Aluminum alloy.

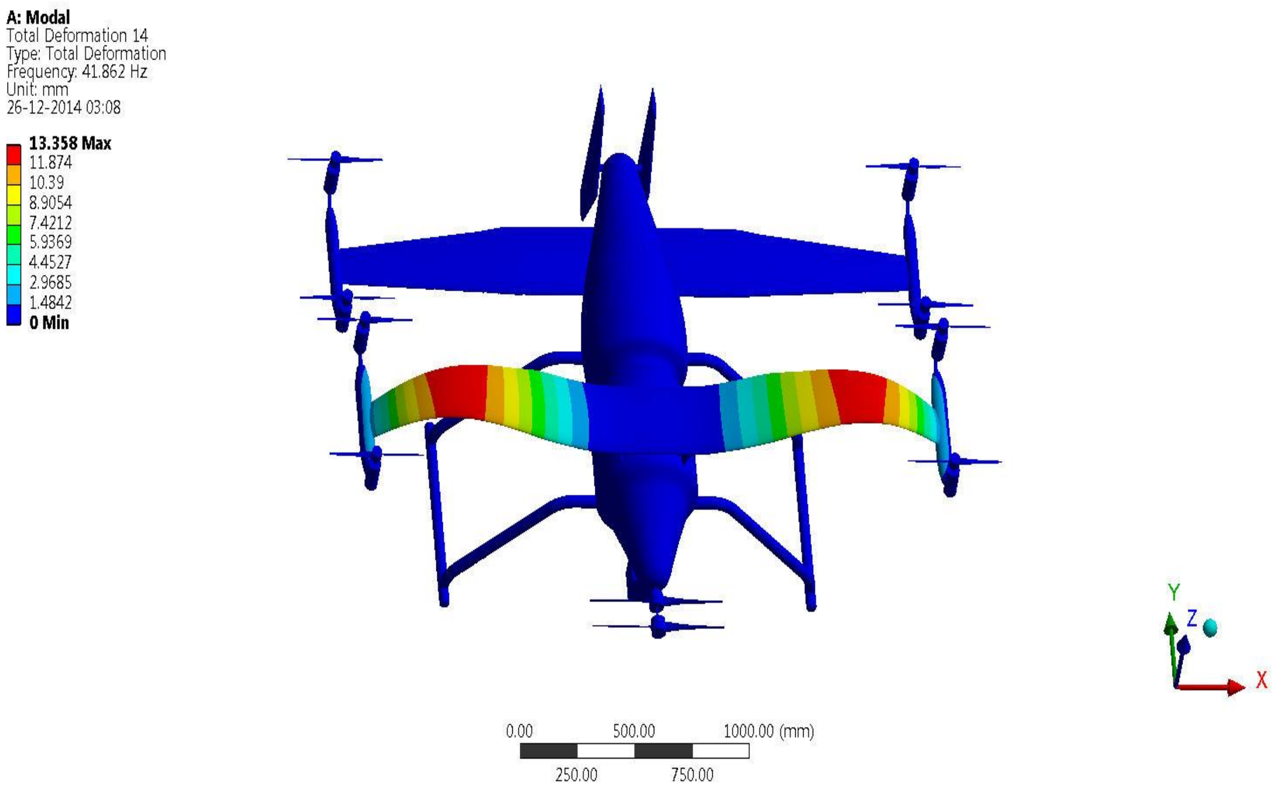

Figure 26. Vibrated structure of front wing—E-GFRP-Fabric.

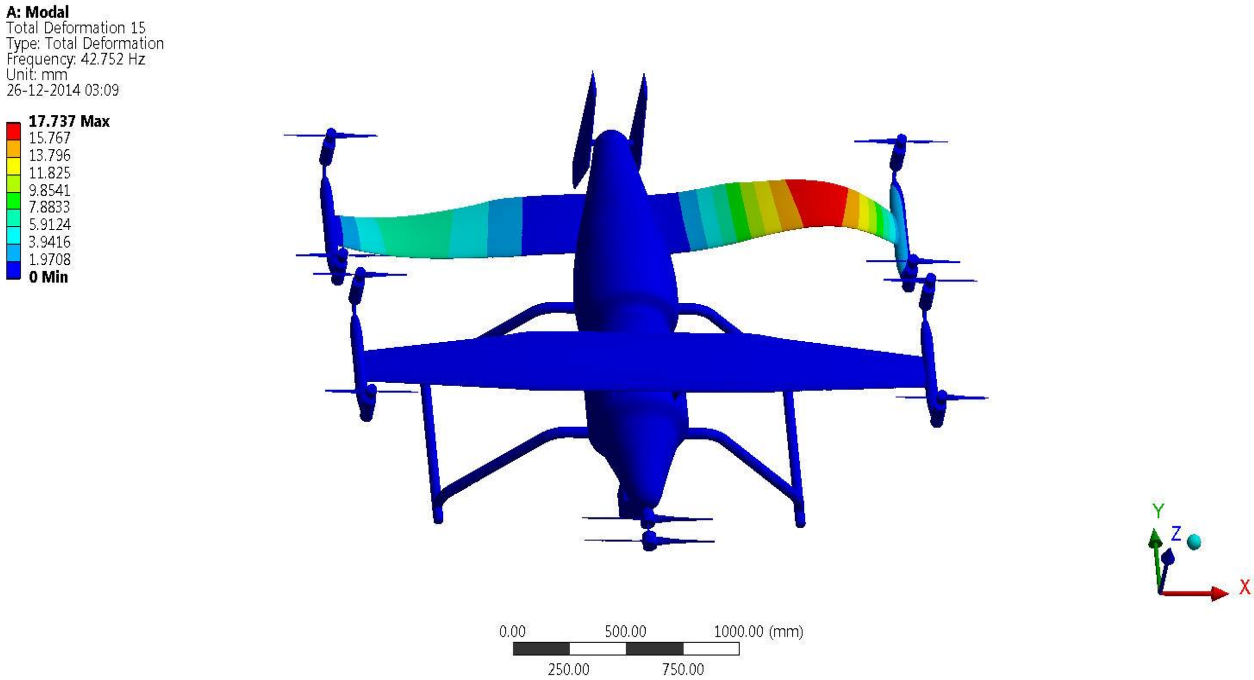

Figure 27. Vibrated structure of rear wing—E-GFRP-Fabric.

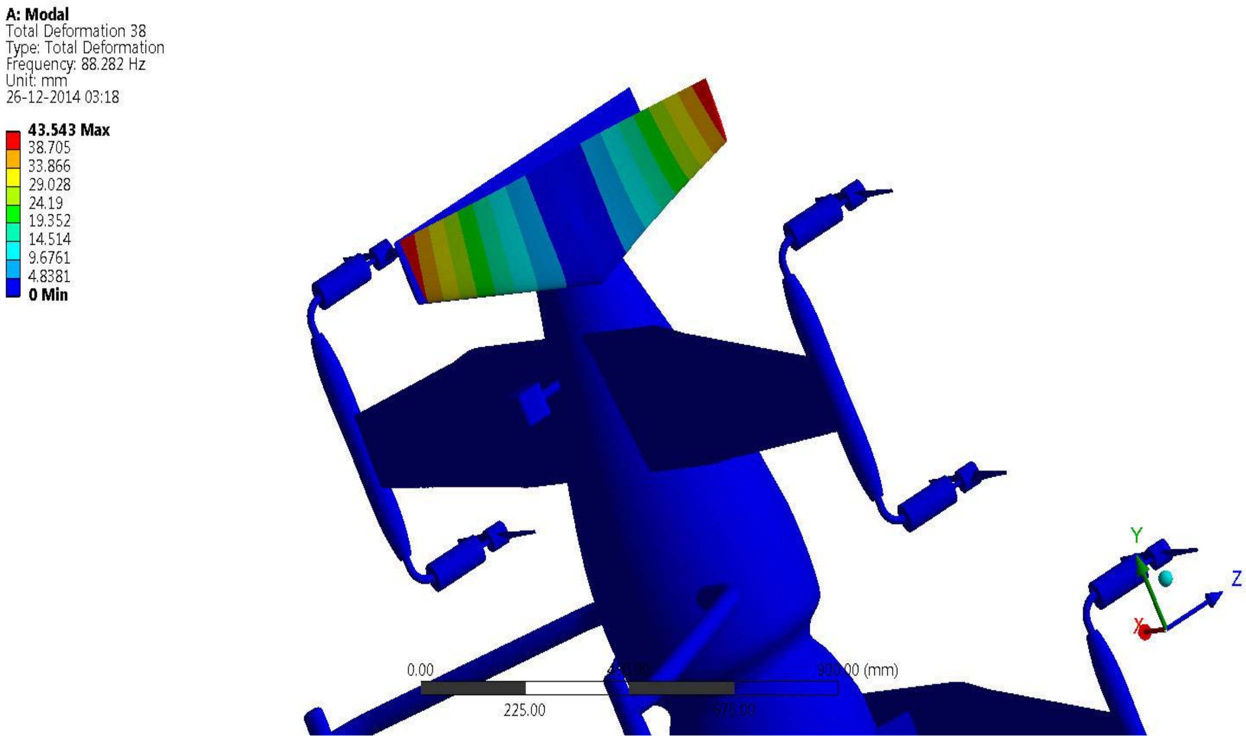

Figure 28. Vibrated structure of vertical stabilizer—E-GFRP-Fabric.

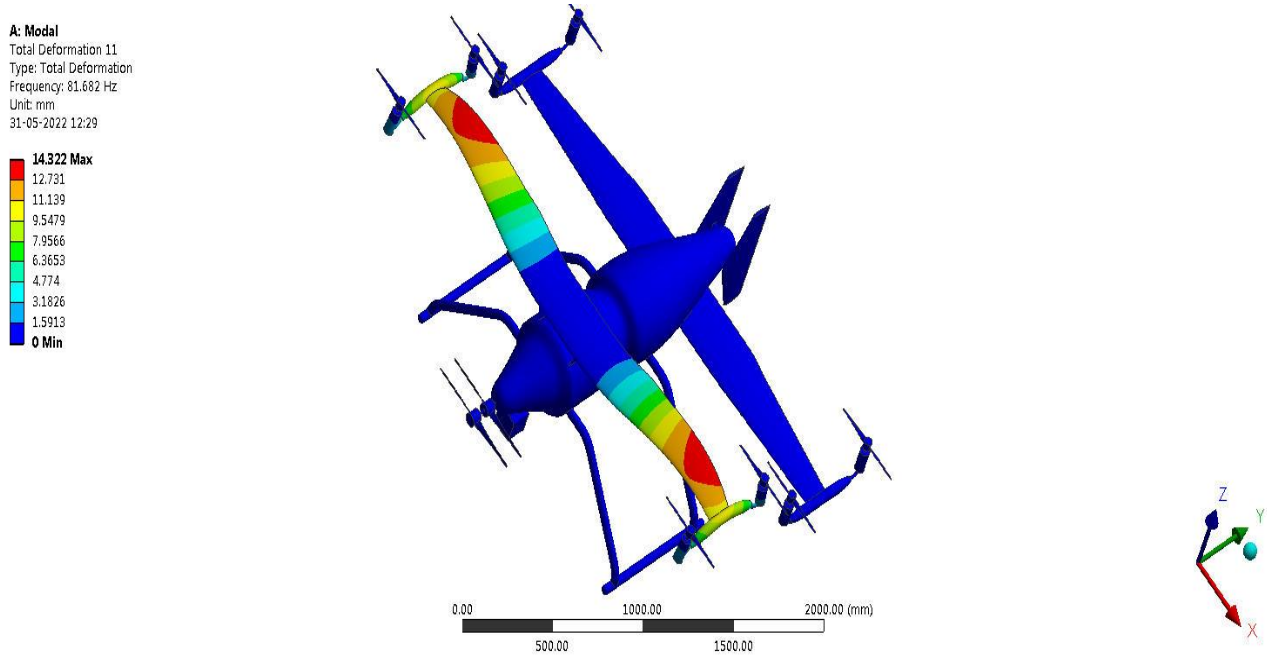

Figure 29. Vibrated structure of front wing—CFRP-UD-Wet.

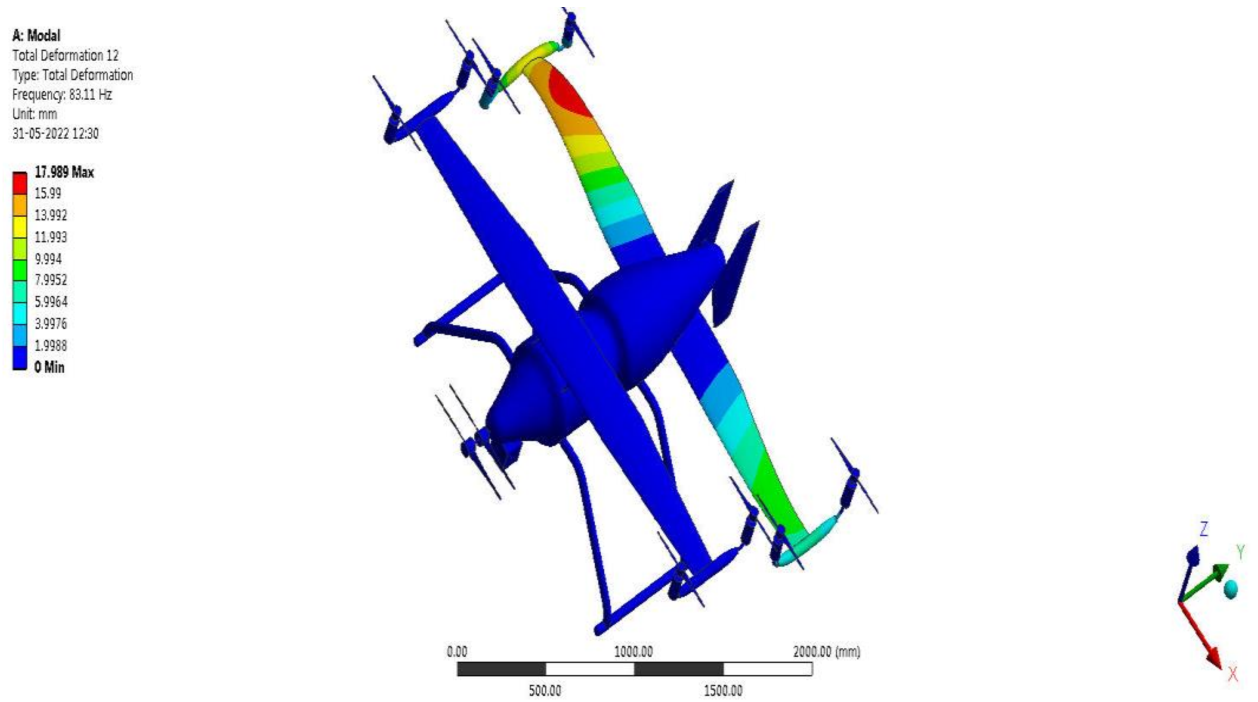

Figure 30. Vibrated structure of rear wing—CFRP-UD-Wet.

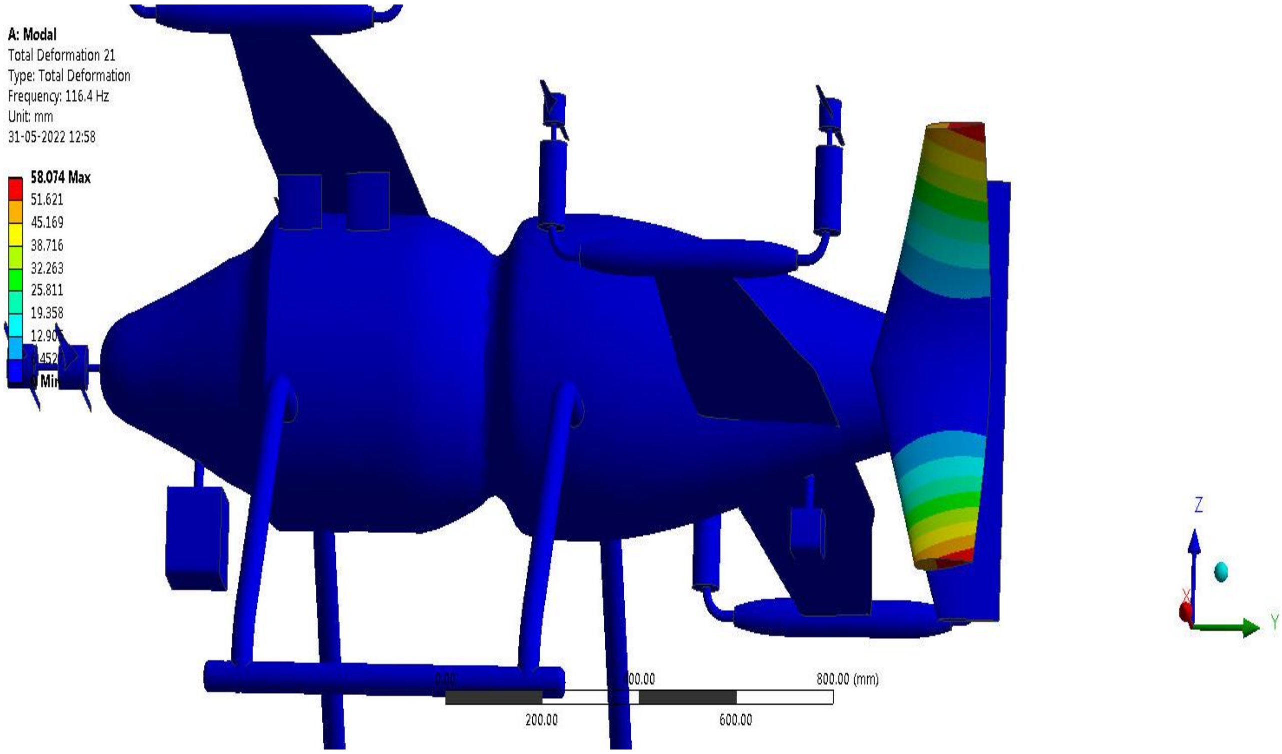

Figure 31. Vibrated structure of vertical stabilizer—CFRP-UD-Wet.

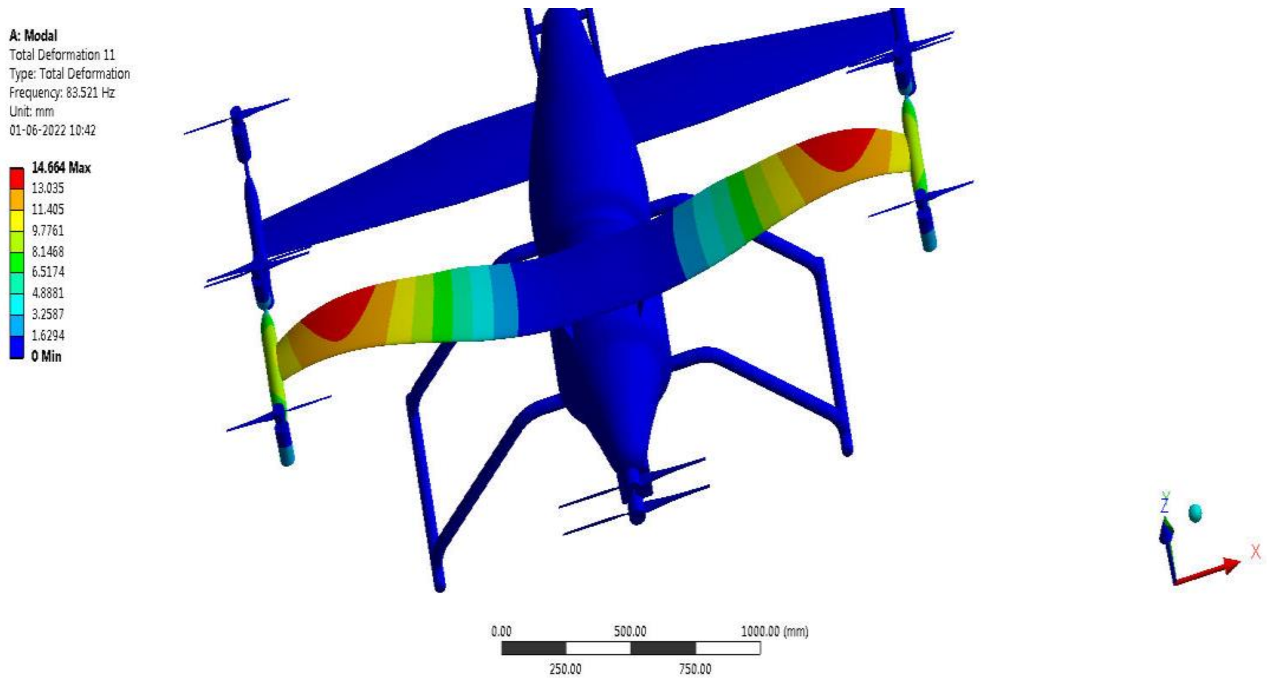

Figure 32. Vibrated structure of front wing—CFRP-UD-Prepreg.

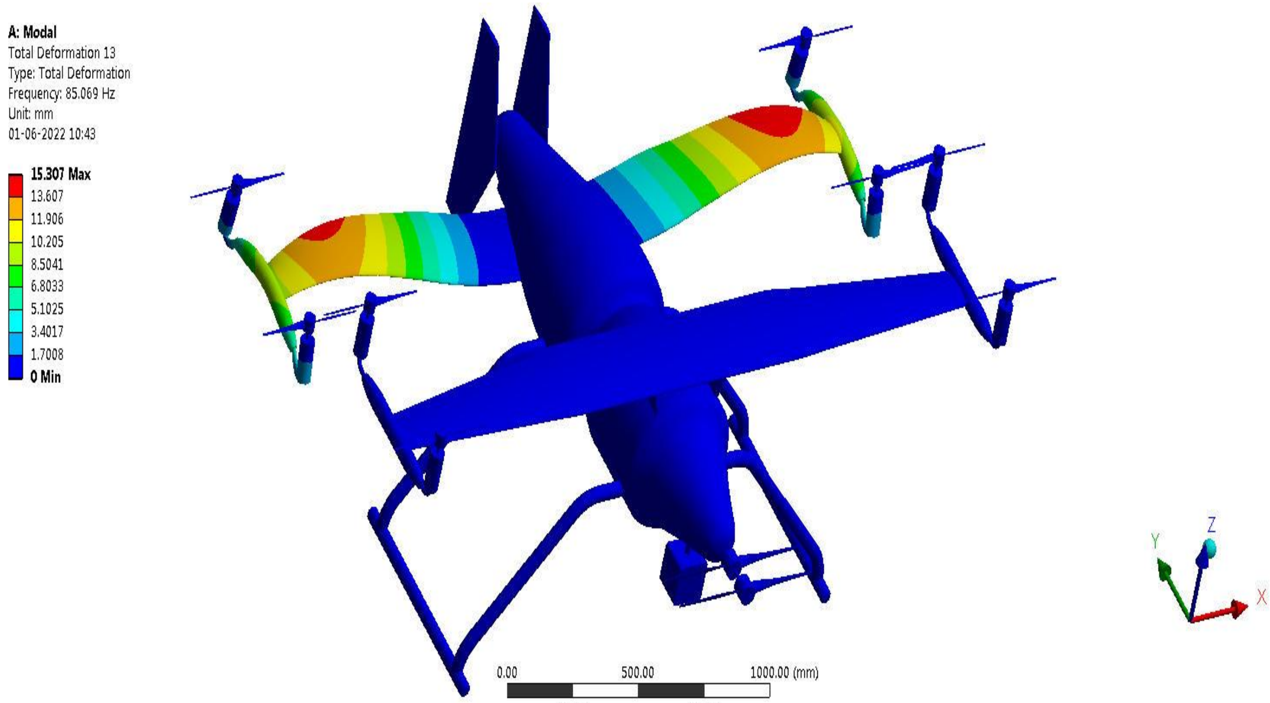

Figure 33. Vibrated structure of rear wing—CFRP-UD-Prepreg.

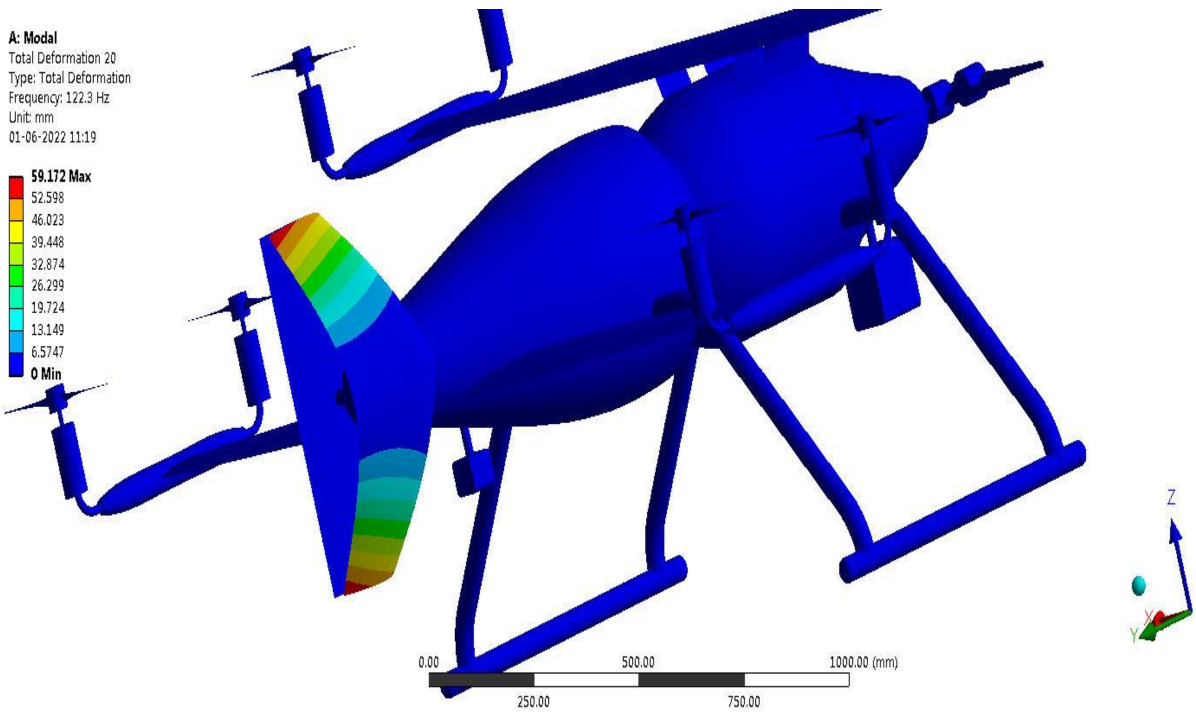

Figure 34. Vibrated structure of vertical stabilizer—CFRP-UD-Prepreg.

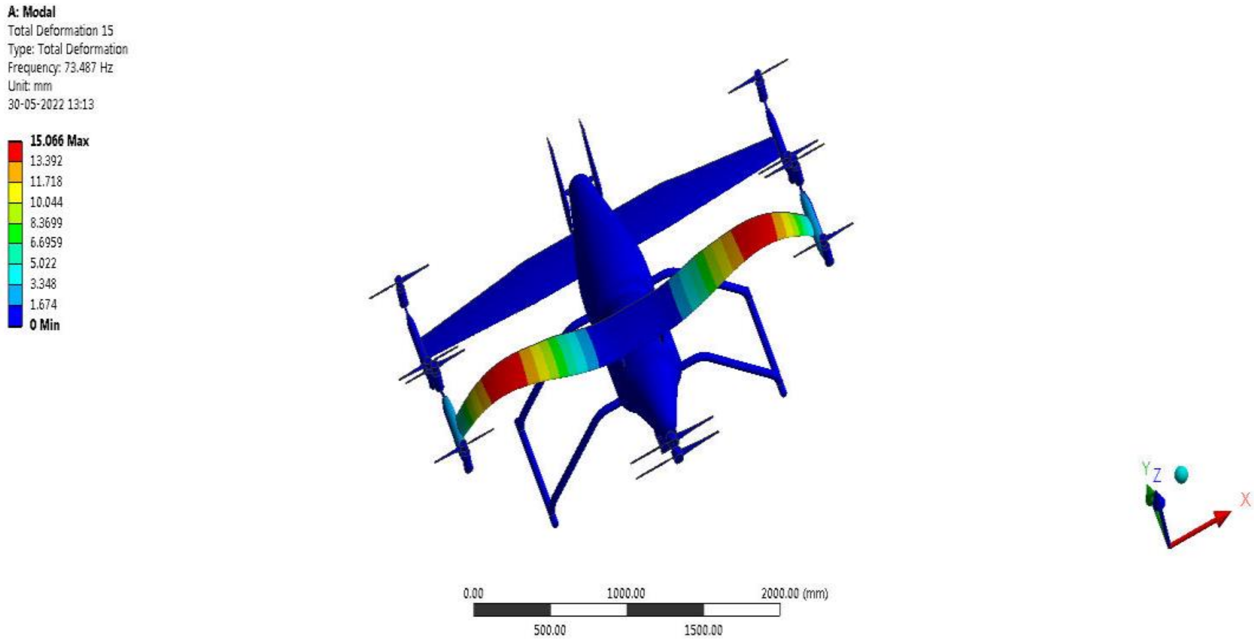

Figure 35. Vibrated structure of front wing—CFRP-Woven-Prepreg.

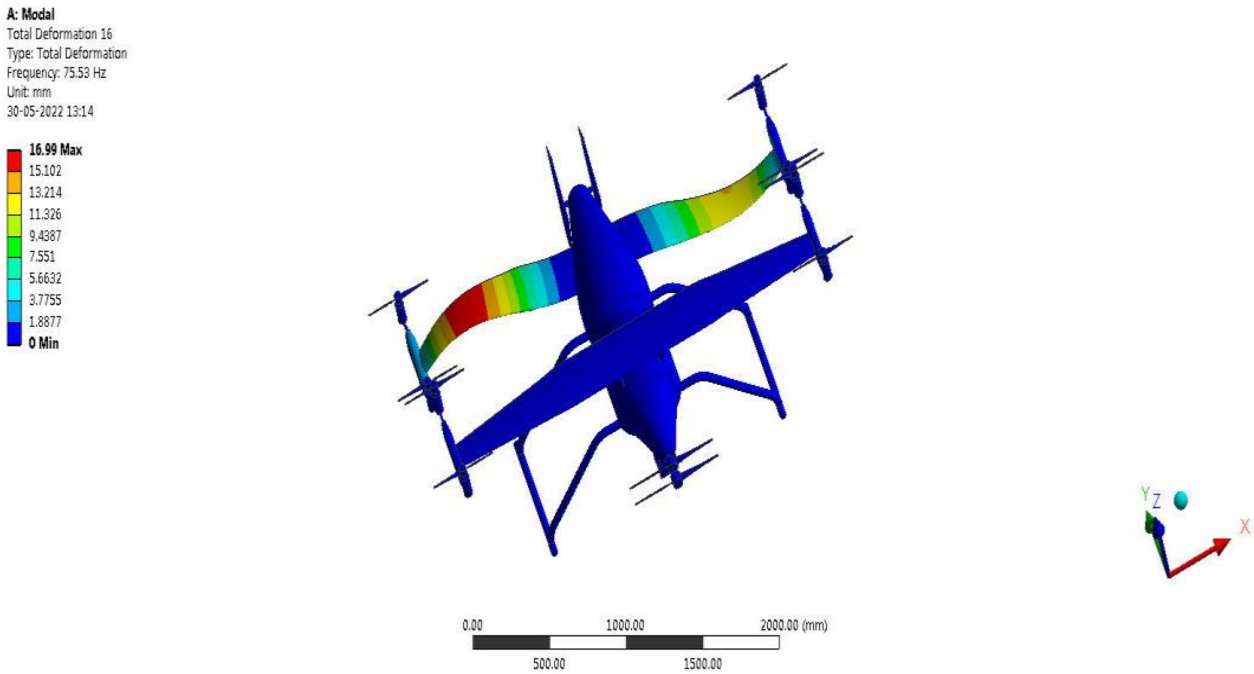

Figure 36. Vibrated structure of rear wing—CFRP-Woven-Prepreg.

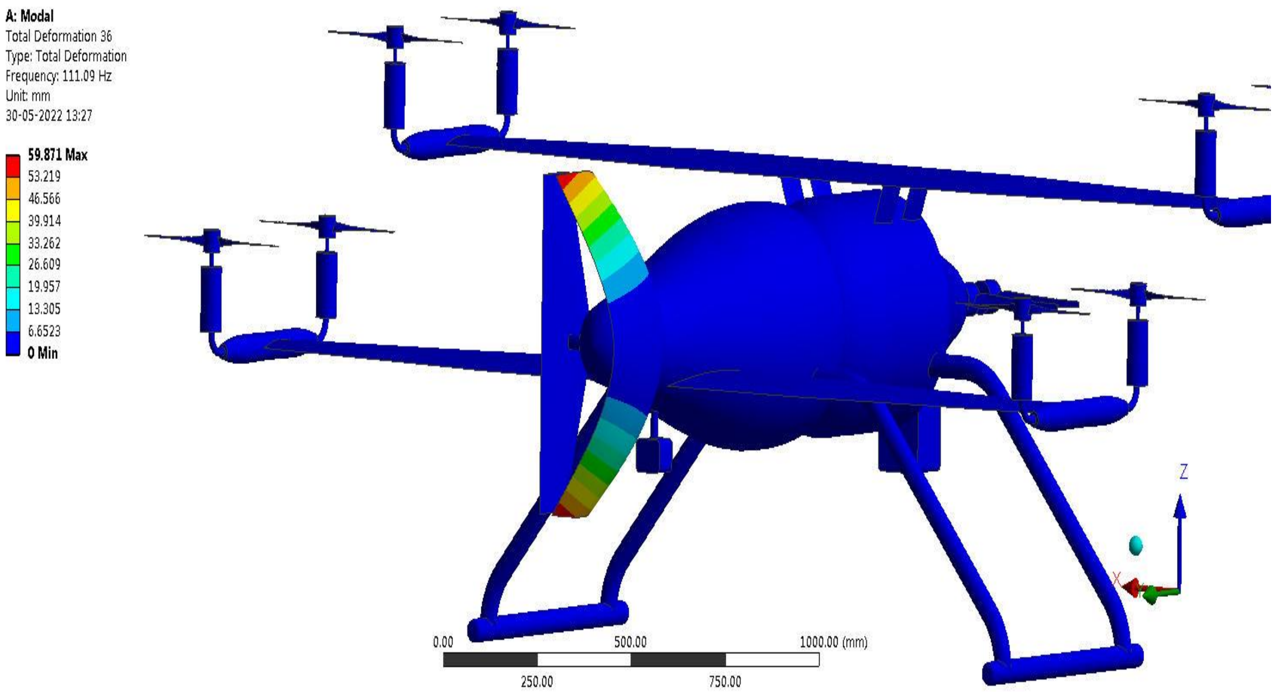

Figure 37. Vibrated structure of vertical stabilizer—CFRP-Woven-Prepreg.

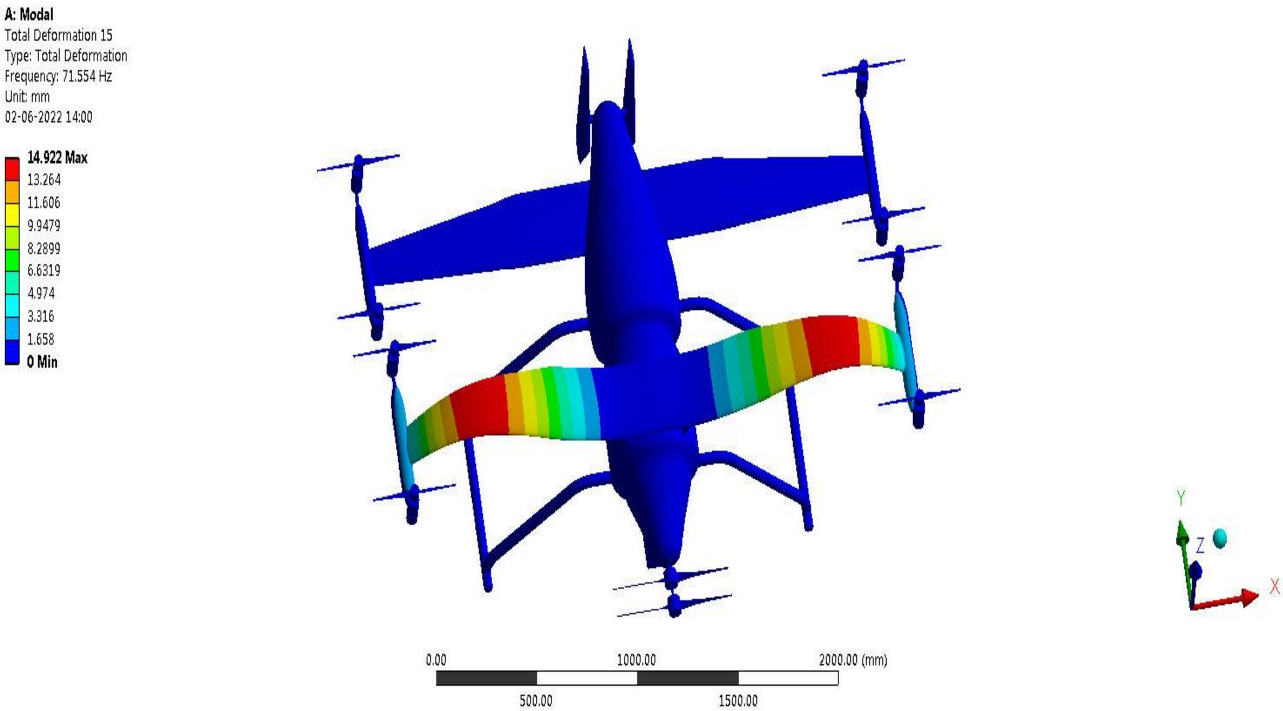

Figure 38. Vibrated structure of front wing—CFRP-Woven-Wet.

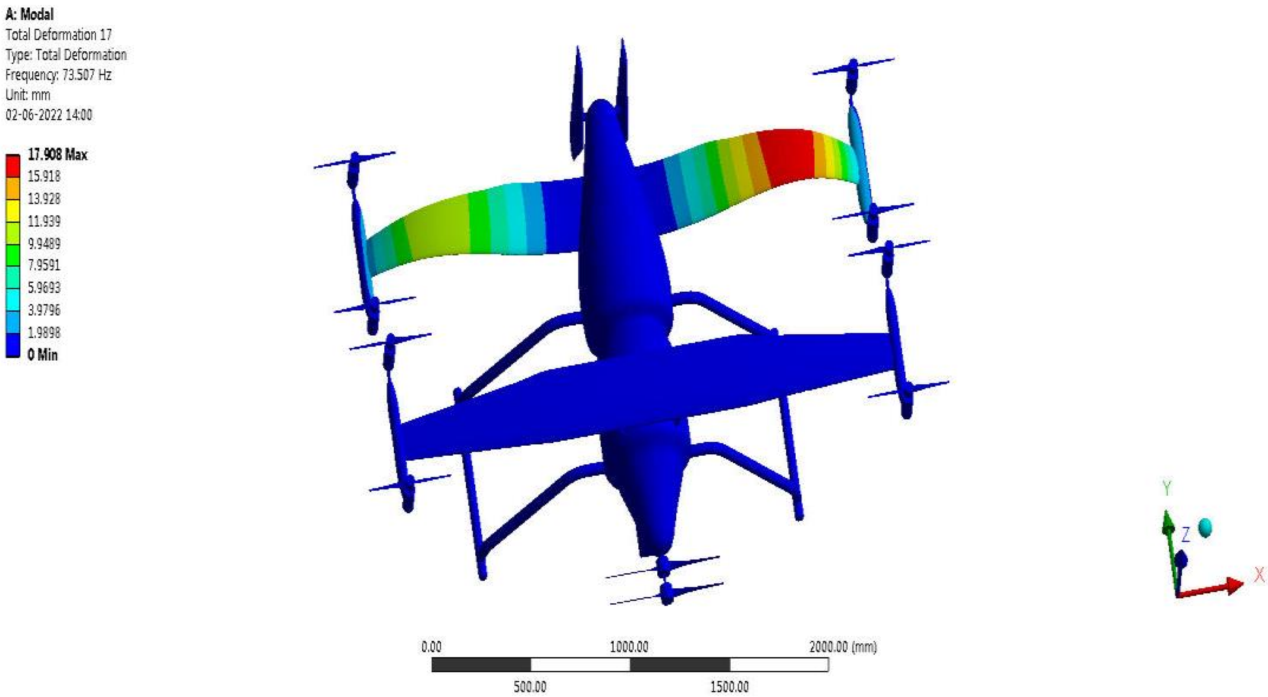

Figure 39. Vibrated structure of rear wing—CFRP-Woven-Wet.

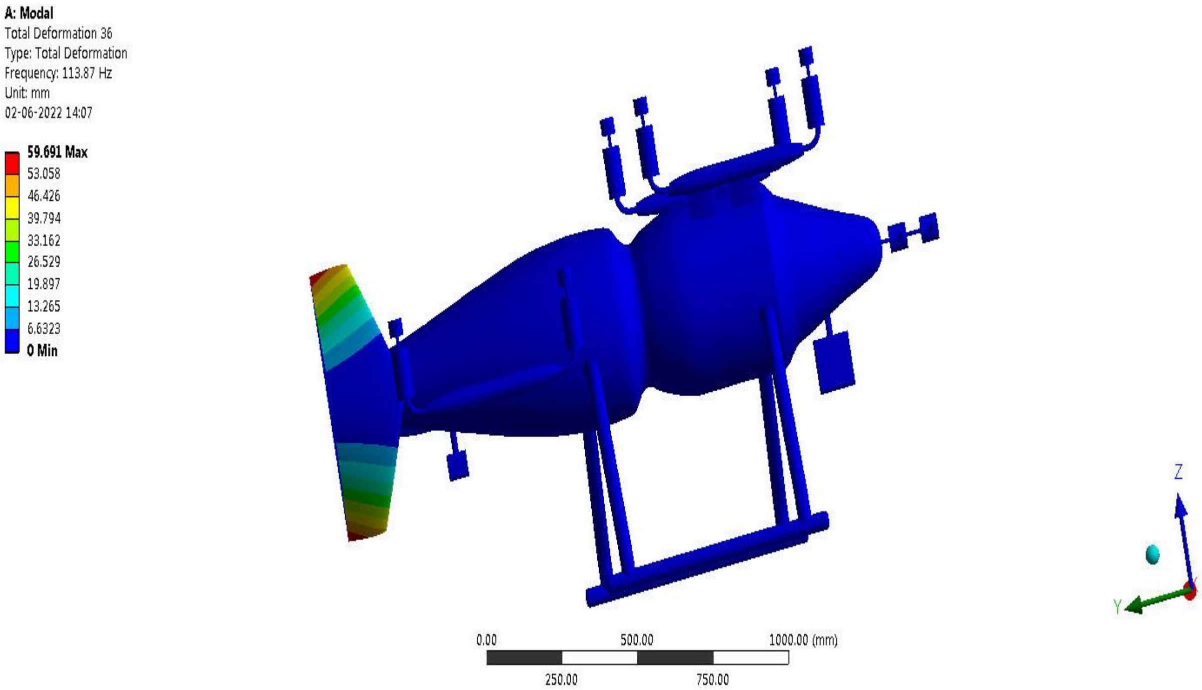

Figure 40. Vibrated structure of vertical stabilizer—CFRP-Woven-Wet.

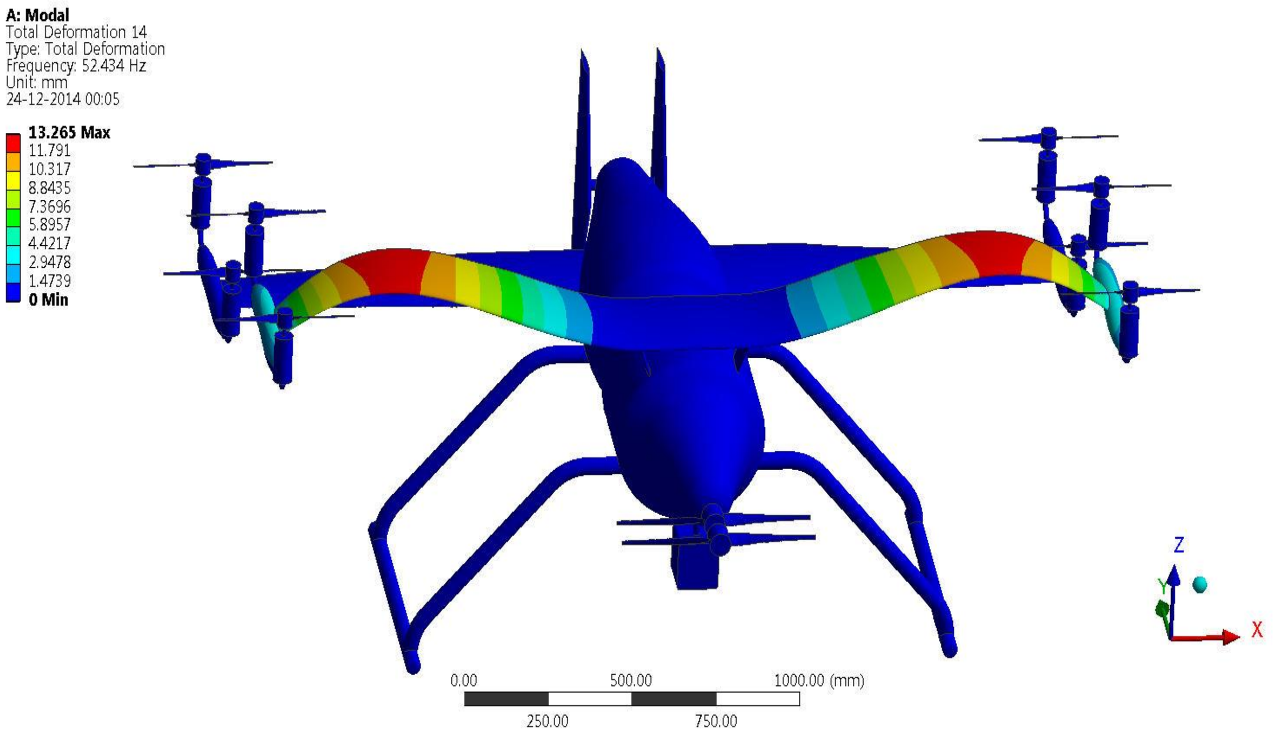

Figure 41. Vibrated structure of front wing—E-GFRP-UD.

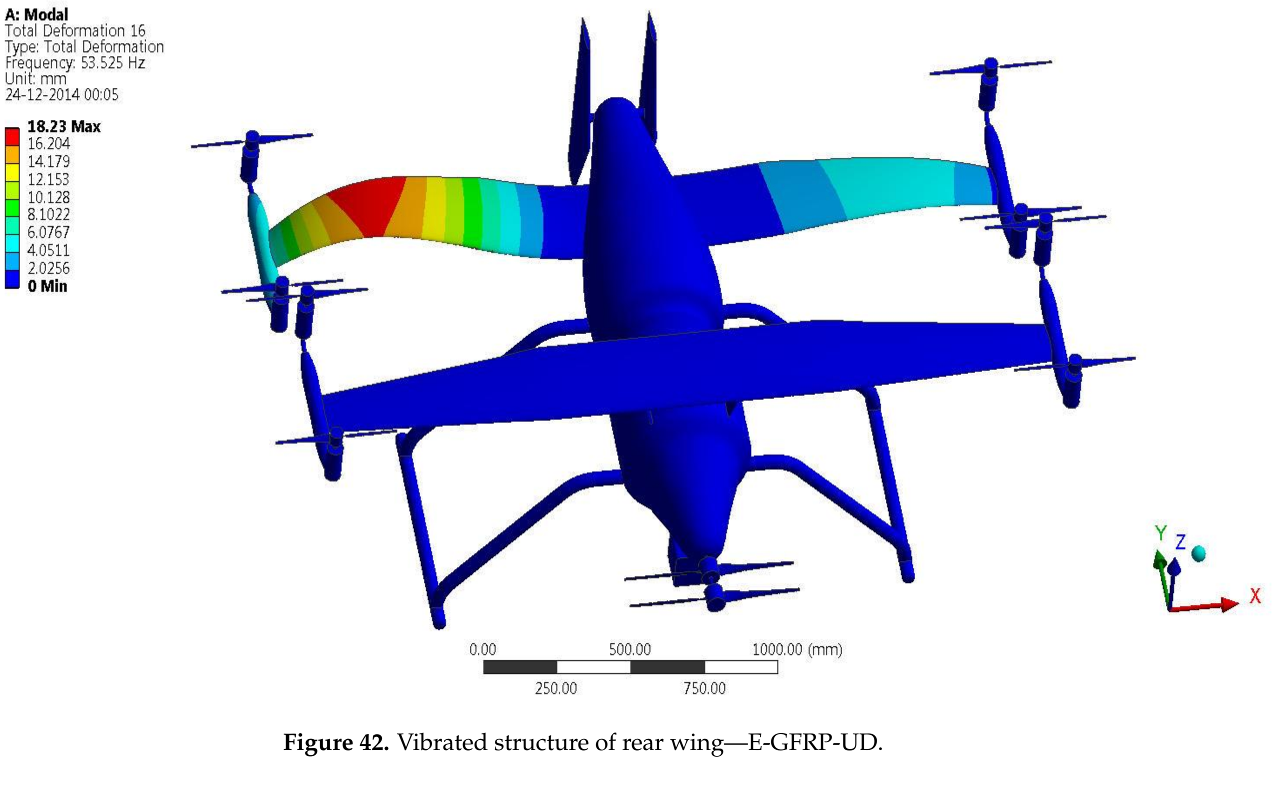

Figure 42. Vibrated structure of rear wing—E-GFRP-UD.

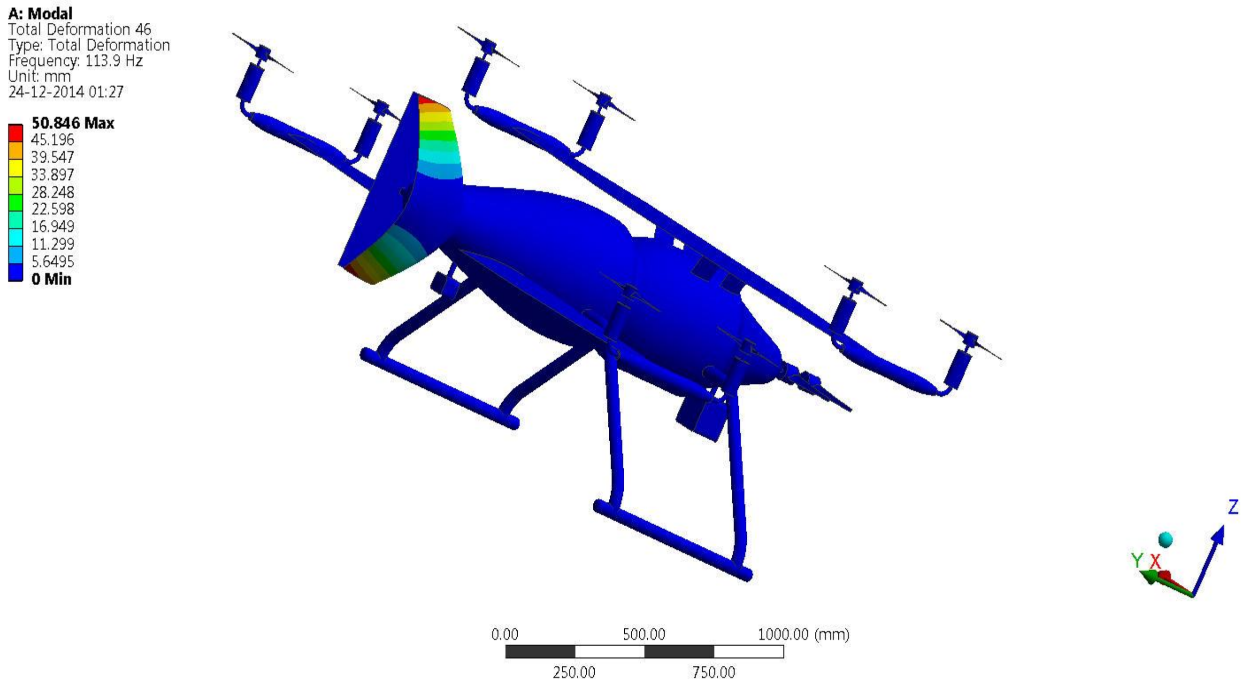

Figure 43. Vibrated structure of vertical stabilizer—E-GFRP-UD.

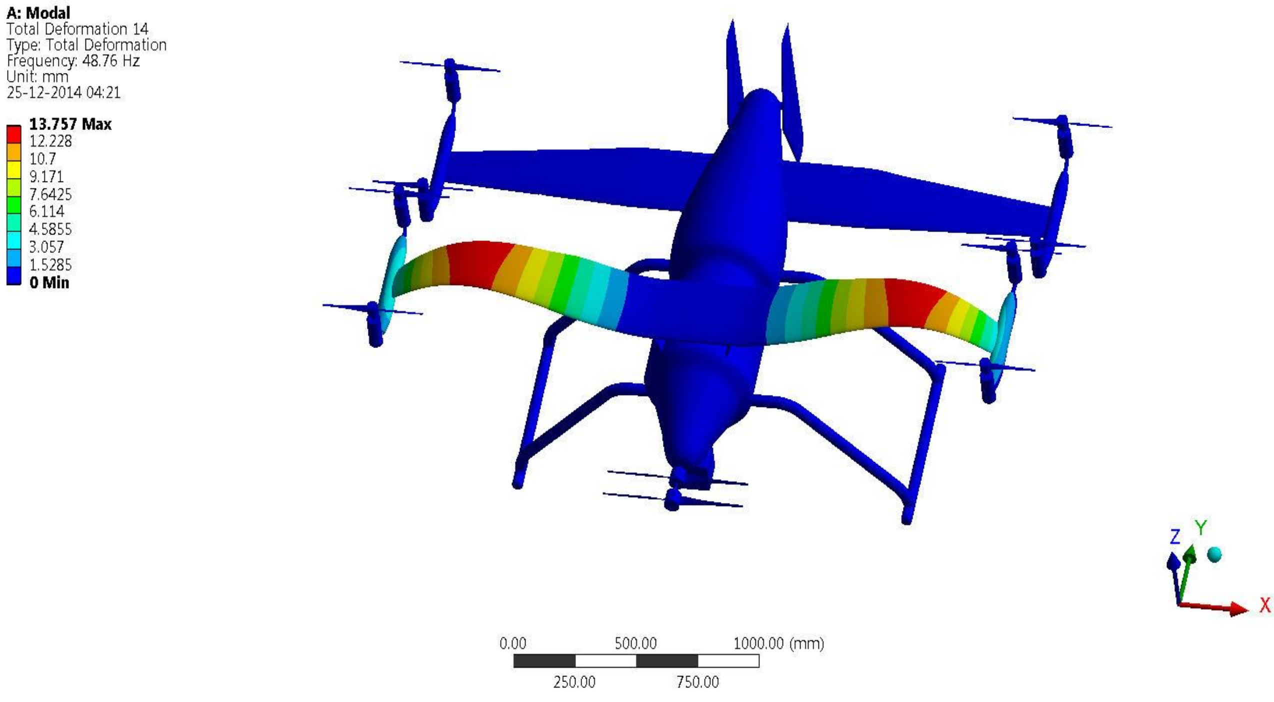

Figure 44. Vibrated structure of front wing—E-GFRP-Wet.

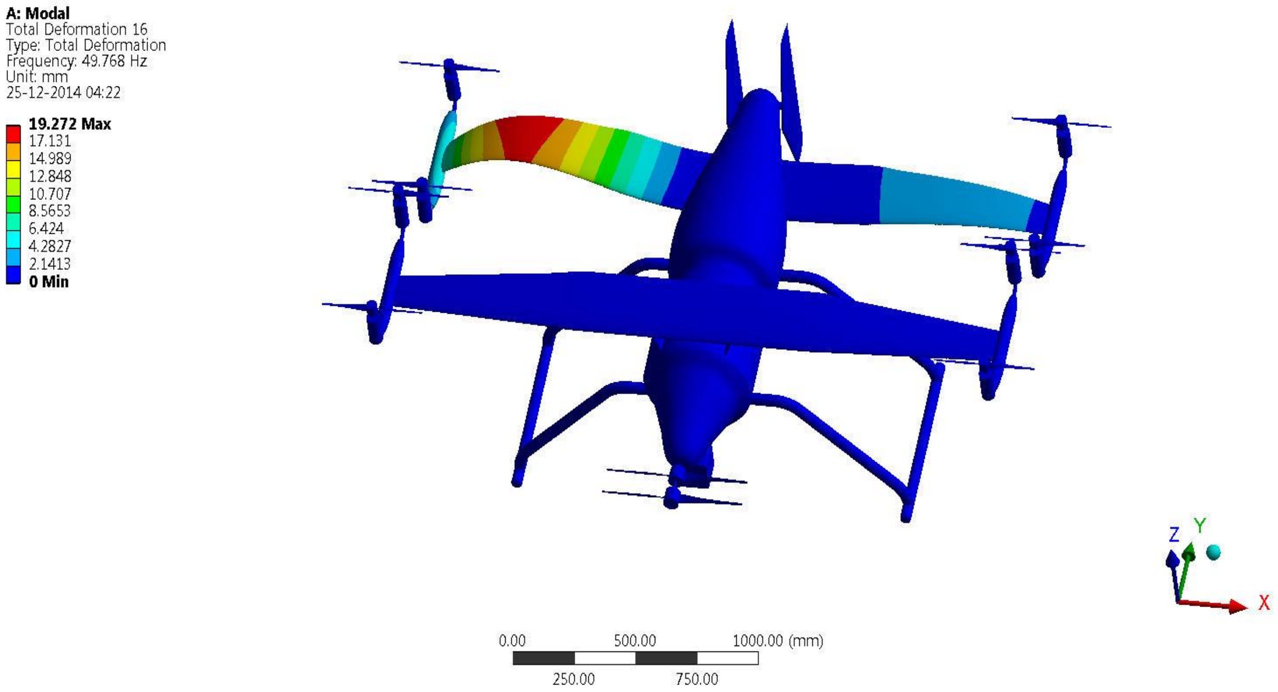

Figure 45. Vibrated structure of rear wing—E-GFRP-Wet.

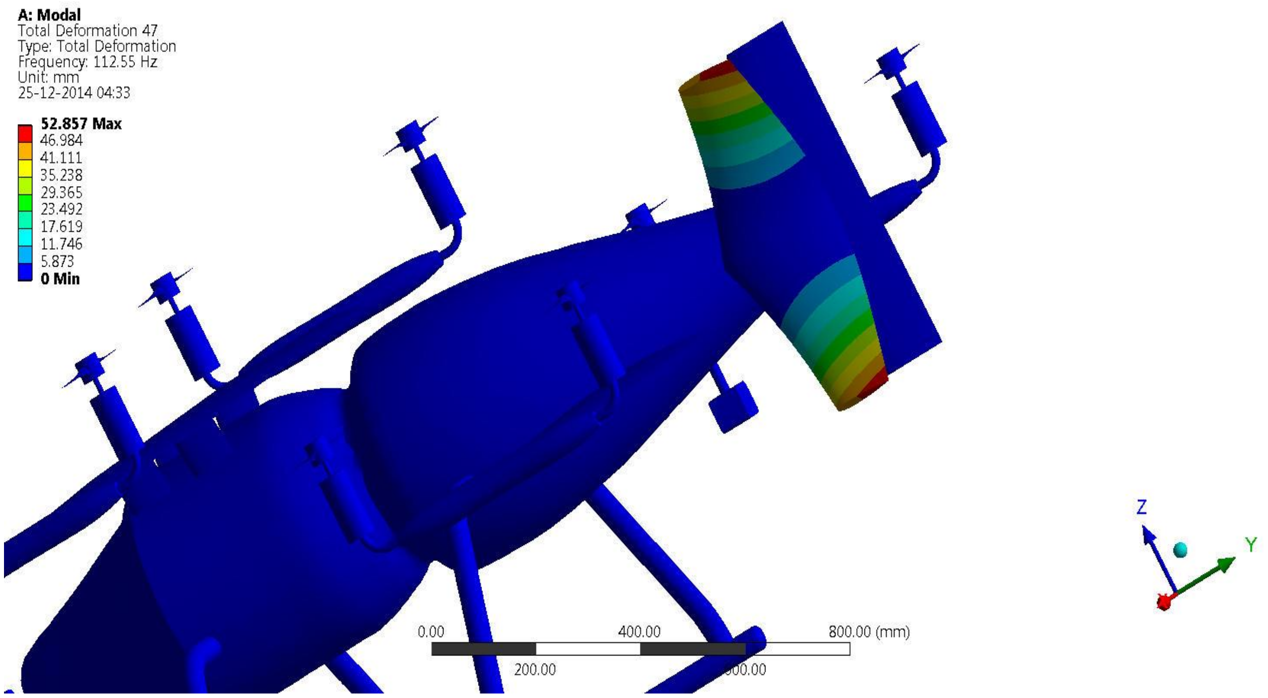

Figure 46. Vibrated structure of vertical stabilizer—E-GFRP-Wet.

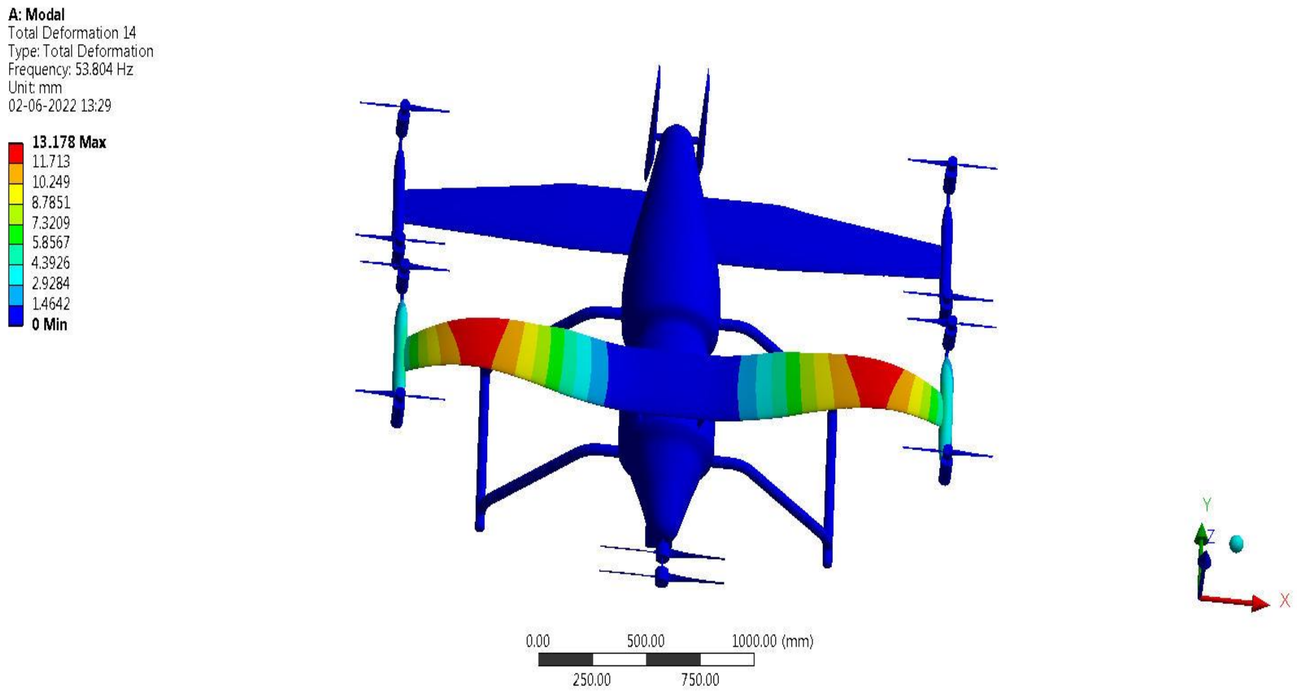

Figure 47. Vibrated structure of front wing—S-GFRP-UD.

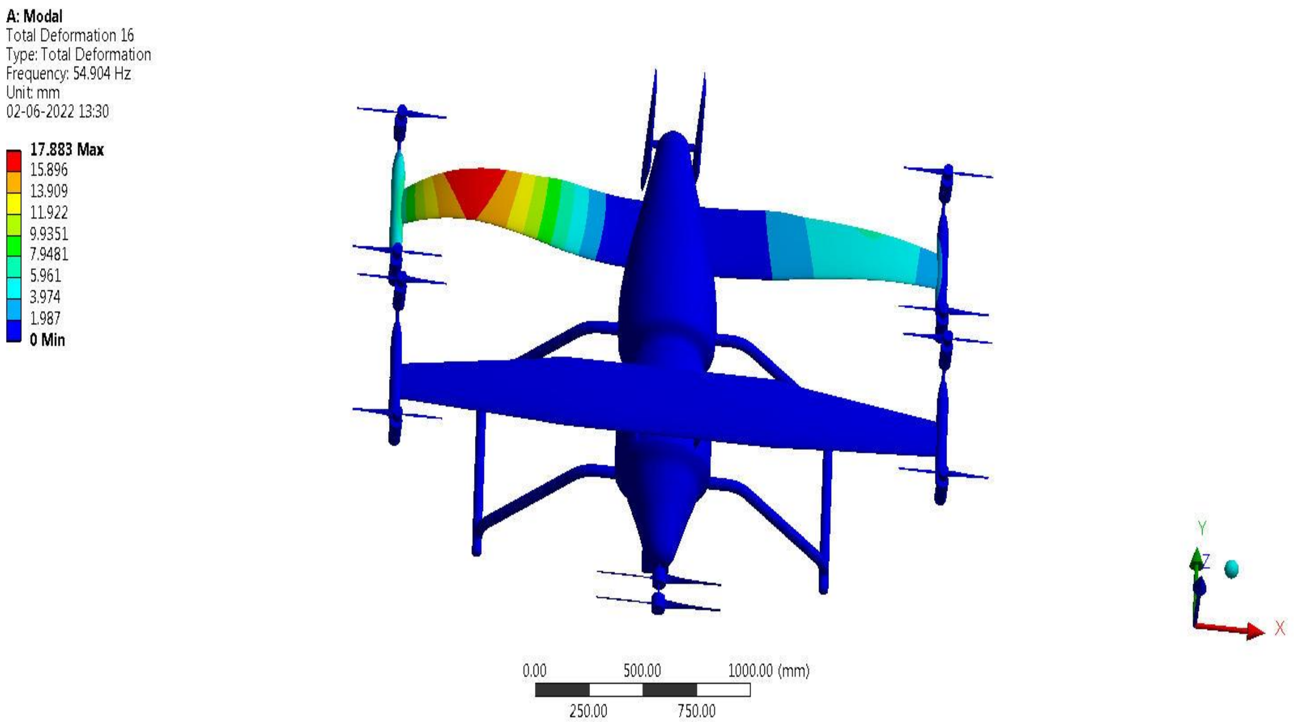

Figure 48. Vibrated structure of rear wing—S-GFRP-UD.

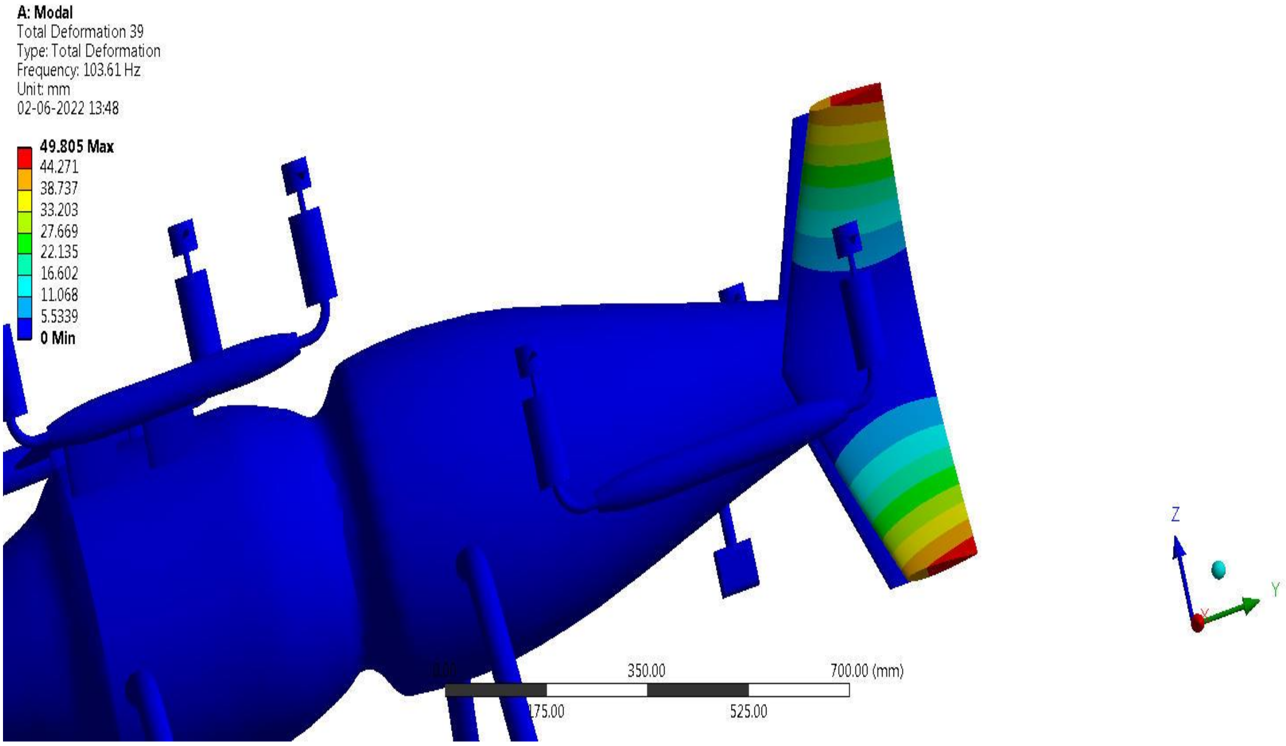

Figure 49. Vibrated structure of vertical stabilizer—S-GFRP-UD.

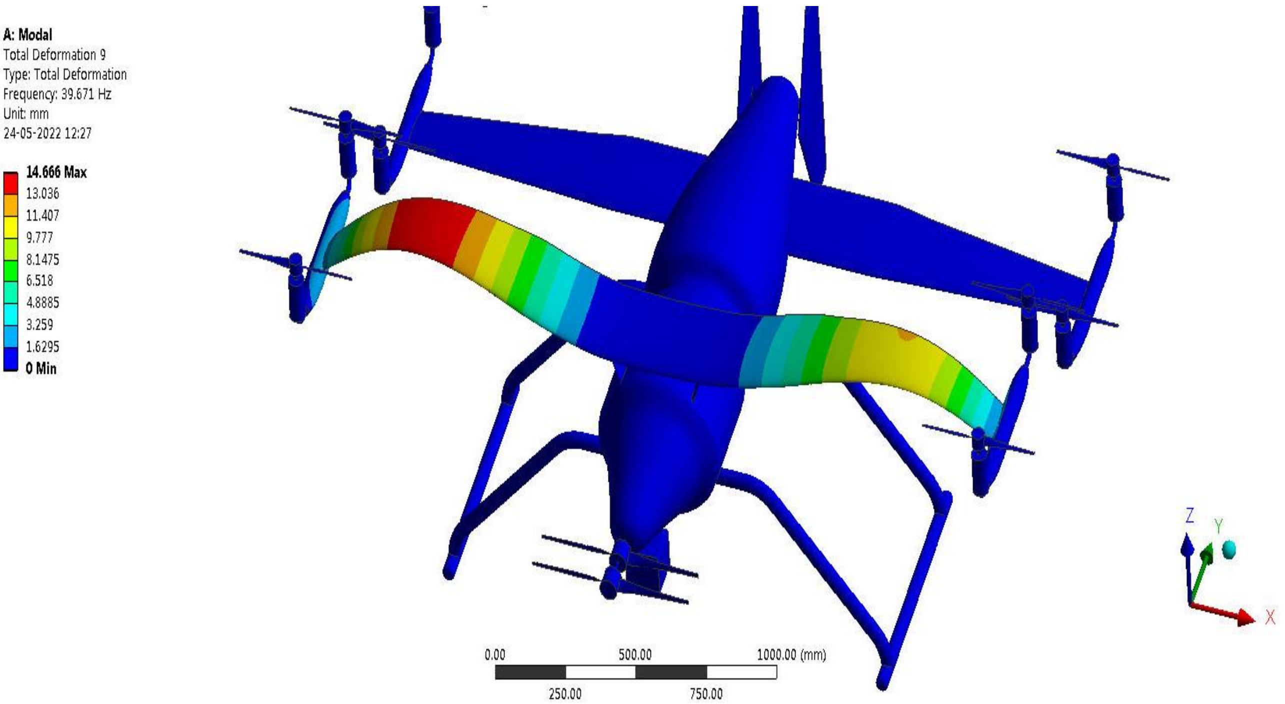

Figure 50. Vibrated structure of front wing—FR-4-GFRP-Woven.

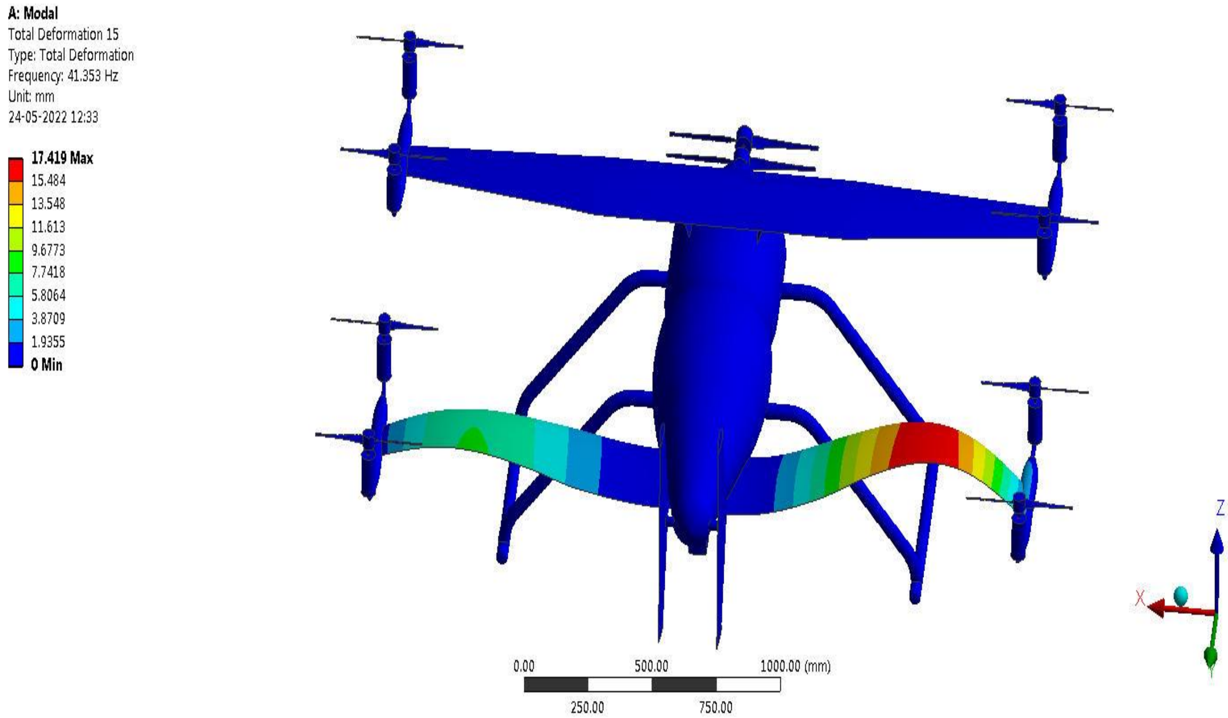

Figure 51. Vibrated structure of rear wing—FR-4-GFRP-Woven.

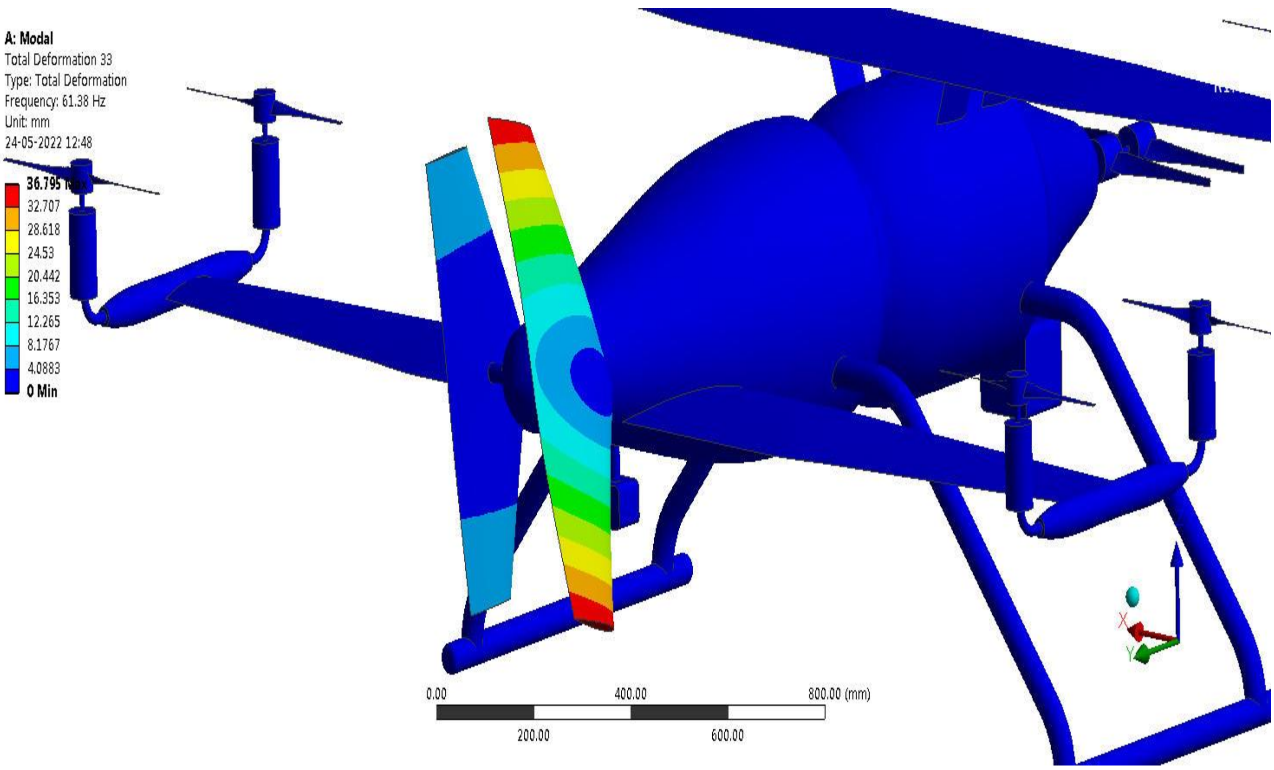

Figure 52. Vibrated structure of vertical stabilizer—FR-4-GFRP-Woven.

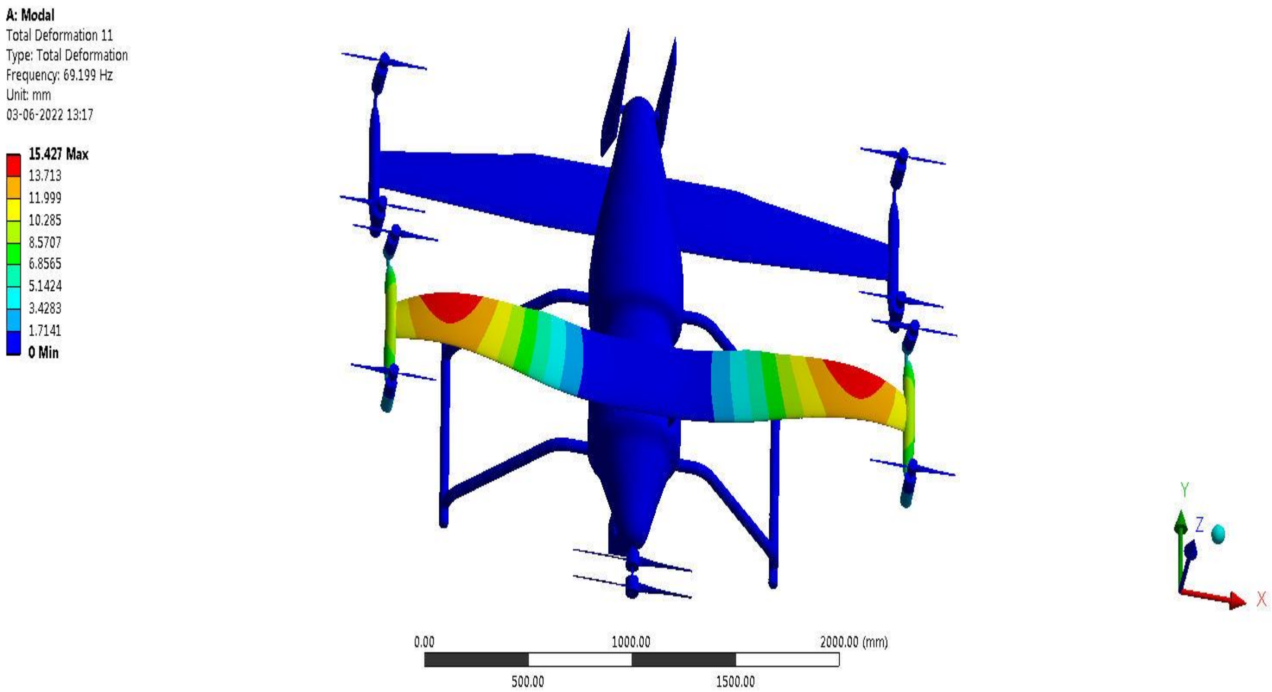

Figure 53. Vibrated structure of front wing—KFRP-UD-49.

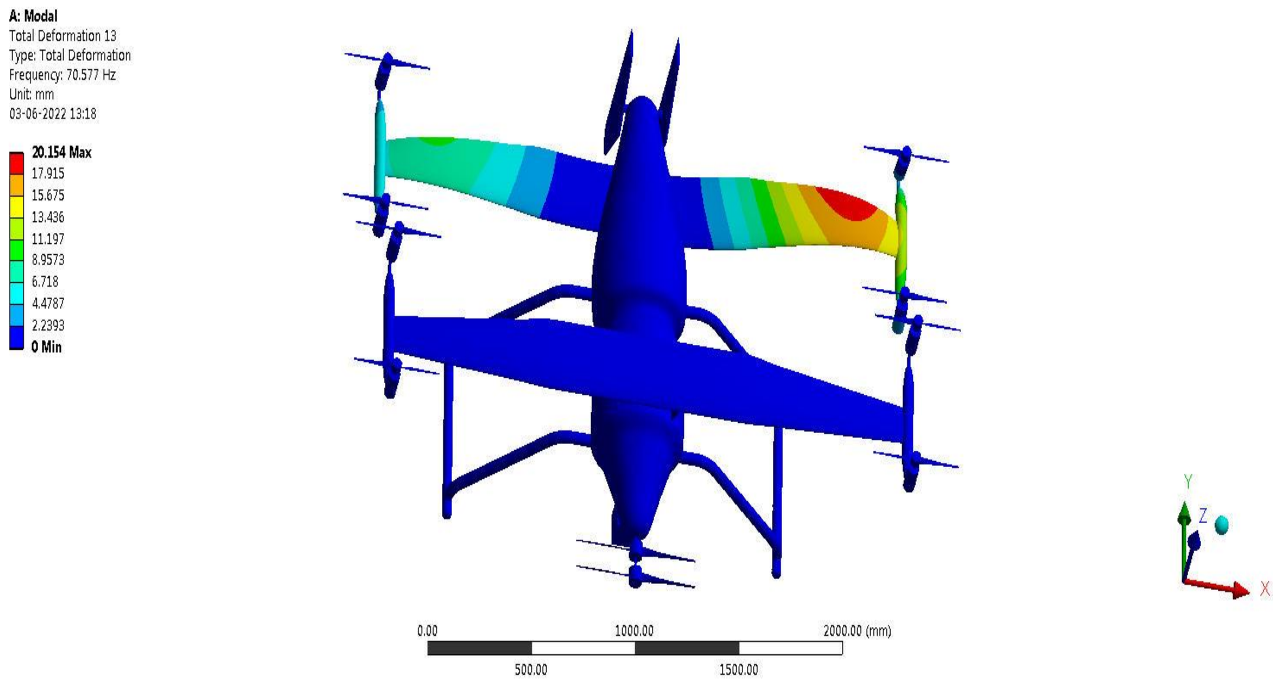

Figure 54. Vibrated structure of rear wing—KFRP-UD-49.

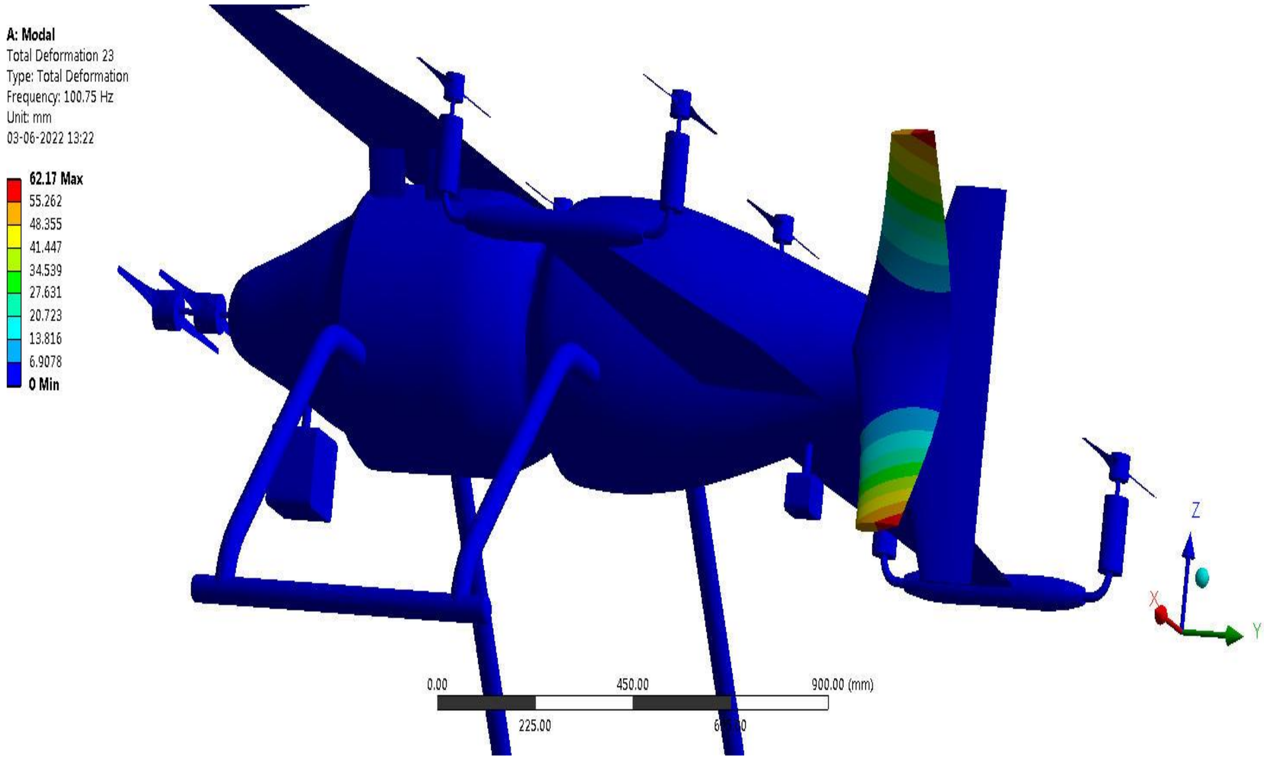

Figure 55. Vibrated structure of vertical stabilizer—KFRP-UD-49.

Table 7. The comprehensive acceptable outcome of free vibrational computation—natural frequencies (Hz).

Lightweight Materials	Acceptable Outcome of Free Vibrational Computation (Hz)		
	Front Wing	**Rear Wing**	**Vertical Stabilizer**
Aluminium Alloy	61.411	63.845	100.07
E-GFRP-Fabric	41.862	42.755	88.282
CFRP-UD-Wet	81.682	83.11	116.4
CFRP-UD-Prepreg	83.521	85.069	122.3
CFRP-Woven-Prepreg	73.487	75.53	111.09
CFRP- Woven-Wet	71.554	73.507	113.87
E-GFRP-UD	52.434	53.525	113.9
E-GFRP-Wet	48.76	49.768	112.55
S-GFRP-UD	53.804	54.904	103.61
FR-4-GFRP-Woven	39.671	41.353	61.38
KFRP-UD-49	69.199	70.577	100.75

Table 8. The comprehensive acceptable outcome of free vibrational computation—vibrational displacement (mm).

Lightweight Materials	Acceptable Outcome of Free Vibrational Computation (mm)		
	Front Wing	Rear Wing	Vertical Stabilizer
Aluminium Alloy	11.436	15.244	28.681
E-GFRP-Fabric	13.358	17.751	43.543
CFRP-UD-Wet	14.322	17.989	58.074
CFRP-UD-Prepreg	14.664	15.307	59.172
CFRP-Woven-Prepreg	15.066	16.99	59.871
CFRP- Woven-Wet	14.922	17.908	59.691
E-GFRP-UD	13.265	18.23	50.846
E-GFRP-Wet	13.757	19.272	52.857
S-GFRP-UD	13.178	17.883	49.805
FR-4-GFRP-Woven	14.666	17.419	36.795
KFRP-UD-49	15.427	20.154	62.17

3.3. Estimation of Power from Energy Harvester

The selection and calculation of PVEH patch both play important roles in this estimation. Various conventional and composites materials were selected and analyzed in ANSYS. The power is calculated with respect to different materials and the calculations are carried out following two steps: intermediate power estimation step and final power estimation step. The first intermediate power extraction step and its mathematical representation are imposed from Equation (21).

$$P^{\mathrm{Hybrid\ UAV}}_{\mathrm{Intermediate}} = d^2_{\mathrm{lwm}} w^2 f^2 \times \frac{18 \times T_{\mathrm{PL}}}{\left[(W_{\mathrm{L-TW}}) \times (L_{\mathrm{PL}})^2 \times ([t_{\mathrm{TW}}] + [T_{\mathrm{PL}}])^4\right]} \times \frac{\rho_{\mathrm{lwm}}}{[1 + f \times \varepsilon \times (\rho_{\mathrm{lwm}})]} \quad (21)$$

where, "d_{lwm}" is piezoelectric material constant (0.12 for common material); "f" is aerodynamic pressure force acted on the parts of UAV (Pressure * Surface area = 3.175N); "w" is natural frequency is induced for varies composite materials; "WL-TW" is chord length of the tandem wing, which is 0.213 m (average chord length); "LPL" is length of the piezoelectric layer, which is 0.6335 m; "t_{TW}" is thickness of the tandem wing is 0.0213 m; "TPL" is thickness of the piezoelectric, which is 0.006335 m; "ρ_{lwm}" is density of the various lightweight materials. The second cum final power extraction step and its mathematical representation is used from Equation (22).

$$P^{\mathrm{Hybrid\ UAV}}_{\mathrm{Final}} = \left(P^{\mathrm{Hybrid\ UAV}}_{\mathrm{Intermediate}}\right) \times \left(\frac{(0.44 \times L)^5}{36} - \frac{L(0.44 \times L)^4}{6} + \frac{5L^2(0.44 \times L)^3}{12} - \frac{L^3(0.44 \times L)^2}{2} + \frac{L^4(0.44 \times L)}{4}\right) \quad (22)$$

As per the above-mentioned calculating procedures, the determinations of the power outcome of the PVEH patches are executed. The energy extracted on the wingspan for various relevant aerospace materials are listed in Table 9.

Table 9. The estimated energy outcome on 50% of the front wingspan.

Materials	Energy Extracted (W)	Materials	Energy Extracted (W)
Aluminium Alloy	818.19	CFRP- Woven-Wet	568.10
E-GFRP-Fabric	251.67	E-GFRP-UD	415.15
CFRP-UD-Wet	759.77	E-GFRP-Wet	332.03
CFRP-UD-Prepreg	781.33	S-GFRP-UD	436.78
CFRP-Woven-Prepreg	587.10	FR-4-GFRP-Woven	228.00
KFRP-UD-49	498.09		

The same calculations are followed to determine the power outcome of the PVEH Patch. The Table 10 contains the energy extracted on the rear wing.

Table 10. The estimated energy outcome on 50% of the rear wingspan.

Materials	Energy Extracted (W)	Materials	Energy Extracted (W)
Aluminium Alloy	850.62	CFRP- Woven-Wet	583.606
E-GFRP-Fabric	257.04	E-GFRP-UD	423.8
CFRP-UD-Wet	773.053	E-GFRP-Wet	338.9
CFRP-UD-Prepreg	795.81	S-GFRP-UD	445.71
CFRP-Woven-Prepreg	603.423	FR-4-GFRP-Woven	237.67
KFRP-UD-49	508.01		

The same calculations are followed to determine the power outcome of the PVEH Patch. Table 11 contains the energy extracted on the vertical stabilizer.

Table 11. The estimated energy outcome on 50% of the VS.

Materials	Energy Extracted (W)	Materials	Energy Extracted (W)
Aluminium Alloy	0.071	CFRP- Woven-Wet	0.035
E-GFRP-Fabric	0.037	E-GFRP-UD	0.046
CFRP-UD-Wet	0.042	E-GFRP-Wet	0.041
CFRP-UD-Prepreg	0.056	S-GFRP-UD	0.041
CFRP-Woven-Prepreg	0.044	FR-4-GFRP-Woven	0.018
KFRP-UD-49	0.026		

3.4. Selection and Calculation of Solar Cell in Top Wing

The solar cells are categorized into three types. The first-generation solar cells are mainly based on silicon wafers and typically demonstrate a performance of about 15–25%. These types of solar cells dominate the market and are mainly those seen on rooftops. The second-generation solar cells are based on materials, such as amorphous silicon, CIGS and CdTe, where the typical performance is 10–15%. The second-generation solar cells are defined as thin film solar cells, since they use direct band gap materials and can be made much thinner than first generation solar cells. The third generation of solar cells is a mix of many types of solar cells. One example is organic solar cells, which include small molecule and polymer solar cells. It also covers expensive high performance experimental multi-junction solar cells, which hold the word record in solar cell performance, plus novel devices in general. Copper indium gallium selenide is preferred, which possess low energy payback time and high efficiency. The efficiency of the solar cell is given in Equation (23) [2,4,14,19,29,36].

$$\eta = P_{out}/P_{in} \tag{23}$$

where, Pout refers to power from photo voltaic device and Pin refers to power from illumination. The formula for power input from solar cells loaded on this proposed hybrid UAV is given in Equation (24).

$$P_{in} = \sigma\, A \tag{24}$$

where, "σ" is solar constant which is estimated as 1000 W/m^2, and "A" is the area of solar cell and to find the area of solar cell, the important relationship is mentioned in Equation (25).

$$A = P_{need}/\eta\sigma \tag{25}$$

where, P_{need} is the amount of power required for our application, and peak sun hour is the global irradiance per day /STC. Hence, substituting the values in a reverse process, the input and output of the solar are calculated. The CIGS solar cell is planned to place at the top of both (front and rear) wing and at the lateral side of the vertical stabilizer. For the calculation, the authors proposed that the CIGS operating condition 27 °C. On the top of the wing, the space left after placing the PVEH patch is the space allowed for placement. Therefore, 50% is allocated for PVEH and Solar Cell, respectively. After detecting some of the allowances, the desired span of the solar panel at one side of wing is developed as span of solar panel is 0.5785 m. The CIGS solar cell is taken, and the defined parameters are taken from strong literature survey [2,4,14,19,29,36]. The following are the calculations dedicated for the estimation of power from the solar cell on the top of the front wing: Open circuit voltage (V_{OC}) as 856.43 mV; Short circuit current density (J_{SC}) as 33.09 mA; Fill Factor(FF) as 85.73%; Efficiency (η) as 24.27% [2,4,14,19,29,36].

$$\text{Input Power } (P_{in}) = \text{ solar irradiance } \times \text{ area of the solar cell} \tag{26}$$

where, σ is the solar irradiance and it is given as $\sigma = 0.1\ W/cm^2$ and the area of the solar cell on the top of the wing is determined as 0.1425 m^2. Therefore,

$$P_{in} = 0.1 \times 1425 \Rightarrow P_{in} = 142.5\ W$$

Hence, the input power is calculated as 142.5 W, the efficiency (η) is calculated as,

$$\eta = \frac{P_{max}}{P_{in}} \tag{27}$$

The P_{in} is the input power, on substituting the necessary values in the above equation,

$$24.27\ \% = \frac{P_{max}}{142.5} \Rightarrow P_{max} = 34.58\ W$$

For the rear side of the wing, the area of the solar cell planned for placement is 0.0936 m^2, and the same above calculation is carried out and the P_{max} obtained is 22.72 W. To utilize the lateral side of the vertical stabilizer, the solar panel is imposed. Thus, after assuming the allowances, the area of the solar cell planned is 0.053 m^2. Hence, the power output of the one side of the solar panel placed on the vertical stabilizer is 12.86 W. the calculated power output is for one portion of the respective placement. The summation of all the solar panels placed on the respective position is tabulated and listed in Table 12.

Table 12. The total power output of the solar panel.

Placement of Solar Cell	P_{max} (W)	Overall Output(W)
Top of the front wing	34.58	69.16
Top of the rear wing	22.72	45.44
Lateral side of the vertical stabilizer	12.86	51.44
Total power output of the solar panel		166.04

The resultant renewable energy from this proposed scheme is calculated with the help of integrated engineering approach. The comprehensive renewable energies are listed in Table 13.

Table 13. The comprehensive estimated total output power developed in energy drone through hybrid energy scheme.

Lightweight Materials	Energy Extracted through PVEH Patches (W)			Energy Extracted through Solar Panels (W)			Resultant Renewable Power (W)
	Front Wing	Rear Wing	Vertical Stabilizer	Front Wing	Rear Wing	Vertical Stabilizer	
Aluminium Alloy	818.19	850.62	0.071	69.16	45.44	51.44	1834.921
E-GFRP-Fabric	251.67	257.04	0.037				674.787
CFRP-UD-Wet	759.77	773.053	0.042				1698.905
CFRP-UD-Prepreg	781.33	795.81	0.056				1743.236
CFRP-Woven-Prepreg	587.10	603.423	0.044				1356.607
CFRP- Woven-Wet	568.10	583.606	0.035				1317.781
E-GFRP-UD	415.15	423.8	0.046				1005.036
E-GFRP-Wet	332.03	338.9	0.041				837.011
S-GFRP-UD	436.78	445.71	0.041				1048.571
FR-4-GFRP-Woven	228.00	237.67	0.018				631.728
KFRP-UD-49	498.09	508.01	0.026				1172.166

4. Conclusions

An in-depth review of the relevant literature sets the way for the conceptual design of the hybrid unmanned aerial vehicle to match the original goal. The required outcomes were accomplished by the utilization of CFD, FEA, and modal simulation. The aeroplanes that serve as inspirations for the design of the Murder Hornet Hybrid UAV have greater payload carrying capacities and greater aerodynamic efficiencies. The unmanned aerial vehicle is capable of reaching high speeds of up to 150 km per hour. Epoxy Carbon Woven Wet shines brightest when strength is the focus of the discussion. The power output of aluminium alloy was significantly higher than that of the other materials examined; as a result of its spacious fuselage, a greater quantity of payloads, such as food and medicine, could be loaded and delivered to any location at any time. This capability was made possible by the aircraft. In comparison to its conventional equivalent, the hybrid UAV has a longer range and greater endurance. The piezoelectric patches that are attached to the UAV's wings not only provide it with the power it needs to function, but also increase its range and duration of flight. Even in conditions where there is not a significant amount of light, the soldiers will be able to see their target area well because to the Short-Wave Infrared and Thermal Imaging Camera that has been implemented. Altering the positioning of the solar panels that are intended for this hybrid UAV might also improve its overall efficiency and versatility. The viability of the integrated engineering technique that was proposed for estimating renewable energy through PVEH patches has been validated by this body of work, and as a result, the same methodology has been made available to researchers for use in future applications. These researchers also introduced the concept of hybrid energy for future unmanned aircraft systems, which is a concept that will find significant use in the field of unmanned aircraft systems as it continues to develop.

For PVEH patches-based energy extractions, the authors used two ways to determine and validate amount of attained electrical power. Firstly, Sijun Du et al. [25] studied and provided the standard analytical formula for the development of electrical power through PVEH patches. Thus, the current authors were previously imposed in this analytical formula in our propellers of UAVs [Naveen Kumar Kulandaiyapan et al. [14,15] found the needful electrical power extraction of the imposed PVEH patches.

Secondly, the current authors executed the validation of this imposed PVEH patches approach through the help of experimental correlation study, which was conducted by J. A. Dunnmon et al. [26]. The imposed technique of this work is coupled CFD (computational fluid dynamics) and CVA (computational vibrational analysis) based advanced scheme, which was validated with aforesaid experimental study, wherein the authors found the error percentage is 8. Thus, the authors are strongly recommended our current proposal for real-time applications.

The architecture of this imposed hybrid energy scheme for hybrid energized drone is systematical revealed in Figure 1. Through this planned architecture, the authors are planned to use the cumulative voltages (PVEH patches + Solar panels) for real-time UAV based applications.

Author Contributions: Conceptualization, V.R. and L.K.; methodology, V.R., N.K.K. and A.A.T.; software, V.R. and N.M.; validation, V.R., N.M. and H.A.Z.A.-b.; formal analysis, V.R. and H.A.Z.A.-b.; investigation, V.R., N.M. and L.K.; resources, V.R., N.K.K. and N.M.; data curation, V.R. and A.A.T.; writing—original draft preparation, N.M.; writing—review and editing, L.K., A.A.T. and V.R.; visualization, H.A.Z.A.-b. and Y.W.; supervision, M.A.-B.; project administration, Y.W.; funding acquisition, Y.W. All authors have read and agreed to the published version of the manuscript.

Funding: This paper is partially supported by the Nantong Basic Research Program Project (Project No.: JC22022067), cultivation object of "Qinglan Project" in colleges and universities of Jiangsu Province and the second-level cultivation object of Jianghai Talent Cultivation Special in the sixth phase of Nantong City.

Institutional Review Board Statement: Not applicable.

Informed Consent Statement: Not applicable.

Data Availability Statement: Not applicable.

Acknowledgments: These computing resources were generously provided by the Aircraft Design and Analyses Laboratory in the Department of Aeronautical Engineering at Kumaraguru College of Technology (KCT) in Coimbatore-641049, Tamil Nadu, India. Therefore, the authors of this piece appreciate the support of the company's upper management and the industry's finest.

Conflicts of Interest: The authors declare no conflict of interest.

References

1. Maurya, S.; Suman, P.; Radhakrishna, M. A review of energy harvesting techniques for WSN. In Proceedings of the 8th International Conferenceon Wireless Communicationand Sensor Networks (WCSN-2012), Phitsanulok, Thailand, 19–23 December 2012. [CrossRef]
2. Akinaga, H. Recent advances and future prospects in energy harvesting technologies. *Jpn. J. Appl. Phys.* **2020**, *59*, 321–327. [CrossRef]
3. Aabid, A.; Parveez, B.; Raheman, A.; Ibrahim, Y.; Anjum, A.; Hrairi, M.; Parveen, N.; Zayan, J.M. A Review of Piezoelectric Material-Based Structural Controland Health Monitoring Techniques for Engineering Structures: Challenges and Opportunities. *Actuators* **2021**, *10*, 101. [CrossRef]
4. Samal, N.; Shiney, O.J. Energy Harvesting using Piezoelectric Transducers: A Review. *J. Sci. Res.* **2021**, *65*, 163–176. [CrossRef]
5. Baniya, P.; Barge, S.; Patil, R.; Yewale, P. Power Generation using Piezoelectric Material. *Int. Res. J. Eng. Technol.* **2019**, *6*, 6586–6589.

6. Morton, S.; D'Sa, R.; Papanikolopoulos, N. Solarpowered UAV: Design and experiments. In Proceedings of the IEEE/RSJ International Conferenceon Intelligent Robotsand Systems (IROS), Hamburg, Germany, 28 September–2 October 2015; pp. 2460–2466. [CrossRef]
7. Jiajan, W.; Kampoon, J.; Klongtrujrok, J.; Yuthayanon, I. Conceptual Designof Tactical Solar Power UAV. *IOP Conf. Ser. Mater. Sci. Eng.* **2019**, *501*, 012011. [CrossRef]
8. Vijayanandh, R.; Kumar, J.D.; Kumar, M.S.; Bharathy, L.A.; Kumar, G.R. Design and fabrication of solar powered unmanned aerial vehicle for border surveillance. In *Proceedings of International Conference on Remote Sensing for Disaster Management*; Springer: Cham, Switzerland, 2018; pp. 61–71. [CrossRef]
9. Chu, Y.; Ho, C.; Lee, Y.; Li, B. Development of a Solar-Powered Unmanned Aerial Vehicle for Extended Flight Endurance. *Drones* **2021**, *5*, 44. [CrossRef]
10. Suman, S.; Kumar, S.; De, S. UAV-Assisted RF energy transfer. In Proceedings of the 2018 IEEE International Conference on Communications (ICC), Kansas City, MO, USA, 20–24 May 2018; pp. 1–6. [CrossRef]
11. Thakur, A.K.; Kumar, D. Aerodynamic stability on piezoelectric multi Rotor UAV with numerical case learning. *Eur. J. Mol. Clin. Med.* **2021**, *7*, 1559–1568.
12. Turgut, E.; Gursoy, M.C.; Guvenc, I. Energy Harvestingin Unmanned Aerial Vehicle Networks With 3D Antenna Radiation Patterns. *IEEE Trans. Green Commun. Netw.* **2020**, *4*, 1149–1164. [CrossRef]
13. Quyen, T.V.; Nguyen, C.V.; Le, A.M.; Nguyen, M.T. Optimizing Hybrid Energy Harvesting Mechanisms for UAVs. *EAI Endorsed Trans. Energy Web* **2020**, *7*, e8. [CrossRef]
14. Kulandaiyapan, N.K.; Gnanasekaran, R.K.; Raja, V.; Bernard, F.A.; Murugesan, R.; Madasamy, S.K.; Mathaiyan, V.; Raji, A.P.; Asher, P.K.; Ponmariappan, J. Optimization of high payload unmanned aerial vehicle's propellers based on energy formation by using computational vibrational analyses. In Proceedings of the AIAA Propulsion and Energy 2021 Forum, Virtual, 9–11 August 2021. [CrossRef]
15. Kumar, K.N.; Meenakshi, S.; Deviparameswari, K.; Vaidegi, R.; Nandhagopal, R.; Ramesh, M.; Vijayanandh, R. Investigation of energy generation on large rotary wing unmanned aerial vehicle's propeller using coupled engineering approaches. In *Advances in Environment Engineering and Management*; Springer: Cham, Switzerland, 2021; pp. 209–224. [CrossRef]
16. Morada, A.M.; Elzahaby, A.; Abdallah, S.; Kameld, M.; Khalile, M.K. Application of Piezoelectric Materialsfor Aircraft Propeller Blades Vibration Damping. *Int. J. Sci. Eng. Res.* **2015**, *6*, 513–520.
17. Anton, S.R.; Erturk, A.; Kong, N.; Ha, D.; Inman, D. An Investigation on multi-functional piezoelectric composite spars for energy harvesting in unmanned aerial vehicles. In Proceedings of the 17th International Conference on Composite Materials (ICCM-17), Edinburgh, UK, 27–31 July 2009. [CrossRef]
18. Anton, S.R.; Inman, D.J. Vibrationenergy harvesting for unmanned aerial vehicles. In *Active and Passive Smart Structures and Integrated Systems*; International Society for Opticsand Photonics: Bellingham, WA, USA, 2008; Volume 6928. [CrossRef]
19. Nishida, R.; Zhong, J.; Shinshi, T. Effectof Forced Liquid Cooling on the Voltage/Charge Displacement Characteristics of Stacked Piezoelectric Actuators during High-Frequency Drive. *Actuators* **2021**, *10*, 297. [CrossRef]
20. Yi, K.A.; Veillette, R.J. A charge controller for linear operation of a piezoelectric stack actuator. *IEEE Trans. Control Syst. Technol.* **2005**, *13*, 517–526. [CrossRef]
21. Sri, K.R.B.; Aneesh, P.; Bhanu, K.; Natarajan, M. Design Analysisof Solar-Powered Unmanned Aerial Vehicle. *J. Aerosp. Technol. Manag.* **2016**, *8*, 397–407. [CrossRef]
22. Vijayanandh, R.; Senthilkumar, S.; Rajkumar, R.; Kumar, A.; Kumar, J.D.; Kumar, K.K.; Prakash, R.A. Conceptual design and computational investigations of fixed wing unmanned aerial vehicle for medium-range applications. In *Autonomous and Connected Heavy Vehicle Technology*, 1st ed.; Academic Press: Cambridge, MA, USA, 2022; pp. 353–374. [CrossRef]
23. Raja, V.; Solaiappan, S.K.; Kumar, L.; Marimuthu, A.; Gnanasekaran, R.K.; Choi, Y. Designand Computational Analyses of Nature Inspired Unmanned Amphibious Vehiclefor Deep Sea Mining. *Minerals* **2022**, *12*, 342. [CrossRef]
24. Raja, V.; Gnanasekaran, R.K.; Rajendran, P.; Ali, A.M.; Rasheed, R.; Al-Bonsrulah, H.A.Z.; Al-Bahrani, M. Asymmetrical Damage Aspects Based Investigations on the Disc Brake of Long-Range UAVs through Verified Computational Coupled Approaches. *Symmetry* **2022**, *14*, 2035. [CrossRef]
25. Du, S.; Jia, Y.; Seshia, A. Maximizing Output Powerina Cantilevered Piezoelectric Vibration Energy Harvester by Electrode Design. *J. Phys. Conf. Ser.* **2015**, *660*, 012114. [CrossRef]
26. Dunnmon, J.; Stanton, S.; Mann, B.; Dowell, E. Power extraction from aeroelastic limit cycle oscillations. *J. Fluids Struct.* **2011**, *27*, 1182–1198. [CrossRef]
27. Nishanth, B.; Kumar, D.S.; Naveen, A.; Vijayanandh, R.; Kumar, M.S. Energy harvesting from a Gas Turbine Engines exhaust heat Using Quantum Well Thermo Electricmaterials Generator (QWTEG). *Mater. Today Proc.* **2017**, *4*, 8378–8386. [CrossRef]
28. Balaji, S.S.; Raja, V.; Raji, A.P.; Madasamy, S.K.; Kulandaiyappan, N.K.; Gnanasekaran, R.K.; Kandasamy, S.; Rajapandi, R.; Nagarajan, N.; Kannan, S.D.; et al. Conceptual design and comparative power generations on unmanned aerial vehicle's wing with rotors using CFD. In Proceedings of the AIAA SCITECH 2022 Forum, San Diego, CA, USA, 3–7 January2022. [CrossRef]
29. Murugesan, K.; Vijayanandh, R.; Venkatesan, R.; Saravanan, R.; Senthilkumar, S.; Kumar, J.D. Conceptual design of high endurance cum hybrid configuration based personal air vehicles with three-axis solar tracker system. In Proceedings of the 2021 International Conference on Advancements in Electrical, Electronics, Communication, Computing and Automation (ICAECA), Coimbatore, India, 8–9 October 2021; pp. 1–7. [CrossRef]

30. Balamurugan, R.J.; Al-Bonsrulah, H.A.Z.; Raja, V.; Kumar, L.; Kannan, S.D.; Madasamy, S.K.; Rasheed, R.; Rajendran, P.; Al-Bahrani, M. Design and Multiperspectivity based performance investigations of H-Darrieus vertical Axis wind turbine through computational fluid dynamics adopted with moving reference frame approaches. *Int. J. Low-Carbon Technol.* 2022; *in press*. [CrossRef]
31. Madasamy, S.K.; Raja, V.; Al-Bonsrulah, H.A.Z.; Al-Bahrani, M. Design, development, and multi-disciplinary investigations of aerodynamic, structural, energy, and exergy factor son 1k Whorizontal Axiswind turbine. *Int. J. Low-Carbon Technol.* 2022; *in press*. [CrossRef]
32. Raja, V.; Al-Bonsrulah, H.A.Z.; Raji, A.P.; Madasamy, S.K.; Ramaiah, M.; Gnanasekaran, R.K.; Kulandaiyapan, N.K.; Al-Bahrani, M. Design and multi-disciplinary computational investigations on PVEH patches attached horizontal axis hybrid wind turbine system for additional energy extraction in HALE UAVs. *IET Renew. Power Gener.* 2022; *in press*. [CrossRef]
33. Raja, V.; Murugesan, R.; Rajendran, P.; Palaniappan, S.; Al-Bonsrulah, H.A.Z.; Jayaram, D.K.; Al-Bahrani, M. Multi-Domain Based Computational Investigationson Advanced Unmanned Amphibious System for Surveillancesin International Marine Borders. *Aerospace* **2022**, *9*, 652. [CrossRef]
34. Rajagurunathan, M.; Raj Kumar, G.; Vijayanandh, R.; Vishnu, V.; Rakesh Kumar, C.; Mohamed Bak, K. The Design Optimization of the Circular Piezoelectric Bimorph Actuators Using FEA. *Int. J. Mech. Prod. Eng. Res. Dev.* **2018**, *8*, 410–422.
35. Kumar, V.A.; Sivaguru, M.; Janaki, B.R.; Eswar, K.S.S.; Kiran, P.; Vijayanandh, R. Structural Optimization of Frame of the Multi-Rotor Unmanned Aerial Vehicle through Computational Structural Analysis. *IOP J. Phys. Conf. Ser.* **2021**, *1849*, 012004. [CrossRef]
36. Asaduzzaman; Bahar, A.N.; Bhuiyan, M.M.R. Dataset demonstrating the modeling of a high performance Cu(In,Ga)Se 2 absorber based thin film photovoltaic cell. *Data Brief* **2017**, *11*, 296–300. [CrossRef]
37. Gu, H.; Lyu, X.; Li, Z.; Shen, S.; Zhang, F. Development and experimental verification of ahybrid vertical take-off and landing (VTOL) unmannedaerial vehicle (UAV). In Proceedings of the International Conference on Unmanned Aircraft Systems, ICUAS, Miami, FL, USA, 13–16 June 2017; pp. 160–169. [CrossRef]
38. Hochstenbach, M.; Notteboom, C.; Theys, B.; de Schutter, J. Designand Controlofan Unmanned Aerial Vehicle for Autonomous Parcel Delivery with Transition from Vertical Take-off to Forward Flight. *Int. J. Micro Air Veh.* **2015**, *7*, 395–405. [CrossRef]
39. Aktas, Y.O.; Ozdemir, U.; Dereli, Y.; Tarhan, A.F.; Cetin, A.; Vuruskan, A.; Yuksek, B.; Cengiz, H.; Basdemir, S.; Ucar, M.; et al. Rapid Prototyping of a Fixed-Wing VTOLUAV for Design Testing. *J. Intell. Robot. Syst.* **2016**, *84*, 639–664. [CrossRef]
40. Gokhale, R.; Wan, Y.; Mehndiratta, M.; Kayacan, E. Fixed-wing vertical-take off-and-landing UAV with additive manufacturing: Adual-rotorversion. In Proceedings of the 3rd International Conference on Progressin Additive Manufacturing, Singapore, 14–17 May 2018; pp. 250–255. [CrossRef]
41. Krishnakumar, R.; Kumar, K.S.; Anand, T. Design and Development of Vertical Take off and Horizontal Transition Mini Unmanned Aerial Vehicle. *Adv. Mater. Res.* **2014**, *1016*, 436–440. [CrossRef]
42. Serrano, A.R. Design methodology for hybrid (VTOL+Fixed Wing) unmannedaerial vehicles. *Aeronaut. Aerosp. Open Access J.* **2018**, *2*, 165. [CrossRef]
43. Dündar, Ö.; Bilici, M.; Ünler, T. DesignandperformanceanalysesofafixedwingbatteryVTOLUAV. *Eng. Sci. Technol. Int. J.* **2020**, *23*, 1182–1193. [CrossRef]
44. Rahman, Y.A.A.; Hajibeigy, M.T.; Al-Obaidi, A.S.M.; Cheah, K.H. Design and Fabrication of Small Vertical-Take-Off-Landing Unmanned Aerial Vehicle. *MATEC Web Conf.* **2018**, *152*, 02023. [CrossRef]
45. Ozdemir, U.; Aktas, Y.O.; Demirbag, K.; Erdem, A.; Kalaycioglu, G.D.; Ozkol, I.; Inalhan, G. Design of acommercial hybrid VTOLUAV system. *J. Intell. Robot. Syst.* **2013**, *74*, 214–220. [CrossRef]